

ACTIVE MIRROR STRUCTURES

R. R. Shannon
R. M. Richard
J. G. Hansen

Optical Science Center
and
Civil Engineering Department
University of Arizona
Tucson, Arizona 85721

Approved for Public Release;
Distribution Unlimited

15 January 1981

Prepared for
Defense Advanced Research Projects Agency
1400 Wilson Boulevard
Arlington, Virginia 22209

Monitoring Agency

Director, Physics Program
Office of Naval Research
800 North Quincy Street
Arlington, Virginia 22217

PLEASE RETURN TO:

BMD TECHNICAL INFORMATION CENTER
BALLISTIC MISSILE DEFENSE ORGANIZATION
7100 DEFENSE PENTAGON
WASHINGTON D.C. 20301-7100

19980309 173

U 43 43

Accession Number: 4343

Publication Date: Jan 15, 1981

Title: Active Mirror Structures

Personal Author: Shannon, R.R.; Richard, R.M.; Hansen, J.G.

Corporate Author Or Publisher: Optical Sciences Center, University of Arizona, Tucson, Arizona 85721

Report Prepared for: Office of Naval Research, 800 North Quincy Street, Arlington, VA 22217 Report
Number Assigned by Contract Monitor: SLL 81-143/LO/L

Comments on Document: Archive, RRI, DEW

Descriptors, Keywords: Active Mirror Structure

Pages: 00061

Cataloged Date: Feb 25, 1993

Document Type: HC

Number of Copies In Library: 000001

Record ID: 26328

Source of Document: DEW

ABSTRACT

This report summarizes work done on a Large Active Mirror Structure Design at the University of Arizona. The design goal is a 4 meter diameter aperture, $f/1.5$ primary mirror. The recommended mirror structure uses a 2 cm by 4 m diameter solid ULE faceplate supported on a low bandwidth active truss support structure whose principal backplate component is made of high stiffness graphite epoxy material. Loads are distributed between the mirror component and the backplate such as to introduce corrections for errors due to mechanical and thermal distortion. This report carries through a detailed structural analysis and provides recommendations for implementation of an extremely lightweight mirror appropriate for either space or terrestrial use.

TABLE OF CONTENTS

	Page
ABSTRACT	i
TABLE OF CONTENTS	ii
LIST OF ILLUSTRATIONS	iv
LIST OF TABLES	viii
 Chapter 1	
INTRODUCTION	1
 Chapter 2	
INTEGRATED ACTIVE MIRROR SYSTEMS	8
Concept Definition	8
Experimental Verification of 41-Actuator System	10
Mirror Scallop	23
 Chapter 3	
PRELIMINARY STUDIES	26
Analysis of 2-Dimensional Model of an Integrated Active Mirror System	27
Finite Element Models	27
Normal Position Control	31
Slope Control	38
Structural Member Connectivity	43
Loads	46
Shear Modulus of Sandwich Core	49
Flat Plates	54
SAP IV Flat Plate Analysis	54
MSC/NASTRAN Flat Plate Analysis	58
Contour Plot Interpretation	61

TABLE OF CONTENTS--cont.

Chapter 4		Page
40-ACTUATOR MIRROR		63
Finite Element Models		64
Normal Position and Slope Controls		66
Defocus and Astigmatism		73
Gravity and Lap Loads		86
FRINGE Data Reduction		89
Heat Transfer		92
 Chapter 5		
40-ACTUATOR SYSTEM.		95
Finite Element Models		97
Specifications		98
Mounts		101
Mechanical Design of Controls		106
Testing the Model		112
Normal Position and Slope Controls		114
Actuator Force Determination		129
Defocus and Astigmatism		130
Gravity Loads		136
Thermal Loads		142
Miscellaneous Output		154
Stress		155
Actuator Strength and Stroke		158
Actuation Sensitivity		160
 Chapter 6		
ADDITIONAL WORK		162
 Chapter 7		
CONCLUSIONS		167
REFERENCES		171

LIST OF ILLUSTRATIONS

Figure		Page
2.1	Truss Configuration for 40- and 41-Actuator Systems. . .	9
2.2	Two Photographs of the 41-Actuator System Built for the Experimental Tests	12
2.3	41-Actuator System. Undeformed Shape	13
2.4	Schematic Layout of Holographic Interferometric Test of 60-cm Active Mirror Model	14
2.5	Slope Changes, 0.4 Zone	16
2.6	z Displacement, 0.4 Zone	17
2.7	41-Actuator System, 0.4 Zone	18
2.8	41-Actuator System, .8 Zone	19
2.9.	41-Actuator System, 1.0 Zone	20
2.10	Surface Profile Through Axis of Symmetry, 0.4 Zone . . .	21
2.11	Scallop of a Thin Mirror for a 9-Actuator System with a Focus Shift.	24
3.1	2-Dimensional Finite Element Models	28
3.2	Structural Members for 2-Dimensional Model	30
3.3	Models for Study of Normal Position Control	32
3.4	Case 5 Mirror and Reference Plate Deflections	34
3.5	Optimization Curves for Case 1 and Case 5	36
3.6	Models for Study of In-Plane Slope Control	39
3.7	Cases 9 and 11 Mirror and Reference Plate Deflections. .	42
3.8	Mirror and Reference Plate Deflections for Thermal Gradient and Gravity Loads	47
3.9	Modeling Webbed Core as Equivalent Solid Core	51
3.10	Sandwich Model	54
3.11	SAP IV Flat Plate Model	56
3.12	Supports and Loads for Flat Plate Models	57
3.13	NASTRAN Flat Plate Model	59

LIST OF ILLUSTRATIONS--cont.

Figure		Page
4.1	Mirror Model	65
4.2	Solid Mirror Model, 80-cm Actuators	67
4.3	Solid Mirror Model, 160-cm Actuators	68
4.4	Solid Mirror Model, 200-cm Actuators	69
4.5	Thin Lightweight Mirror Model, 80-cm Actuators	70
4.6	Thin Lightweight Mirror Model, 160-cm Actuators	71
4.7	Thin Lightweight Mirror Model, 200-cm Actuators	72
4.8	Cross Section of Ideal Defocus	74
4.9	Cylindrical Coordinate System	76
4.10	Thick, Lightweight Mirror Model, Defocus	77
4.11	Solid Mirror Model, Defocus	78
4.12	Thin Lightweight Mirror Model, Defocus	79
4.13	Thick Lightweight Mirror Model. Cross Sections for Defocus	80
4.14	Solid Mirror Model, Cross Sections for Defocus	81
4.15	Thin Lightweight Mirror Model, Cross Sections for Defocus	82
4.16	Solid Mirror Model, Astigmatism	85
4.17	Mirror Deflections Due to Gravity and Lap Loads	87
4.18	Fringe Data to Support Choice of Residual for rms Calculation	90
4.19	Approximate Thermal Models	93
5.1	40-Actuator System. Undeformed Shape	99
5.2	Cross Sections and Material Properties for 40-Actuator System	100
5.3	Reference Plate and Supporting Flexures	103
5.4	Normal Position Control and Slope Control Models	104
5.5	Actuator Post Flexures	105
5.6	Plan View of Servomechanisms	108

LIST OF ILLUSTRATIONS--cont.

Figure		Page
5.7	Side View of Servomechanisms	110
5.8	Normalized Deflections for Normal Position Control and Slope Controls	111
5.9	System Model with Thick Lightweight Mirror, 80-cm Actuators	116
5.10	System Model with Thick Lightweight Mirror, 160-cm Actuators	117
5.11	System Model with Thick Lightweight Mirror, 200-cm Actuators	118
5.12	System Model with Solid Mirror and Nominal Reference Plate, 80-cm Actuators	120
5.13	System Model with Solid Mirror and Nominal Reference Plate, 160-cm Actuators	121
5.14	System Model with Solid Mirror and Nominal Reference Plate, 200-cm Actuators	122
5.15	System Model with Solid Mirror and Nominal Reference Plate, 160-cm Actuators ($\theta = 22.5^\circ$)	123
5.16	System Model with Solid Mirror and Small Reference Plate, 80-cm Actuators	124
5.17	System Model with Solid Mirror and Small Reference Plate, 160-cm Actuators	125
5.18	System Model with Solid Mirror and Small Reference Plate, 200-cm Actuators	126
5.19	System Model with Solid Mirror, Small Reference Plate and Flexure Mount. Two Slope Controls	128
5.20	System Model with Solid Mirror and Small Reference Plate, Defocus	131
5.21	System Model with Solid Mirror and Small Reference Plate. Cross Sections for Defocus	132
5.22	System Model with Solid Mirror and Small Reference Plate, Astigmatism	135

LIST OF ILLUSTRATIONS--cont.

Figure		Page
5.23	System Model with Solid Mirror and Small Reference Plate, x Gravity load of $1g$	137
5.24	System Model with Solid Mirror and Small Reference Plate, y Gravity Load of $1g$	138
5.25	System Model with Solid Mirror and Small Reference Plate, z Gravity Load of $1g$	139
5.26	System Model with Solid Mirror and Small Reference Plate, Cross Sections for z Gravity Load	140
5.27	System Model with Solid Mirror, Nominal Reference Plate, and Flexure Mount; Gravity Loads	143
5.28	System Model with Solid Mirror and Small Reference Plate, Axial Thermal Gradient of $1^{\circ}C$	145
5.29	System Model with Solid Mirror and Small Reference Plate, Uniform Thermal Soak of $1^{\circ}C$	146
5.30	System Model with Solid Mirror and Small Reference Plate, Cross Sections for Thermal Gradient	147
5.31	System Model with Solid Mirror and Small Reference Plate, Cross Sections for Thermal Soak	148
5.32	System Model with Solid Mirror, Nominal Reference Plate, and Flexure Mount. Thermal Loads	152

LIST OF TABLES

Table		Page
3.1	Variations of Case 5 Normal Position Control Model . . .	45
3.2	Mechanical Properties of Three Sandwich Cores	53
3.3	Results of SAP IV Flat Plate Analysis	55
3.4	Results of NASTRAN Flat Plate Analysis	60
4.1	Residual Wavefront Variations for Defocus and Astigmatism of Three Mirror Models	84
5.1	Mass Summary for Three Versions of 40-Actuator System. .	102
5.2	Residual Wavefront Variations for Defocus and Astigmatism for System Model with Solid Mirror and Small Reference Plate	134
5.3	Residual Wavefront Variations after Subtraction of Tilt and Defocus for System Model with Solid Mirror and Small Reference Plate	141
5.4	Residual Wavefront Variations after Subtraction of Tilt and Defocus for Two Different 40-Actuator Systems .	144
5.5	Thermal Loads in °C Producing Residual Wavefront Variation of .1λ rms for System Model with Solid Mirror and Small Reference Plate	151
5.6	Stresses in System Model in Dyne/cm ²	157
5.7	Maximum Actuator Forces and Deflections in System Model with Solid Mirror and Small Reference Plate	159
5.8	Sensitivities of 80-cm Actuators	161
6.1	Additional Work to be Completed	163

CHAPTER 1

INTRODUCTION

This report completes 5 years of work by the University of Arizona on deformable lightweight mirrors. This work has involved much computation and computer modeling and some experimental concept verification, and it has been carried out as a portion of several contracts.* Listed at the end of this section are two earlier reports on this project.

The original mirror concept proposed the support of a thin-shell mirror, actively controlled with force actuators that are related to a minimal backing structure which was not required to have excess stiffness. The actuator concept employed force loading, rather than positional changes, to control deformations in the thin shell surface. Early in this work it was demonstrated that the number of actuator or control points could be reduced significantly by using three degrees of freedom at each control point. These degrees of freedom are a displacement perpendicular to the surface and tilt in the radial and tangential directions on the mirror surface. The number of actuators and stiffness of the mirror plate were chosen such that nearly independent influence functions were obtained from each actuator. This yields the advantage of an influence matrix that is nearly diagonal and therefore the control devices can be implemented by rather inexpensive algorithms for specific applications.

*DARPA Contracts N00014-80-C-0565 and N00014-78-C-0282; Air Force Contract F04701-75-C-0106.

The mirror surface itself could consist of either a solid thin slab or a structured lightweight surface. The structured surface is advantageous because it permits the actuators to be attached so as to provide forces at the neutral plane of the element. This advantage is small, however, compared to the economic impact of using a sandwich structure versus a simple thin slab.

In this final report the mirror being considered is 4 meters in diameter and has a central hole of 0.8 m diameter. Several versions of plate thickness and backing structure were examined. One particular mirror design uses a 2-cm-thick solid ULE faceplate. A high modulus graphite epoxy material is used in the support structure. The total weight for a proposed 40-actuator 4-meter mirror amounts to 1,032 kilograms. By contrast, a typical solid mirror 4 meters in diameter would perhaps be 0.4 meter thick and would weigh more than 14,000 kilograms when suitable mounting is included. Needless to say, the weight advantage is significant, making this approach suitable for space applications. Terrestrial applications will likely benefit from similar weight reductions. In general, most types of errors induced in the mirror surface can be corrected to better than 1% of the induced error. Therefore, this mirror should be of adequate stiffness in any reasonable environment.

The present report is based in large part upon the Ph.D. dissertation research of Mr. James Hansen under the direction of Dr. Ralph Richard of the Civil Engineering Department. This work draws heavily upon previous work in this area and adds significant

new information, in that a complete modeling of the mirror system in considerable detail was carried out using the NASTRAN structural analysis program. This program was made available by courtesy of the Air Force Weapons Lab at Kirtland Air Force Base in Albuquerque.

As a guide to the details in the various chapters the following outline is presented:

Discussed in Chapter 2 is the general concept of the integrated active mirror system approach studied. The choice of the 40-actuator system is a compromise in terms of mirror stiffness, number of actuators, completeness of control, and the desire to reduce the amount of scalloping or residual error that remains when functional corrections are introduced that would change the focal length of the mirror surface. Support trusses and reference surface are integrated into one structure. Again, as noted, the backing plate and truss structure are not required to have infinite stiffness. This chapter also reviews an experimental verification of a 41-actuator system. This system is similar to the proposed 40-actuator system, except that there was no central hole in the mirror and thus a single central actuator post was added to the design. Holographic interferometry was used to examine the extent to which deformations produced by radial, tangential, and axial displacements on the surface would match those predicted from structural analysis. There were only three active actuators in this experiment; the remaining actuator posts were set at nominal positions to provide paths for reaction forces during changes in the mirrors. There is quite good matching of

the extent of the influence function and reasonable matching of its detailed shape. The concept of mirror scalloping is also discussed. Scalloping is a result of the fact that if the focal length or radius of the mirror is changed, the actual metric on the surface of the mirror must also necessarily change. Since glass is not easily stretched or squashed, a buckling or scalloping effect occurs between edge actuators. This is an intrinsic property of thin mirrors and can only be reduced, not eliminated. This reduction is accomplished by judicious placing of actuators along the periphery of the mirror.

Described in Chapter 3 are some preliminary studies that were made using two-dimensional analysis to examine the accuracy of different methods of modeling the mirror and to determine the properties of various truss components and shapes of truss components that would be used in the final mirror model. A set of possible couplings between reference plate deformations and mirror deformations was studied and used to determine optimum choice of the weight of the truss structure.

Presented in Chapter 4 is the specific design of a 40-actuator mirror, 4 m in diameter, with 80-cm-diameter central hole and radius of curvature of 12 m, yielding an f-number of $f/1.5$. The influence for each actuator type were evaluated, and corrections of various types of errors such as defocus and astigmatism were made. Contour plots were obtained showing the extent of the correction and the residuals remaining after correction. Table 4.1 in this chapter

summarizes some of the corrections that were observed. Figure 4.17 shows a more complex problem with residual mirror deflections due to gravity and lap loads that would occur in the handling of the mirror in the shop. Residual errors were compared with Zernike error terms, which are commonly used to evaluate residual RMS errors in the wave-front. It is shown that even a 36-term Zernike analysis is not adequate for describing the mirror characteristics in detail because of the large number of actuation points and the high order of symmetry that is obtained in the correction. Some thermal effects are also discussed.

In Chapter 5, the methods used in modeling the 40-actuator system are presented. Simulation of the control functions that would be applied in actual space-borne systems are made. Responses of the mirror to gravity loads, thermal gradients, thermal soaks, and mechanical deformations were determined. Differences between normal force control and normal and slope control were also evaluated. Since a ring of actuators was not placed at the central hole, some residual problems around this central region of the mirror were observed. In an actual final design, the structural designer would have to decide whether or not this additional set of actuators should be included.

Gravity deflections were quite large. With the mirror on edge, additional external loads would have to be applied to make the mirror controllable. This is not detrimental, however, as any type of mirror will require some specific handling gear to be tested in the unit-gravity field. Some consideration was given to launch

stresses, and it appears that the approach suggested will be satisfactory. Table 5.1 summarizes the weight of three versions of the system. The most strongly recommended approach is a solid mirror with a nominal reference plate, the total mass of which, including reference plate and estimated weight of servo mechanisms, is 1,032 kilograms. The total mass per mirror area is on the order of 86 kilograms per square meter. Note that the mirror alone is about 40 kilograms per square meter. Some suggested mechanizations for the actuators are carried through that are improved versions of those previously reported. No effort was made to analyze the dynamics of the control system in the presence of various rates of correction. The required force distribution in the mirror is estimated.

Finally, in Chapter 6, some suggestions are made for further work that may be carried out in detailed design of the mirror.

The conclusions are that the 40-actuator system provides a useful and viable concept that could be used for either a ground-based or space-based large optical system. Considerable economy would be achieved in the use of low expansion (ULE type) material, and the permitted flexure of the backing plate allows considerable scope in the design of the system. Obviously, problems need to be solved in the sensing and control over a stated bandwidth of the mirror surface. These, however, are outside the scope of this present work. Previous reports* on this project have discussed problems in introducing slope control, and of introducing holographic

components on mirror surfaces that may be used in an optical sensing scheme for controlling the surface.

* Previous Reports on Mirror Control

R. R. Shannon and W. S. Smith, Final Report on Active Mirror Holographic Interferometry, Final report on project USAF F04701-75-C-0106, Univ. of Arizona, September 1978.

R. R. Shannon, R. M. Richard and J. G. R. Hansen, Optimum Optical Structures for Active Control, Final report on project N00014-78-C-0282 (DARPA), Univ. of Arizona, January 1980.

CHAPTER 2

INTEGRATED ACTIVE MIRROR SYSTEMS

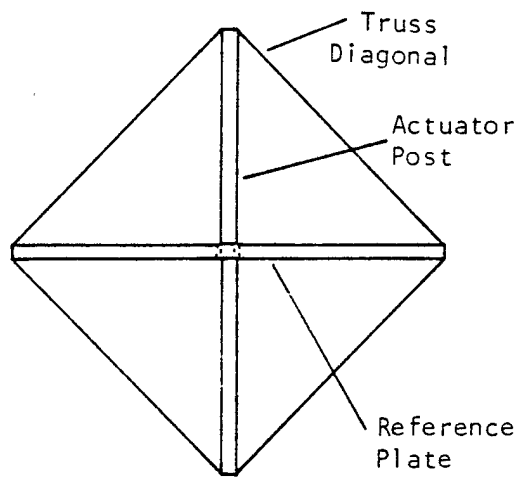
Concept Definition

Integrated active mirror systems studied in this effort differ from other mirror systems in two important respects. First, each mirror actuator controls the surface in three ways--normal position and slope about radial and tangential axes--thereby reducing the number of points at which actuation must be applied to the mirror. Second, the mirror element forms part of the structure instead of being referenced to a much stiffer reference plate. The integrated active mirror and support have an increased efficiency since the loads are carried in the direction of maximum structural stiffness, i.e. in tensile-membrane action. The weight of the system is minimized when the membrane of the shell (the active mirror) becomes part of the structure.

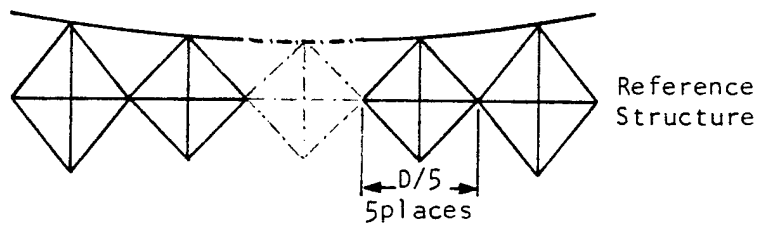
The number of actuators required for a system is a function of several variables: the mirror stiffness, the scale of the residual errors, the magnitude of the residual errors, and their form.

Previous studies have indicated that scalloping of the outer edge of the mirror is a significant problem. Scalloping occurs when an attempt is made to defocus the mirror. In choosing the 40-actuator system for further study, the effects of scalloping have been alleviated by closer placement of actuators at the outer edge.

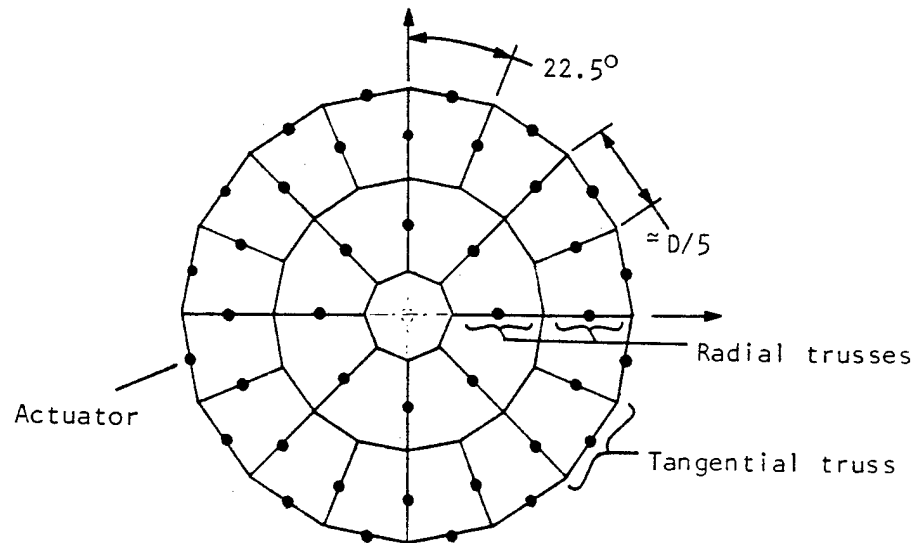
In order to increase the stiffness of the support structure, the truss and reference plate are integrated, as illustrated by the truss configurations in Fig. 2.1(a). Here the truss is modified to include the additional horizontal reference plate element.



(a) Individual truss.



(b) Section view of truss configuration along meridional plane.



(c) Top view.

Fig. 2.1. Truss Configuration for 40- and 41-Actuator Systems. Dashed Structural Members Only Exist in 41-Actuator System.

Figure 2.1(b), a meridional section view of the structure of the 40-actuator system, illustrates the change in actuator truss height with radial position and the symmetry of the truss about the reference plate. The stiffness of the reference structure is increased by the spoke configuration created by this radial alignment. The width of the radial trusses is $D/5$. A top view of the support structure is shown in Fig. 2.1(c). Sixteen tangentially aligned trusses have been added at points where scalloping would have been maximized in their absence. The positions of these actuators make the width of the edge actuator trusses approximately $D/5$.

This 40-actuator system is identical to that of the 4-m diameter mirror system analyzed in this report. Analyses used the MSC/NASTRAN and SAP IV finite element computer programs. Experimental verification of the integrated active mirror concept and the associated structural analysis was made using a 41-actuator system with a 60-cm aperture $f/1.5$ active mirror. The mirror in the 41-actuator system has no central hole, and the truss configuration is modified by the addition of a central actuator with a 3-dimensional truss. These modifications are shown in Fig. 2.1 in dashed lines. The experimental verification is briefly discussed below.

Experimental Verification of 41-Actuator System

A 60-cm aperture, $f/1.5$ active mirror was designed to demonstrate the figure control efficiency of a 41-actuator support concept. This system was designed to show the localization of both the position and slope controls. Three of the actuators were implemented with active components, the remaining 38 were preset mechanically in each of their three degrees of freedom. For these three active actuators, each degree

of freedom is controlled independently by a single servomotor. Photographs of the model are shown in Fig. 2.2.

Three views of a NASTRAN finite element model of the 41-actuator system are shown in Fig. 2.3. The physical dimensions, material specifications and mechanical design of that model are included in Shannon and Smith (1978). The topology and loading of the 41-actuator system mathematical model is similar to the model to be discussed in Chapter 4 under the heading 40-Actuator System Finite Element Model. The only differences are: 1) that only the three active actuators in the 41-actuator system have flexures in the middle of their actuator posts, 2) the inclusion of the central actuator with a 3-dimensional truss and the associated center section of the mirror, and 3) the boundary conditions are provided by four pinned attachments to the reference plate illustrated in Fig. 2.3 and representing four cone-tipped screws seated in counter sunk holes drilled in the reference plate of the experimental model.

The experimental arrangement is shown schematically in Fig. 2.4. Interferograms were produced and compared with contour plots from NASTRAN finite element analyses.

Figure 2.5(a) shows the effect of a tangential slope change produced at the 0.4 zone (9.5-cm radius). It bears a good resemblance to the prediction of the computer model (see Fig. 2.7(b)). Several fringes due to overall curvature change can be seen. This was caused by a change of one or two degrees Fahrenheit in the room temperature between the time the hologram was exposed and the time the interferogram was made. Some tilt is also noticeable, as well as irregularities due to air turbulence and reactions between the deformed shell and the fixed, passive actuators.

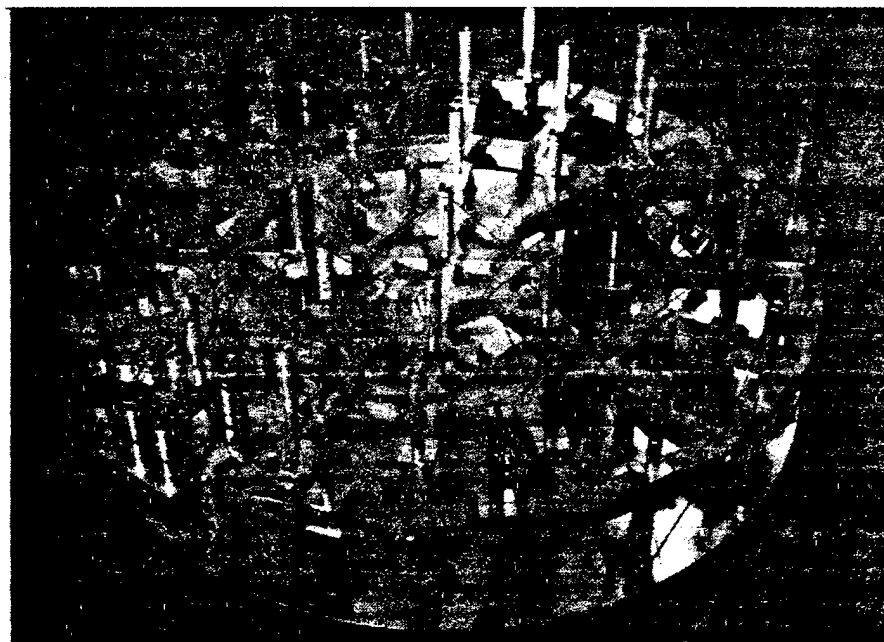
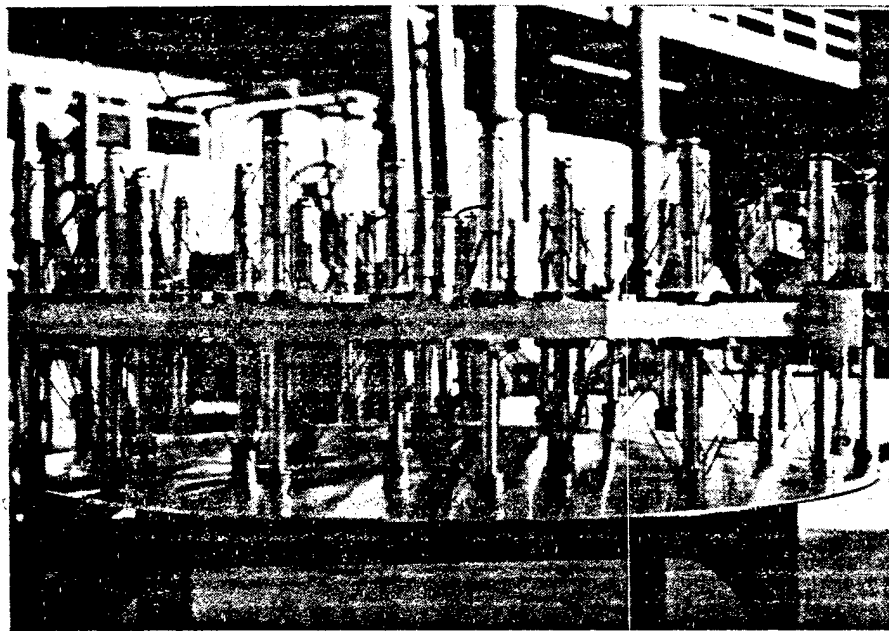
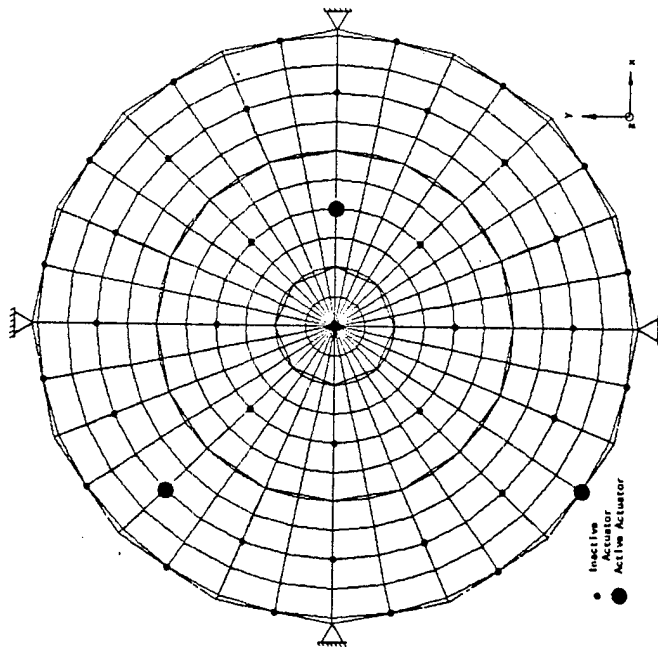
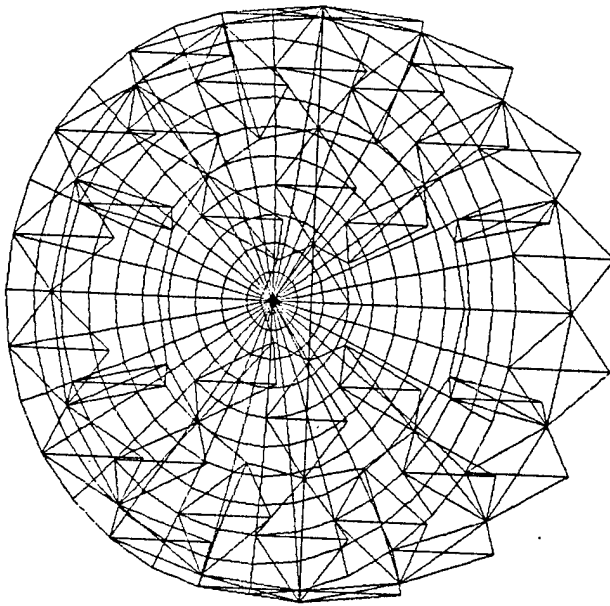


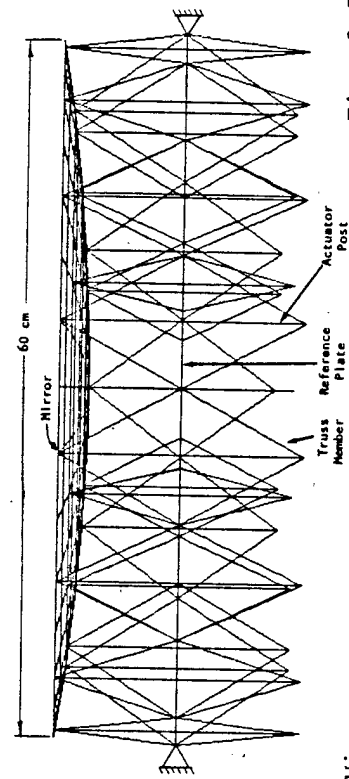
Fig. 2.2. Two Photographs of the 41-Actuator System Built for the Experimental Tests.



(a) Top View



(c) Orthographic Projection of Top View
Rotated -30° about x Axis



(b) Side View

Fig. 2.3. 41-Actuator System. Undeformed Shape.

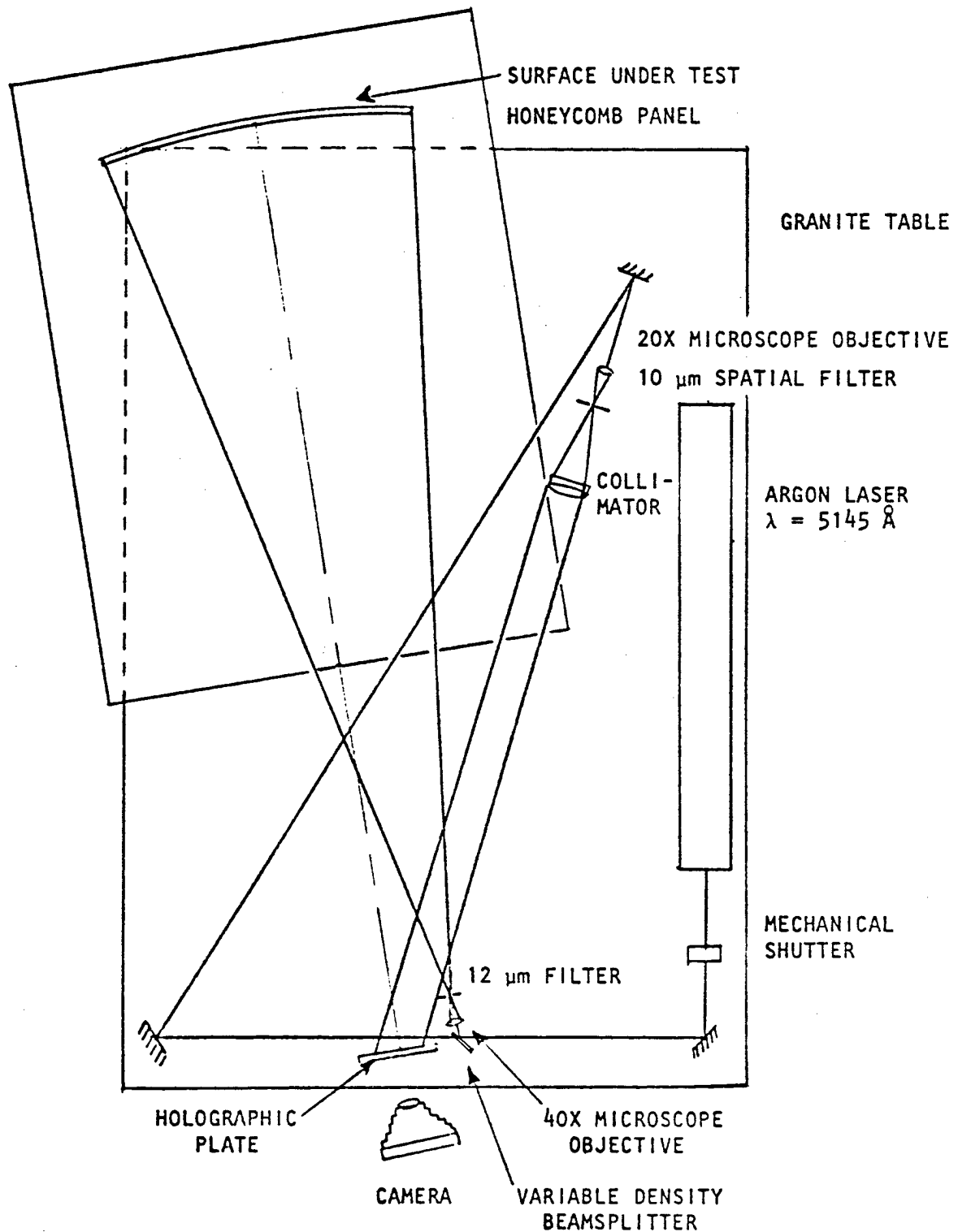


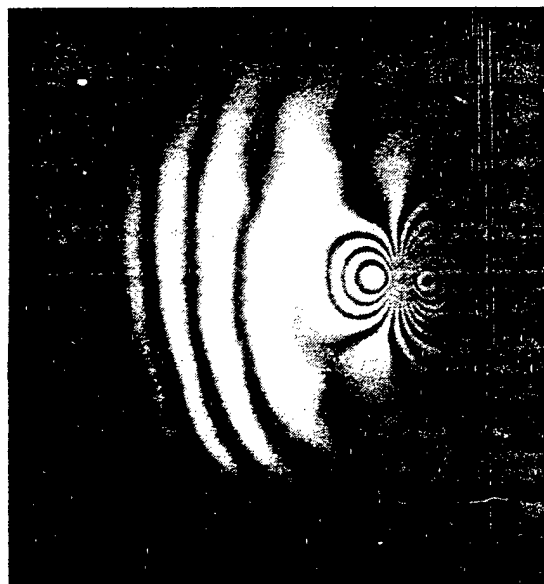
Fig. 2.4. Schematic Layout of Holographic Interferometric Test of 60-cm Active Mirror Model.

The deformation produced by a radial slope change also at the 0.4 zone is shown in Fig. 2.5(b). The result of a small-z-displacement is shown in Fig. 2.6(a) and a large z-displacement is shown in Fig. 2.6(b). Again, the fringe shapes are more or less as predicted (compare Figs. 2.7(c) and 2.7(a)). The reactions of the passive actuators are clearly seen in Fig. 2.6(b). It should be noted that the peak occurring at about six o'clock at the 0.4 zone is not an actuator reaction, but an artifact introduced by the experimenter while demonstrating the real-time nature of the holographic interferometry--finger pressure on the back of the shell, estimated at 5 to 10 lb, apparently produced a permanent deformation in the form of a dimple. It was subsequently removed by making a new hologram.

Surface profiles along the axes of symmetry in the direction of the slope changes were computed by hand for the tangential slope change mode of Fig. 2.5(a) and for the radial slope change mode of Fig. 2.5(b) at the 0.4 zone. These profiles are plotted in Figs. 2.10(a) and 2.10(b) along with the corresponding computer predictions. The theoretical curve for Fig. 2.10(a) is symmetric about the origin to the accuracy of the naked eye. In actuality the structure is not perfectly symmetric due to the inclusion of the three active actuators with flexures in their actuator posts, but this only slightly changes the stiffness characteristics of the structure. The experimental curve for the same case is definitely not symmetric. Since the structure is designed to be symmetric, except for the aforementioned active actuators, either 1) the interferometric test data is in error or, 2) the construction of the physical model produced the discrepancy. It is far more likely



(a) Tangential.



(b) Radial.

Fig. 2.5. Slope Changes, 0.4 Zone.



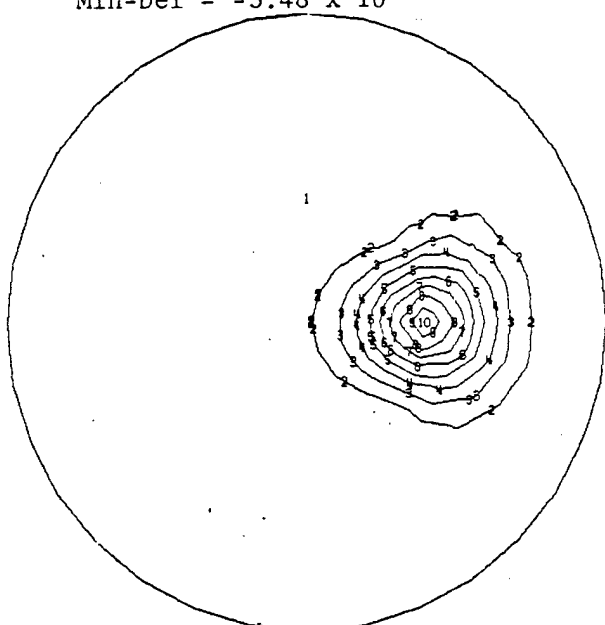
(a) Small displacement (no tilt).



(b) Large displacement (28 fringes).

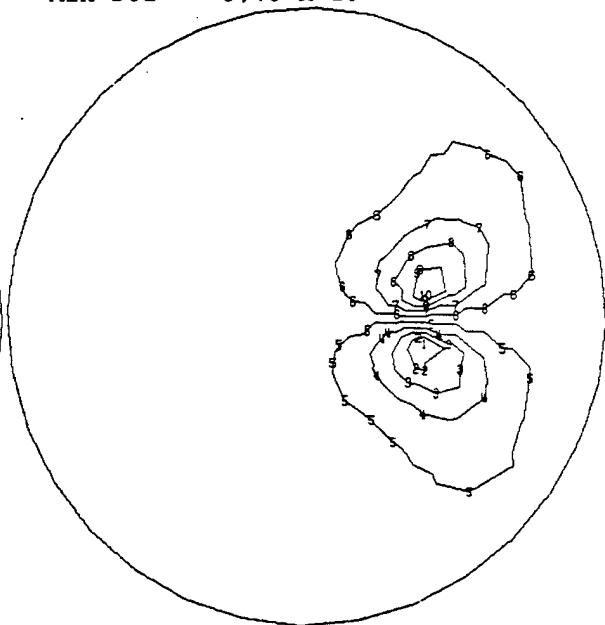
Fig. 2.6. z Displacement, 0.4 Zone.

Max-Def = 1.24×10^{-4}
Min-Def = -3.48×10^{-6}



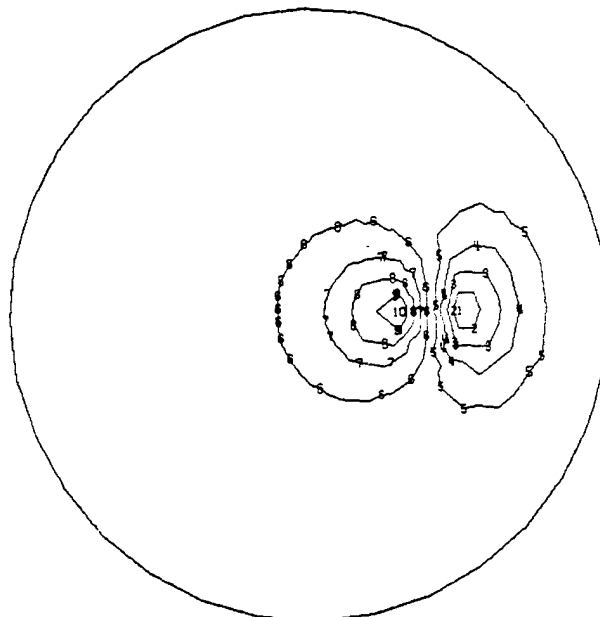
(a) Normal Position Control

Max-Def = 6.46×10^{-6}
Min-Def = -6.46×10^{-6}



(b) Tangential Slope Control

Max-Def = 9.47×10^{-6}
Min-Def = -9.66×10^{-6}

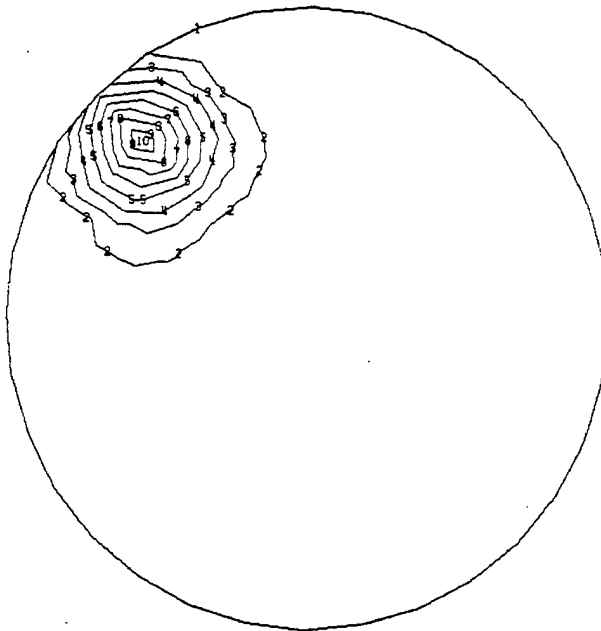


(c) Radial Slope Control

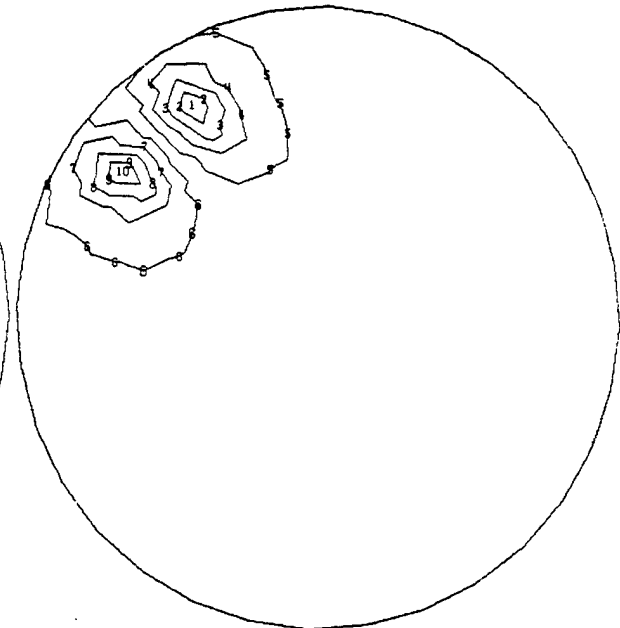
Fig. 2.7. 41-Actuator System, 0.4 Zone.

Max-Def = 1.47×10^{-4}
 Min-Def = -6.87×10^{-6}

Max-Def = 5.20×10^{-6}
 Min-Def = -5.20×10^{-6}

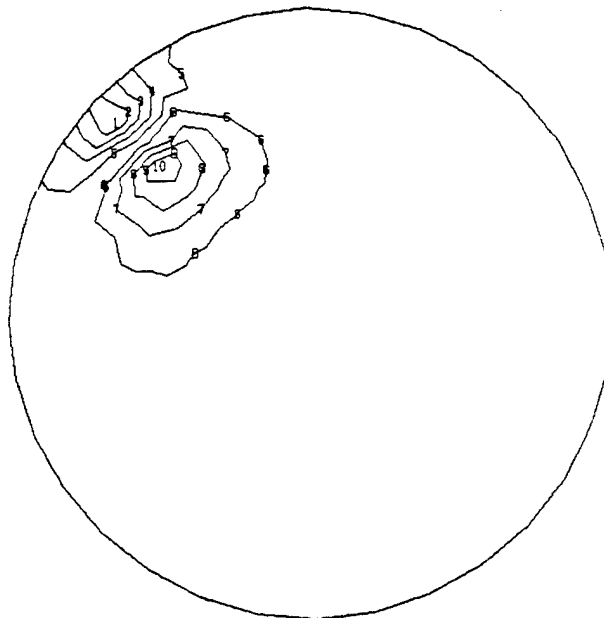


(a) Normal Position Control



(b) Tangential Slope Control

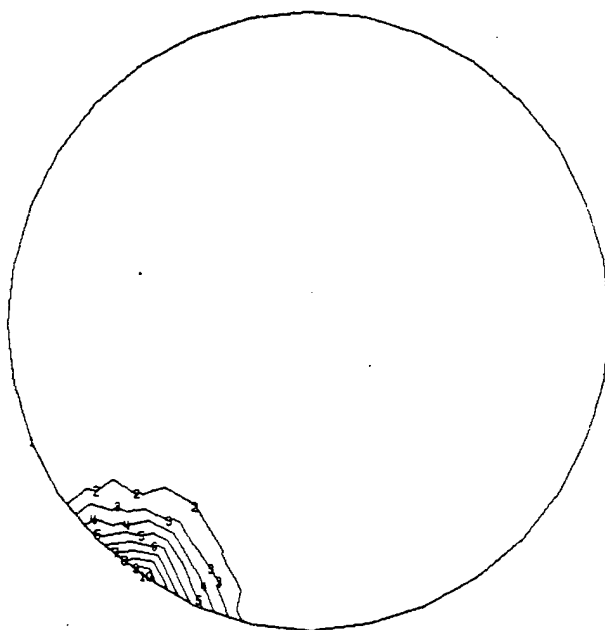
Max-Def = 8.38×10^{-6}
 Min-Def = -8.17×10^{-6}



(c) Radial Slope Control

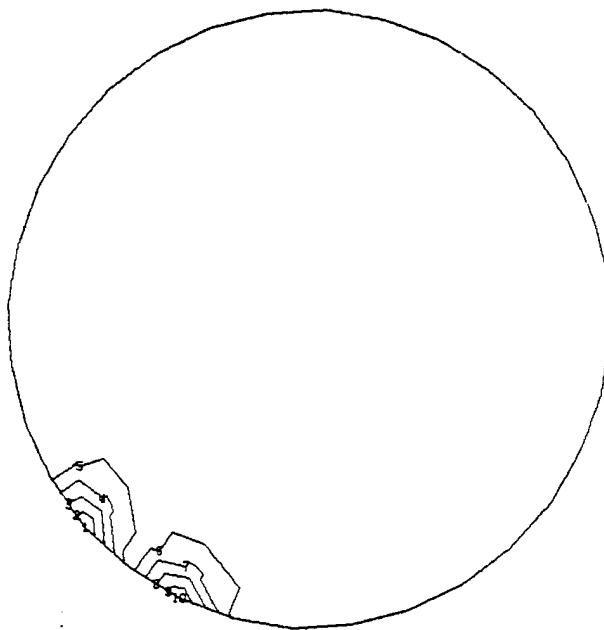
Fig. 2.8. 41-Actuator System, .8 Zone.

Max-Def = 2.08×10^{-4}
Min-Def = -5.94×10^{-6}



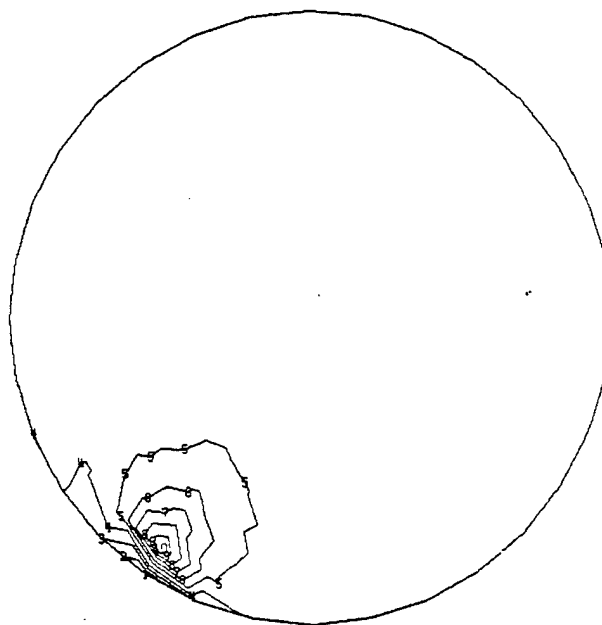
(a) Normal Position Control

Max-Def = 1.24×10^{-5}
Min-Def = -1.32×10^{-5}



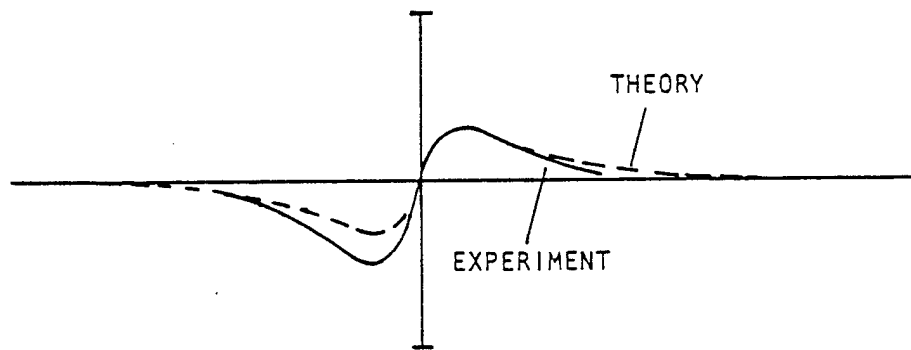
(b) Tangential Slope Control

Max-Def = 4.76×10^{-6}
Min-Def = -3.00×10^{-6}

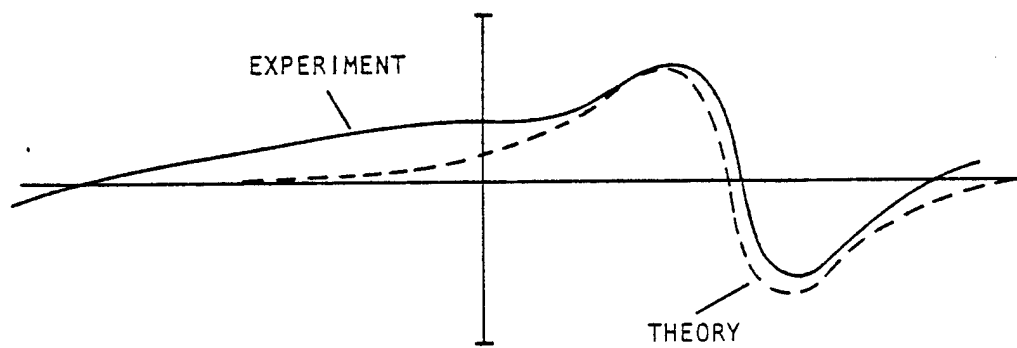


(c) Radial Slope Control

Fig. 2.9. 41-Actuator System, 1.0 Zone.



(a) Tangential Slope Change



(b) Radial Slope Change

Fig. 2.10. Surface Profile Through Axis of Symmetry, 0.4 Zone.

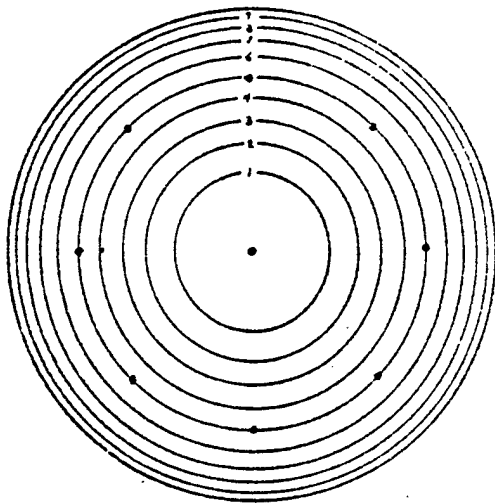
that the latter is the cause. In the interests of simplicity and due to its small size, the 60-cm model relied chiefly upon friction and close mechanical fits to keep structural members connected and aligned. Slippage of two adjacent members probably accounts for the difference between the theoretical and experimental curves in Fig. 2.10(a). (It is appropriate to note that in solving this problem the design of a full size 40-actuator system incorporates mechanical flexures and bonding as demonstrated in Figs. 5.5-5.7 .) For the same reasons that there was not exact correspondence in the tangential slope control, there is not exact correspondence in the radial slope change curves in Fig. 2.10(b). In any event the remarkable correspondence demonstrated gives credence to the finite element modeling techniques and to the concept of an integrated active mirror system.

A much more detailed accounting of the mechanical design of the demonstration model, holographic interferometry of the model and comparison of results with a previous SAP IV mathematical model that is not as accurate as the current NASTRAN model are included in Shannon and Smith (1978).

Mirror Scallop

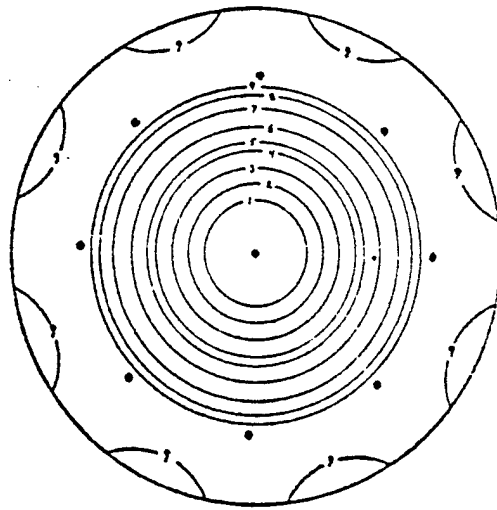
During the evolution of the 40- and 41-actuator systems, a finite element study and a test of a physical model were conducted for a 9-actuator integrated active mirror system (Koterwas, 1974). The f/1.5 spherical mirror for that system had a 12 in. diameter, was .08 in. thick and had no center hole. An analytical attempt was made to defocus the mirror. Fig. 2.11(a) shows a contour plot of the intended defocus, and Figs. 2.11(b) and (c) show the mirror surface under active control and illustrates scallop. To deform the model, the nine actuators shown by dots were given the same normal translations and slopes in Fig. 2.11(b) as occur in Fig. 2.11(a). The error at the outer edge of the mirror is nearly 58%. Unacceptable error occurred because for defocus the mirror has to take a nondevelopable shape, i.e. one in which the middle surface of the mirror is stretched. By increasing mirror thickness to .8 in. and later using a lightweight mirror, the magnitude of defocus errors was reduced to 15% and 22% respectively, with scalloping being dramatically reduced. The same 9-actuator system worked much better when the active controls deformed the thin mirror into the shape of astigmatic aberration. In that case the enforced shape is developable, i.e., the middle surface is not stretched and there are no membrane forces. The maximum error for astigmatism is less than 12%. In order to enforce nondevelopable shapes and to correct mirror distortions that exhibit significant outer edge wrap, while at the same time minimizing mirror and system weight, more active control points need to be added at and near the outer edge

Datum = 0.0
 Contour Interval = 3.60
 $w(x, y) = (1)(x^2 + y^2)$

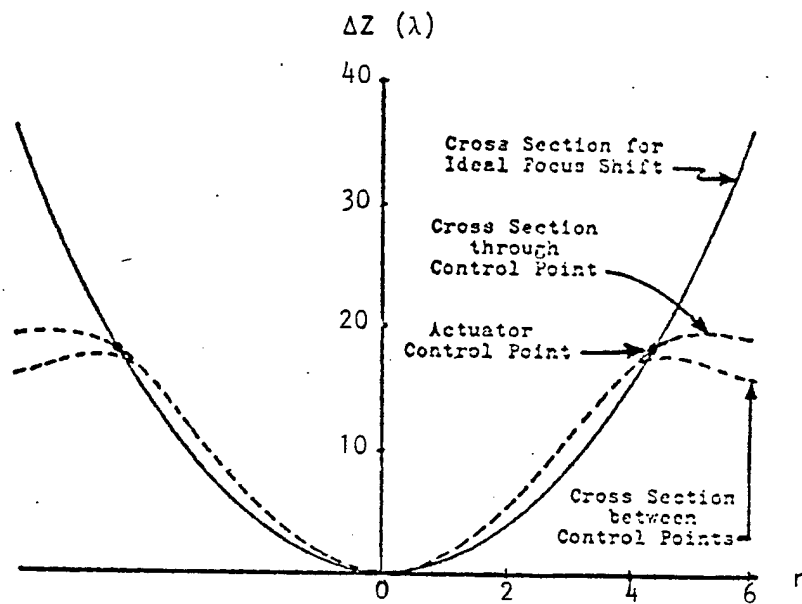


(a) Ideal Focus Shift

Datum = 0.0
 Contour Interval = 1.92
 Mirror Thickness = .08 in



(b) Thin Mirror with Focus Shift



(c) Cross Sections of Thin Mirror with Focus Shift

Fig. 2.11. Scallop of a Thin Mirror for a 9-Actuator System with a Focus Shift.

of the mirror. These control points have been incorporated into the 40- and 41-actuator systems.

Causes of scallop are discussed in more detail in Chapter 4 under the heading "Defocus and Astigmatism."

CHAPTER 3

PRELIMINARY STUDIES

In retrospect, the decision to undertake SAP IV analyses of a 2-dimensional representation of the integrated active mirror system proved to be one of the most significant factors leading to the successful completion of analyses of a 3-dimensional system model. The decision was made when computer time was not available for the MSC/NASTRAN finite element program used for analyses of the 3-dimensional model. This delay in availability of computer resources turned out to be a fortuitous circumstance. The 2-dimensional analyses were performed with SAP IV on a time sharing computer system at the University of Arizona. A DEC 10 computer was used to interactively build models, to submit them for execution in batch mode on a CYBER 175, and to examine results in files shipped back to the DEC 10. For a small 2-dimensional model, the analysis was truly an interactive process, and the quality and quantity of the results obtained exceeded all prior expectations.

The webbed core of sandwich plates was represented in 3-dimensional finite element models by an equivalent homogeneous solid material. The equivalent shear modulus for the solid material was derived and tested on flat plate models.

Finite element modeling of flat plates representative of solid and sandwich mirrors was initiated using the SAP IV program (Bathe, Wilson, and Peterson, 1973) on the University of Arizona CDC Cyber 175 computer. Costs of running SAP IV analysis were approximately \$125 per run. It became clear at this point that the analysis of the 40-actuator system would be prohibitive using SAP IV. By switching to the MCS/NASTRAN program (Joseph, 1979) on the Air Force Weapon's Laboratory CDC Cyber

176 computer, the cost of the same flat plate model was approximately 10% of the SAP IV amount. Results for flat plate models show excellent correlation with analytical results.

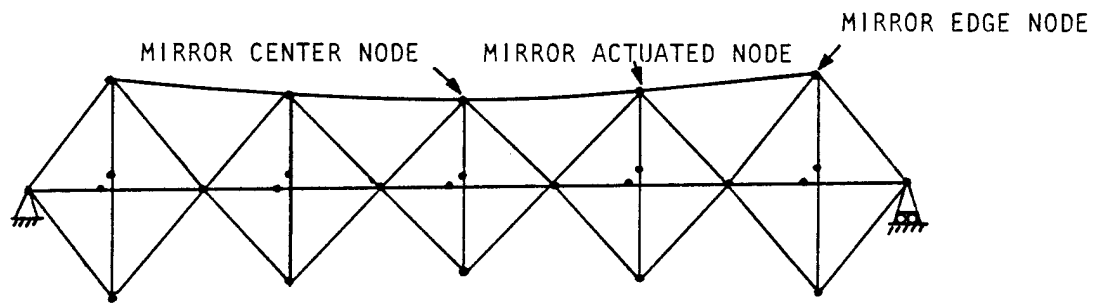
Analysis of 2-Dimensional Model of an Integrated Active Mirror System

The 2-dimensional finite element models were used to study normal position control, in-plane slope control, structural member connectivity, and various types of loads. The SAP IV program was used exclusively.

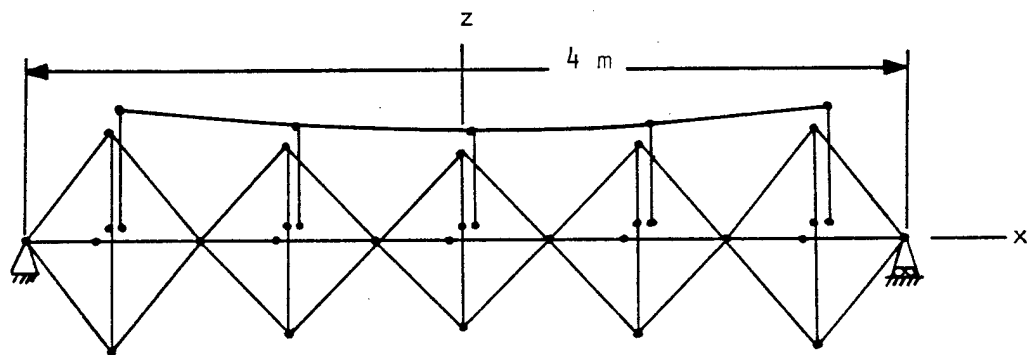
Finite Element Models

Models used in the 2-dimensional analysis are shown in Fig. 3.1. They represent the structure within a diametrical slice taken out of a 41-actuator system, since the 40-actuator system with its annular mirror does not have a central actuator. Nevertheless, since the structure must include this central actuator to be continuous in a 2-dimensional model, and since the integrated active mirror system designed in this study has 40 actuators and an annular mirror, the assumption was made that the lessons learned from study of the 41-actuator system would apply equally to the 40-actuator system.

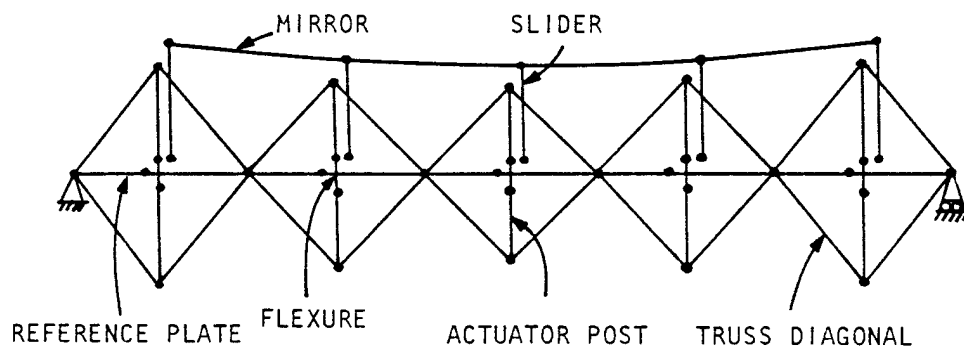
In order to reduce the size of the mathematical model so that it would be an effective interactive tool, the ends of the mirror between the outside actuator posts and the outside edge of the actual mirror were neglected (to see this compare Fig. 3.1(a) with Fig. 2.1(b)), and no nodes were included in the mirror sections between the actuator posts. The ends of the mirror were eliminated since they were outside the support



(a) Model for Cases 1, 2, 3, 4, and 7.



(b) Model for Cases 5, 6, 8, 9, and 12.



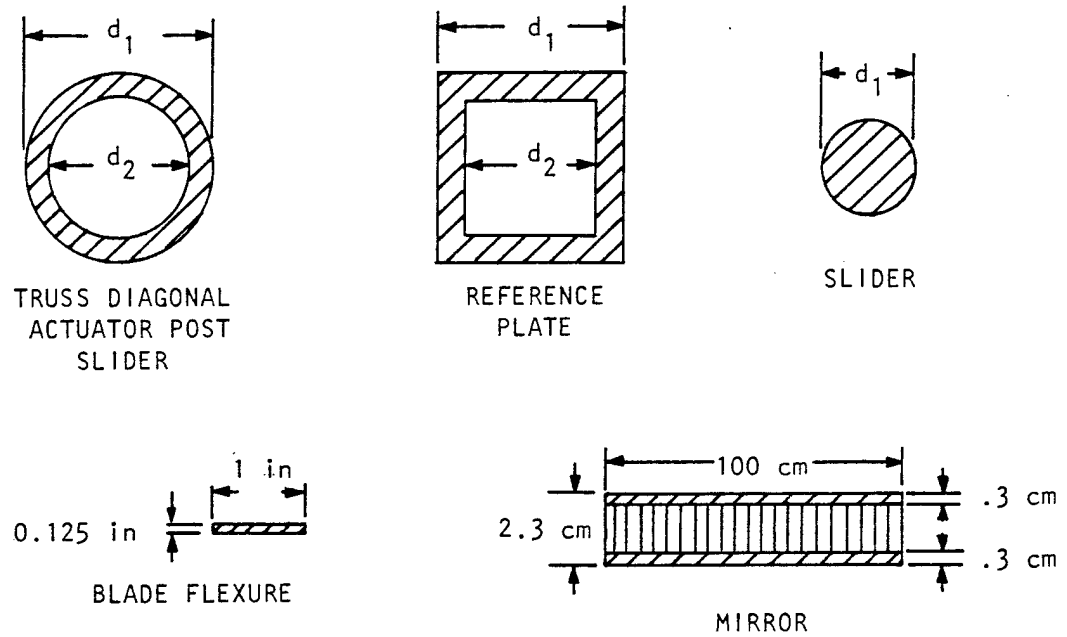
(c) Model for Cases 10 and 11.

Fig. 3.1. 2-Dimensional Finite Element Models.

points and would affect deflections of the remainder of the mirror only for certain loads. The lack of intermediate mirror nodes between actuator posts makes small reductions in accuracy, due to the curved surface of the mirror being represented by four flat segments.

In Fig. 3.1(a) the tops of the actuator posts attach directly to the mirror. At the intersections of the actuator posts and the reference plate there are separate nodes for each structure. The separate nodes, which actually coincide, are shown slightly offset in the figure. In Fig. 3.1(b) sliders have been added. The top of a slider attaches to the mirror and the bottom to an actuator post. Again the nodes have been offset for clarity, whereas in actuality a slider moves up and down inside an actuator post as seen in Fig. 5.5. In Fig. 3.1(c) flexures have been added to the actuator posts. The tops of the sliders act as if they pass through frictionless sleeves in the tops of the actuator posts, and the bottoms of the sliders are rigidly attached to the middle of the actuator posts. The connectivity of degrees of freedom between reference plate and actuator post nodes varies, and will be documented for each individual case. The translational degrees of freedom are x and z and the rotational degree of freedom, yy , is a rotation about the y axis and is positive clockwise.

The structural members representing the reference plate, actuator posts, sliders, and mirror are beams. The truss diagonals will be modeled as SAP IV truss elements until noted otherwise. Cross-sections of these structural members are described in Fig. 3.2. For each member except the mirror, three different sets of dimensions are given,



(a) Cross Sections.

Member		d_1 (in)	d_2 (in)
Truss Diagonal	- Small	.25	.125
	- Nominal	.5	.25
	- Large	1.	.5
Actuator Post	- Small	.5	.25
	- Nominal	1.	.5
	- Large	2.	1.
Slider	- Small	.25	—
	- Nominal	.5	—
	- Large	1.	.5
Reference Plate	- Small	2.	1.5
	- Nominal	3.	2.
	- Large	5.	3.5

(b) Cross Section Dimensions.

Fig. 3.2. Structural Members for 2-Dimensional Model.

i.e., small, nominal and large. These different dimensions were needed for studies to minimize the size of the structural members. The nominal cross-section dimensions and the material properties are the same as those called Property Set 7 in a prior report (Shannon, Richard and Hansen, 1980), since the original intent of the 2-dimensional analyses was to optimize the structure designed in that study. The mirror is made of fused silica, and the remainder of the structure is constructed out of a graphite epoxy composite.

Normal Position Control

The 2-dimensional models were first used to study various forms of normal position control, since this is the primary means of mirror figure control with slope control being secondary. Seven of the cases studied are shown in Fig. 3.3. This figure shows the loads used to model the active actuator, describes the connectivity between actuator posts and the reference plate, and gives results of analyses in terms of a ratio of the z displacements of two mirror nodes. A small displacement ratio is desirable, and it occurs if the deformation of the mirror is localized to the vicinity of the active actuator. Refer to the complete models in Fig. 3.1 and note that an active actuator from Fig. 3.3 is the second actuator from the right.

Cases to be discussed first are those described by Fig. 3.1(a). For Cases 1 and 2 of Fig. 3.3 the actuator posts pass through clearance holes in the reference plate. In Case 1 the actuator post is heated so that it expands and deflects the mirror upward. This type of loading was used by Radau (1977), by Shannon and Smith (1978) and by Shannon, Richard and Hansen (1980). Optimization curves were generated for this

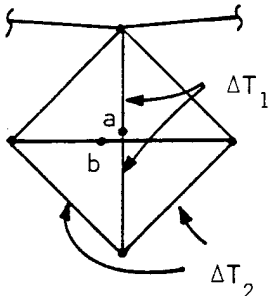
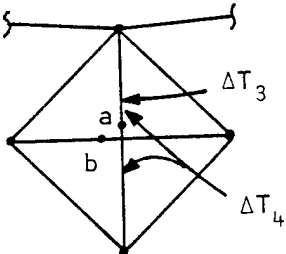
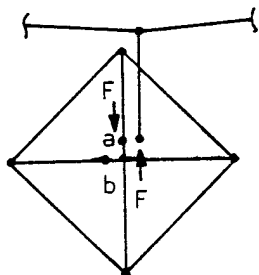
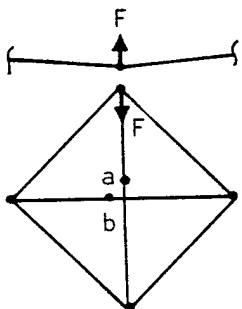
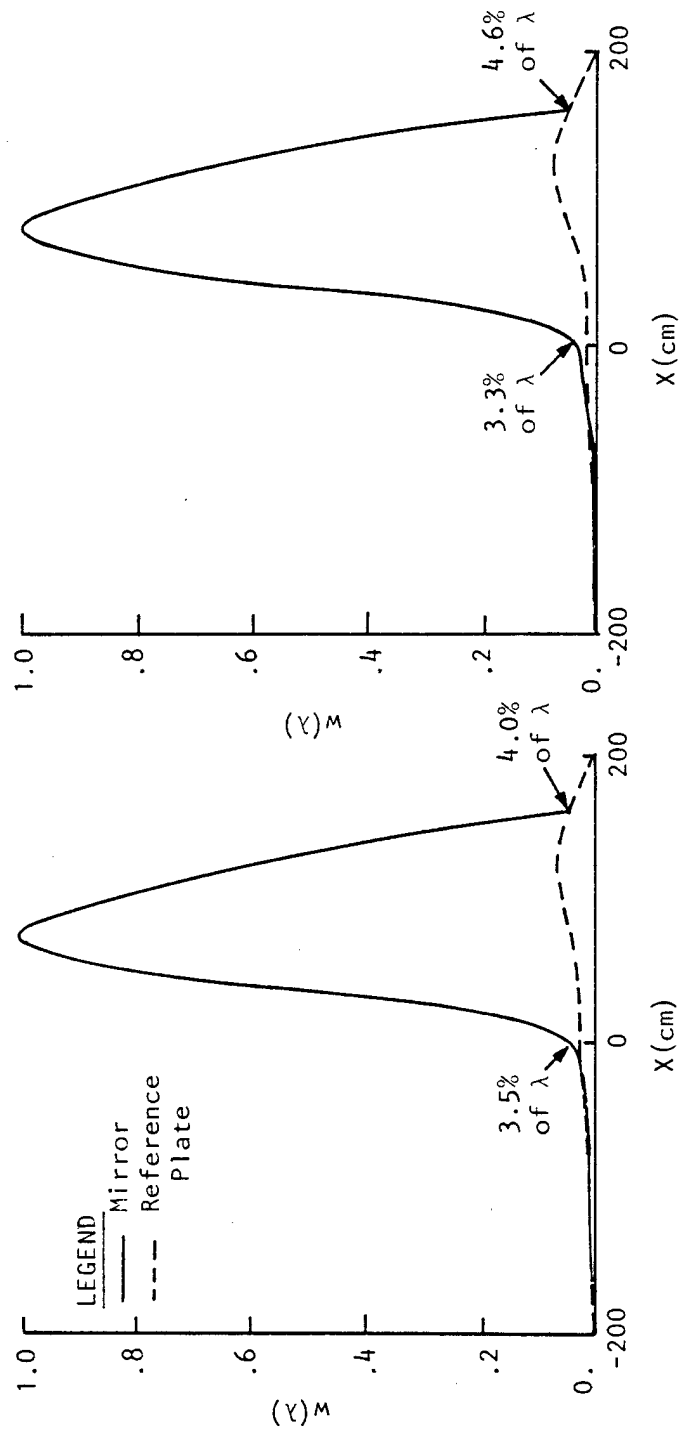
Active Actuator	Degrees of Freedom Connected between Actuator Post Node a and Reference Plate Node b	$\frac{w_{\text{mirror center node}}}{w_{\text{mirror actuated node}}}$
	None	Case 1 7.6% Case 2 7.6%
	x, z, yy	Case 3 11.0% Case 4 6.9%
	Case 5 - x Case 6 - x, z, yy	Case 5 3.5% Case 6 9.7%
	x	Case 7 8.6%

Fig. 3.3. Models for Study of Normal Position Control.

case, since it has been the primary mode of normal actuation in previous works, and these curves will be discussed later. For Case 2, if both of the lower truss diagonals are cooled, the mirror node again moves upward. This type of loading was used by Koterwas (1974). For Cases 3 and 4 the actuator post and reference plate are rigidly attached to one another. When only the top half of the actuator post is heated in Case 3, the reference plate is bent severely, and mirror deformations are not as localized as when the entire actuator post is heated in Case 4. In all previous cases thermal loads have been applied to the models, but these loads model any type of servomechanism used to change the lengths of the thermally existed structural members. In Case 7, instead of using thermal loads, a mechanical device is inserted between the mirror and the top of the actuator post, and this device forces the two members apart.

Next, slides were added to the model as shown in Fig. 3.1(b). A servomechanism is inserted between the bottom of the slider and the actuator post. The only difference between Cases 5 and 6 is the connectivity of the actuator posts with the reference plate. It is beneficial to uncouple these structures. For Case 5 the actuator post and reference plate are attached for translational motion in the plane of the reference plate, since this is a requirement of the usual method of in-plane slope control. Figure 3.4(a) shows mirror and reference plate deflections for Case 5. The fact that mirror deformations are localized about the active actuator and are only 3.5% and 4.0% of maximum at the two adjacent inactive actuators, demonstrates the effectiveness of an



(a) Nominal Reference Plate.

(b) Small Reference Plate.

Fig. 3.4. Case 5 Mirror and Reference Plate Deflections.

integrated active mirror system. This localization yields a minimization of coupling between the active controls, making design of a relatively simple and effective control system possible.

Analyses for Cases 1 through 7 all involved use of nominal structural members. By reexecuting the analyses for Cases 1 and 5 six times, each time substituting one structural member that is either small or large as defined in Fig. 3.2, the optimization curves of Fig. 3.5 were generated. Six variations were sufficient for Case 5, because the actuator post and slider combination was varied as a unit, e.g. the small post and small slider were always used together. Three curves appear for each case: one for the ratio of mirror center node to mirror actuated node displacements, one for the ratio of mirror edge node to mirror actuated node displacements, and one for system weight. Each curve was generated from three data points. The weight curves for Cases 1 and 5 are so similar that they appear as one curve in each of the three sets of curves. Of course the system weight is most appreciably affected by reduction in the cross-sectional area of the reference plate members, as can be seen from the lower set of curves.

For Case 1 the upper and lower sets of curves in Fig. 3.5 demonstrate that the displacement ratio improves, i.e., decreases, when the area of the truss diagonals is reduced and when the reference plate area is increased. The truss diagonals are counterproductive here. The larger their dimensions, the greater is the required force of actuation, and this load increases faster than the stiffness. As the area of the truss diagonals becomes smaller and smaller, the mirror and reference plate begin to act as two distinct structures separated by actuator posts, each relying more and more upon its

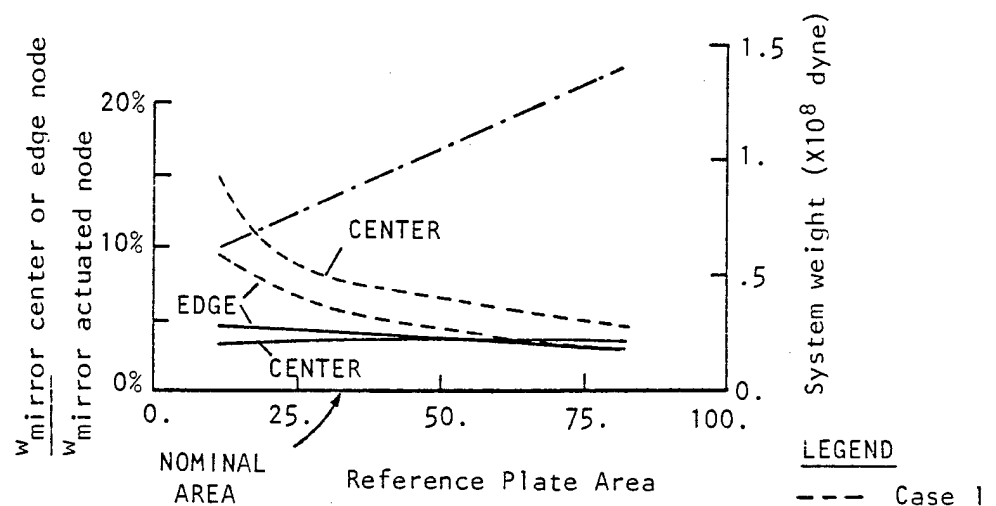
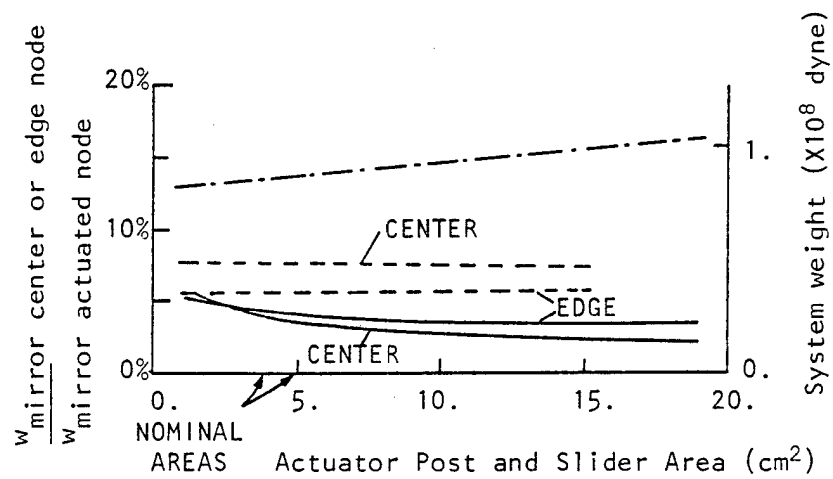
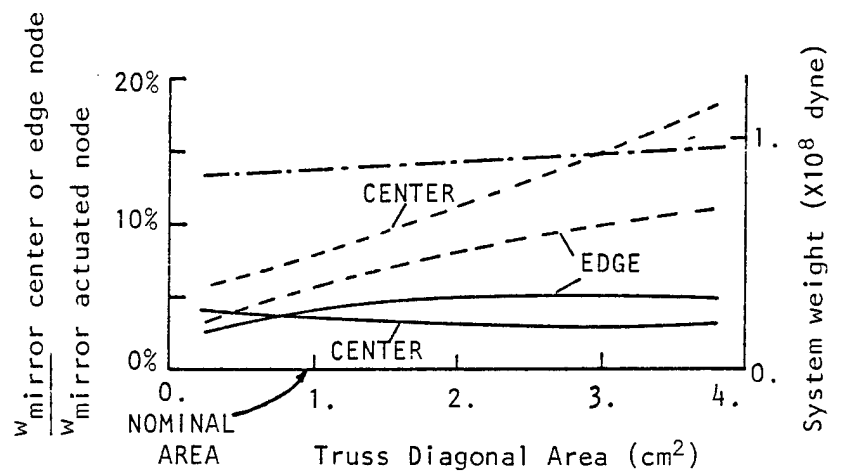


Fig. 3.5. Optimization Curves for Case 1 and Case 5.

individual bending stiffness to resist deflection. Evidence that the reference plate is bending is the severely nonlinear increase in deflection brought about by decrease in reference plate area. Since the goal of the integrated active structure is to minimize weight and maximize stiffness by carrying loads in membrane action, Case 1 is rejected from further study.

Behavior of Case 5 is far superior to that of Case 1. The Case 5 curves in Fig. 3.5 most insensitive to reduction in area are those plotted versus reference plate area. Since the reference plate members are the largest, it is implied that membrane action is predominant. It was not determined how much smaller the reference plate could be made without adverse effects, but if the membrane stiffness of the mirror and reference plate are made equal, the reference plate area can be found from

$$A_{\text{Ref plate}} = \frac{(AE)_{\text{mirror}}}{E_{\text{Ref plate}}} .$$

Fig. 3.4(b) shows mirror and reference plate deflections for a small reference plane with other members having nominal dimensions. The mirror curve is nearly indistinguishable from the curve for the nominal reference plate, however the reference plate deformation shows that localized bending is increasing.

Two simple explanations of why Case 5 is superior to Case 1 are:

- (1) that the reaction force pushing against the support structure is input directly into the reference plate in Case 5 and only indirectly in Case 1 and these reaction forces resist reference plate deformation and,
- (2) that for Case 5 the actuation forces are only 2% of those needed in Case 1 to produce equal mirror displacements, resulting in less reference plate distortion.

As a result of this study, the structure for the 3-dimensional model will include sliders and the reference plate will be attached to the actuator posts via annular flexures seen in Fig. 5.5. These flexures allow rotation and vertical translation of the actuator post with respect to the reference plate.

Slope Control

In-plane slope control can be effectively studied with the 2-dimensional model, but out-of-plane slope control cannot. Four cases of in-plane slope control are shown in Fig. 3.6. All of these cases include sliders, since normal position control was most effective with sliders. Displacement ratios in the figure are given each time for nominal structural members, and if ratios are available for structures with a small reference plate, they are presented in parentheses.

For available data the displacement ratio increased by about 5.% when the reference plate was changed from nominal to small dimensions, even though the bending stiffness of the small reference plate is only 17.% of that of the nominal plate. This reinforces the fact that for an integrated active mirror system the most important load carrying mechanism is membrane action rather than bending. The shapes of the plots of mirror and reference plate displacement were virtually unaffected by the switch in reference plates.

The plots of mirror displacement were more difficult to obtain for slope control than for normal control. For normal position control the maximum mirror displacement occurs at the actuated node, but for slope control the maximum occurs somewhere in the two beams adjacent to the actuated node. To find the maximum displacements and other intermediate displacements for curve sketching an auxiliary computer program was

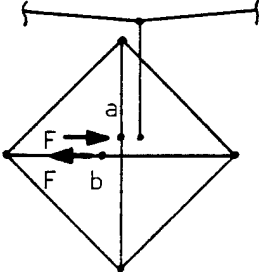
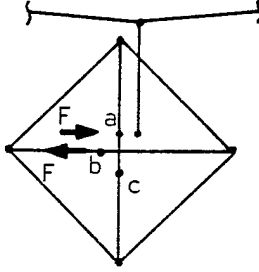
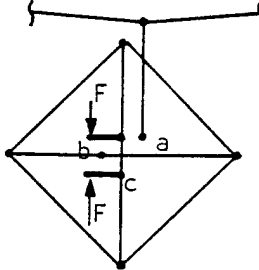
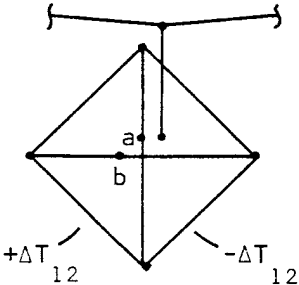
Active Actuator	Degrees of Freedom Connected between Actuator Post Node a and Reference Plate Node b	$\frac{w_{\text{mirror center node}}}{w_{\text{mirror actuated node}}}$
	x (for nonactuated trusses)	Case 8 20.0% (21.0%) (No pins at nodes a) Case 9 13.0% (pins at nodes a)
	x (for nonactuated trusses)	Case 10 13.5% (14.2%)
	None	Case 11 7.9%
	None	Case 12 8.0%

Fig. 3.6. Models for Study of In-Plane Slope Control.

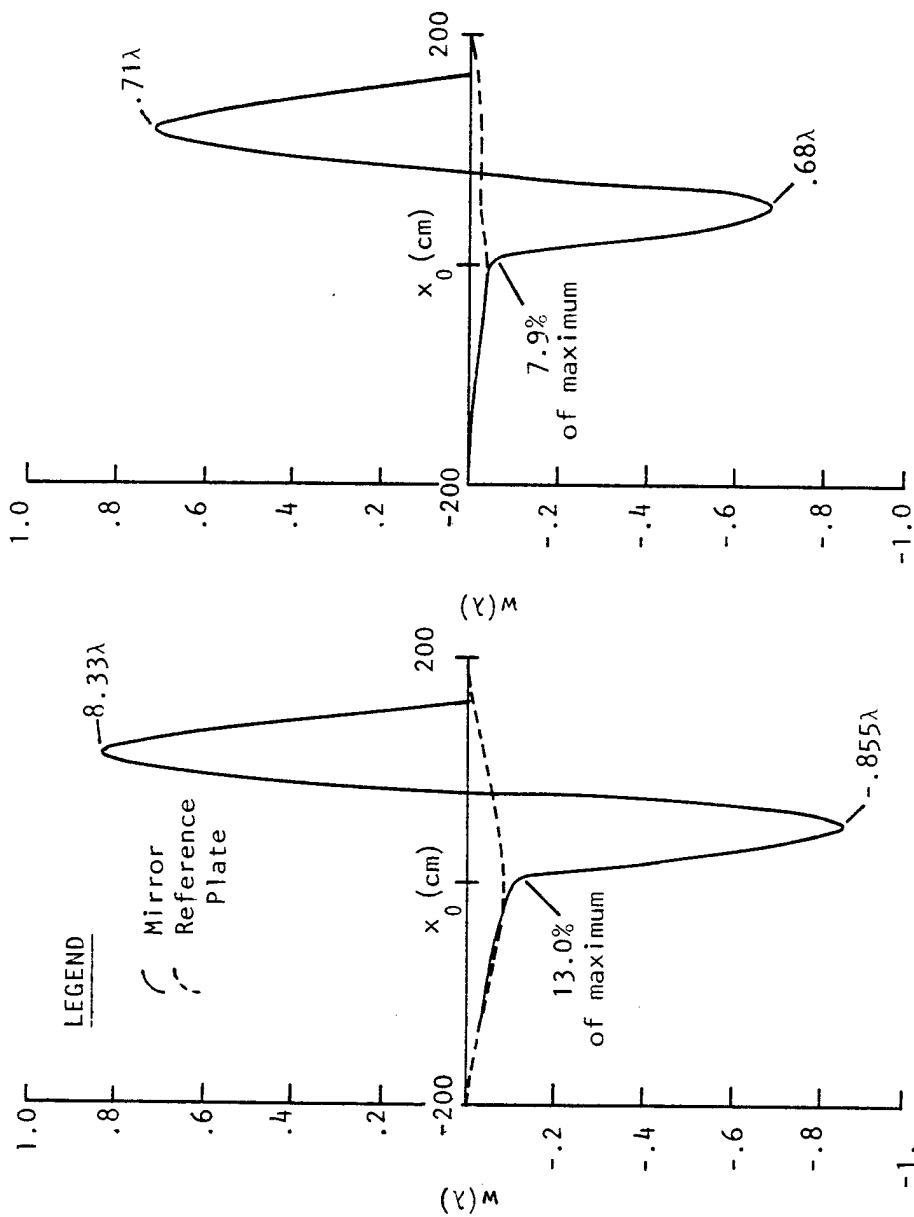
written. The program transformed the displacements of two nodes of a beam representing a mirror segment from global to local coordinates, used these local coordinates to evaluate the beam shape function (Cook 1974, p. 70), and then found the intermediate displacements from the shape function.

In Cases 8, 9, and 10 a servomechanism is inserted between the actuator post and the reference plate. These cases differ only in their treatment of the actuator post. In Case 8 the actuator post is a continuous, hollow tube from top to bottom. This type of modeling was used by Radau (1977), by Shannon and Smith (1978) and by Shannon, Richard and Hansen (1980). Since relatively large forces are needed to bend the actuator post in order to cause tilt at the mirror surface, this case has an unacceptable displacement ratio of 20%. In order to decrease the force of actuation, a pin joint is added to the actuator post at node (a) for Case 9 in Fig. 3.6, and the displacement ratio is significantly reduced. For the pinned post, actuation forces are one-third of the forces needed with a continuous post for equal mirror rotations, resulting in less reference plate distortion and thereby a smaller displacement ratio. In an optical structure where extremely small displacements and rotations are critical, the play in a traditional pin joint cannot be tolerated. Therefore it is effective to physically replace the pin with a blade flexure aligned to have little stiffness resisting in-plane rotations of the two sections of the actuator post, but with substantial stiffness resisting out-of-plane rotations. In Case 10 the flexure is modeled as a beam located between nodes (a) and (c) in Fig. 3.6, and the displacement ratio is only 3.8% larger than for Case 9 with the "ideal pin" joint. The increase is due to the fact that the flexure resists in-plane rotation a

small amount, whereas the frictionless pin joint has zero resistance to rotation. Figure 3.7(a) presents curves of deflections for Case 9. The shapes of the curves for Cases 8 and 10 are nearly identical to that for Case 9. Of course angles in the plot are greatly exaggerated. The slope of the mirror at the actuated node is actually only 3.7 μ rad.

Cases 11 and 12 present two entirely different methods of inducing in-plane slope control. In Case 12 the lower right hand truss diagonal in Fig. 3.6 is cooled while the lower left hand truss diagonal is heated, thereby shifting the lower end of the actuator post to the right. The actuator post has no pin or flexure, and it forces the mirror to rotate. The deflection ratio for this case is much less than those cases previously discussed. A disadvantage of this method is that it would be paired with the Case 2 method of normal position control which was shown to be only mediocre in performance. Since normal position control is of primary importance, the method in Case 12 was not implemented in 3-dimensional studies here, however this method was studied by Koterwas (1974).

Case 11 represents a new approach to in-plane slope control. It employs a flexured actuator post loaded by a servomechanism offset from the axis of the post so that both forces and couples are applied. The couples rotate the post and mirror. The displacement ratio here is the lowest reported. The deflections are plotted in Fig. 3.7(b). To explain the improved performance, consider the forces acting at the ends of the reference plate in Fig. 3.6. The upper half of the actuator post rotates counterclockwise a smaller angle than the lower half of the post rotates clockwise, since the upper half is resisted by the mirror. Thus the resultant force of the left node of the reference plate is up while the resultant force at the right end is down. The torque from



(a) Case 9 with Nominal Reference Plate.
 (b) Case 11 with Nominal Reference Plate.

Fig. 3.7. Cases 9 and 11 Mirror and Reference Plate Deflections.

this effect is clockwise, reducing the overall counterclockwise rotation of this section of the reference plate and forcing the mirror deflection to be more localized. This same clockwise torque on the reference plate occurs in Case 12. For Case 11, if the actuator post and reference plate are attached in the x degree of freedom, the deflection ratio balloons to 29.%. If a servomechanism could be devised to apply a torque to the actuator post and react the torque directly into the reference plate, while at the same time not constraining horizontal translation of the actuator post, the displacement ratio could probably be reduced to less than one third that of Case 11.

Case 9 was utilized for in-plane slope control in the 3-dimensional model in this study. Future studies should definitely exploit Case 11.

Structural Member Connectivity

The 2-dimensional model was next used to study variations in the connectivity of different structural members. It has already been shown that for in-plane slope control modeling a blade flexure as a pin changed the deflection ratio for the mirror center by only 3.8%. It was necessary to see what effect the flexible joint would have on normal position control of Case 5. The model with the small reference plate was reexecuted with blade flexures in the middle of the actuator posts. The new curves so closely resembled the displacement curves for the post without a flexure as shown in Fig. 3.4(b), that they were indistinguishable from one another. Subsequently, the flexural joints in the 3-dimensional system were modeled as pins, thereby significantly reducing the size and complexity of that model.

Table 3.1 gives the displacement ratio at the mirror center for six variations of Case 5, all utilizing a small reference plate. Number 1 is the same as Case 5 with a small reference plate. Variation 2 shows what happened when the blade flexures were added to the actuator posts, as discussed in the previous paragraph. Variation 3 and 4 are concerned with changes in the connections between the actuator post and the slider. For 3 the tops of the sliders and actuator posts are disconnected, so the sliders pass through clearance holes in the actuator posts rather than through frictionless sleeves. The separation caused the mirror to decouple from the support structure, making results totally unsatisfactory. For 4 the bottom of the slider was disconnected in all degrees of freedom except z translation. In variations 5 and 6 the truss diagonals were changed from truss to beam elements, i.e., they were able to resist bending, and the actuator post and slider connections were varied. Variations 4 thru 6 are all satisfactory.

The changes in variation number 6 of the normal position control model were made to the slope control model. Previous results in Fig. 3.6 showed that for a flexured actuator post and a small reference plate that the displacement ratio was 14.2%. With the additional changes noted in variation number 6, the results were identical to three significant figures, i.e., the displacement ratio was still 14.2%.

Conclusions drawn from these variations affect both the mechanical design of the structure and the resulting 3-dimensional analysis. They imply that: (1) the connection between the top of an actuator post and a slider is critical and will be maintained in the mechanical design by the twin

Table 3.1. Variations of Case 5 Normal Position Control Model.

Number	Flexure	SAP IV Element Used to Model Truss Diagonals	Degrees of Freedom Connected Between Tops of Actuator Posts and Sliders	Degrees of Freedom Connected Between Middle of Actuator Posts and Bottom of Sliders	Mirror Center Node	
					w_{Mirror}	Actuated Node
1	No	Truss	x, yy	x, z, yy	3.29%	
2	Yes	Truss	x, yy	x, z, yy	3.36%	
3	Yes	Truss	None	x, z, yy	21.6 %	
4	Yes	Truss	x, yy	z	3.37%	
5	Yes	Beam	x, yy	x, z, yy	3.35%	
6	Yes	Beam	x, yy	z	3.35%	

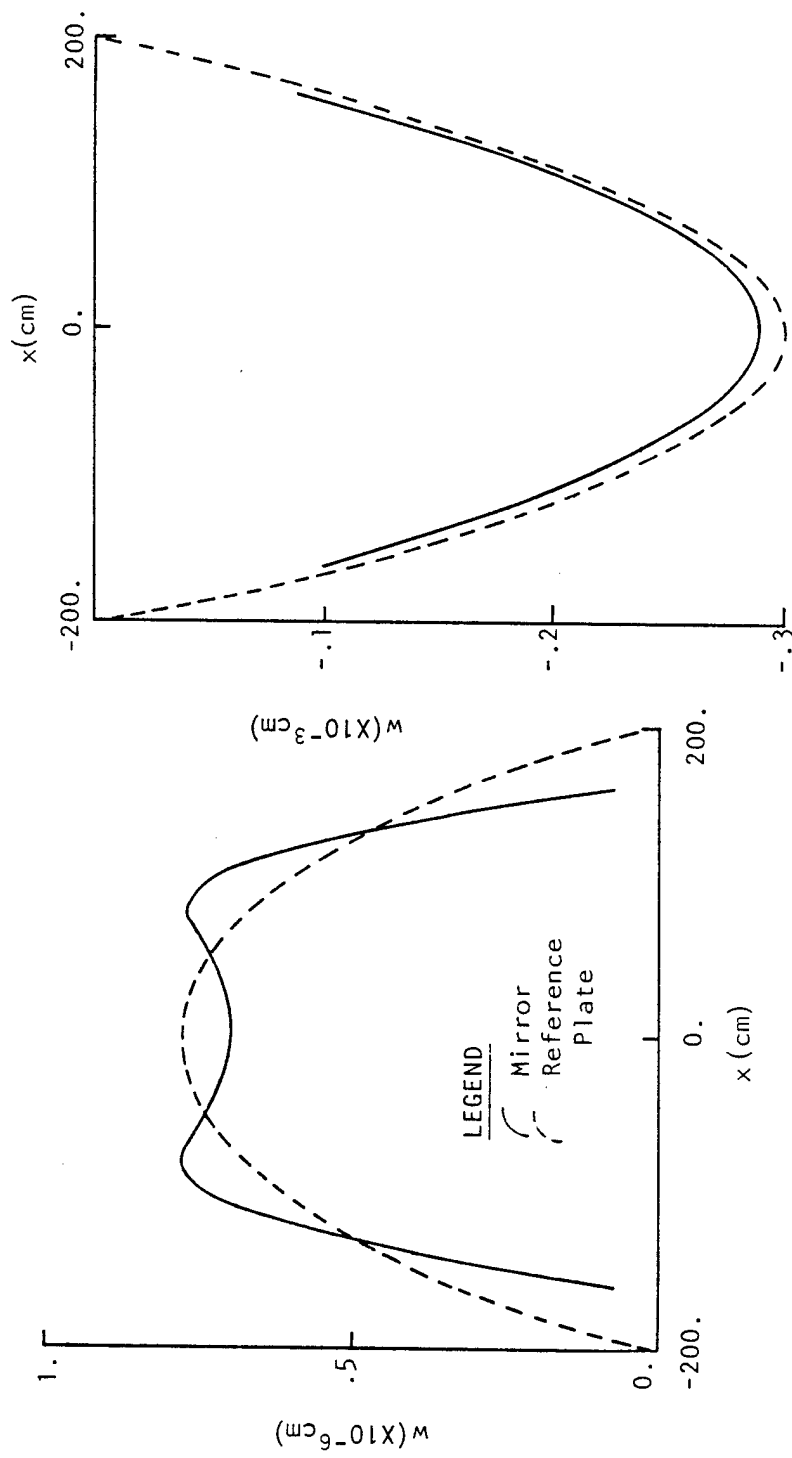
blade annular flexure illustrated in Fig. 5.5, (2) the connection between the middle of the actuator post and the slider is not critical except, of course, for vertical translation so no flexure will be used here and, (3) it is not important whether or not the truss diagonals can resist bending. The last lesson further supports the contention that for the integrated mirror system the predominant load carrying mechanism is membrane action and not bending.

Loads

The last function for the 2-dimensional model was to study the effects of various loads, including an axial thermal gradient, gravity loads and loads to enforce a prescribed displacement of the mirror surface. These analyses used models with small reference plates and with actuator post flexures.

The 1°C axial thermal gradient was applied to the mirror only. The temperature of the support structure remained at ambient, and the highest temperature was on the front face of the mirror. The deflections of the mirror and reference plate are shown in Fig. 3.8(a). The peak-peak deflection of the mirror is $.011\lambda$. This is 5.8% of the deflection that the same mirror would experience if it were not part of an integrated mirror system, but were instead mounted as a simply supported beam. The stresses and deflections from this model served as estimates for the 3-dimensional model. The maximum reference plate bending stress is only 38.% of the maximum reference plate axial stress, even though the thermal gradient is input to the mirror as bending moments and not membrane forces.

Gravity loads were introduced both perpendicular to and parallel to the reference plate. Again calculated stresses and displacements served as estimates for 3-dimensional analyses. Deflection curves for the case where the



(a) Axial Thermal Gradient Across Mirror. (b) Gravity Load Parallel to Reference Plate.

Fig. 3.8. Mirror and Reference Plate Deflections for Thermal Gradient and Gravity Loads.

gravity load is applied parallel to the reference plate are presented in Fig. 3.8(b). The peak-peak mirror deflection is 4.6λ . More important is the fact that the shape is very close to a parabola, so that the deviation from the best fit sphere is very small. This observation led to the consideration of mounting the integrated actuator system with flexures attached to the reference plate, as shown in Fig. 5.3, rather than with a 3 point kinematic support.

The methods of loading for normal position control in Case 5 of Fig. 3.3 and for in-plane slope control in Case 9 of Fig. 3.6 cannot be used directly to simultaneously prescribe translation and rotation of the mirror surface. In Case 5 the slider is disconnected from the post of the active actuator so that forces can be applied to the members, and in Case 9 the actuator post and reference plate are disconnected at the active control. The stiffness matrices for the two cases are not the same. By leaving the members connected and applying thermal loads instead of concentrated forces, the stiffness matrices are identical. For normal position control the thermal load is applied to the slider and the actuator force is the slider's axial load. For in-plane slope control a thermal load is applied to heat the element of the reference plate on one side of the actuator post while simultaneously cooling the element on the opposite side of the post, and the actuator force is the difference of the axial forces in the two reference plate elements. These two pairs of equivalent methods of actuation yield identical results except for the displacements of the point of application of the concentrated forces.

Using the thermally loaded model it is possible to solve for the influence coefficient matrix $[F]$, where in the matrix equation

$$\{x\} = [F]\{f\}$$

x_i is the i^{th} displacement of the mirror surface,
either a translation or a rotation

f_j is the j^{th} temperature, either of a slider or of
a pair of reference plate elements

and F_{ij} is the i^{th} displacement due to a unit j^{th} temperature.

To solve for the thermal loads to enforce a prescribed displacement, simply evaluate

$$\{f\} = [F]^{-1}\{x\}.$$

This technique was tested on the 2-dimensional model and later applied to the 3-dimensional model.

Shear Modulus of Sandwich Core

The sandwich core of a lightweighted mirror is made of a series of webs joined in a repeating pattern. A mirror model with quadrilateral finite elements for the web structure would have too many degrees of freedom to incorporate into a model of the entire integrated active mirror system. For the flat plate models shown in Fig. 3.11 and 3.13, if a cell is 4 cm across, each finite element would contain five cells in the radial direction. This is a sufficient number to assume that the core acts as a continuum and to distribute the stiffness of the webbed cells within solid bricks, each characterized by an equivalent shear modulus, G_e , and an equivalent mass density, ρ_e . The purpose of this section is to evaluate these properties.

The technique used was presented by Soosaar, Grin and Ayer (1975), and presented here to correct errors in that report (shear modulus would be off by a factor of two if those results are used directly) and to develop relations among shear strains. These relations are based on the assumptions that the core carries no normal stress, so that transverse shear strains are constant across the core's depth, that transverse shear strains are not a function of x and y within each brick, and the in-plane shear strains are negligible.

Fig. 3.9 shows a side view of a sandwich plate illustrating core depth, h , and web thickness, t , and presents top views of square, triangular and hexagonal webbed cores. The smallest repeating unit in each case is enclosed within a dashed square. The strain energy within the repeating unit for the lightweight core is:

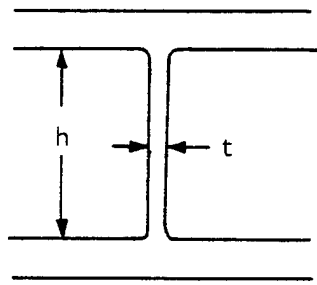
$$U = \sum_{i=1}^n \int_{V_i} \gamma_i^2 G dv_i$$

where: $n = 4$ for square core
 $n = 3$ for triangular and hexagonal cores

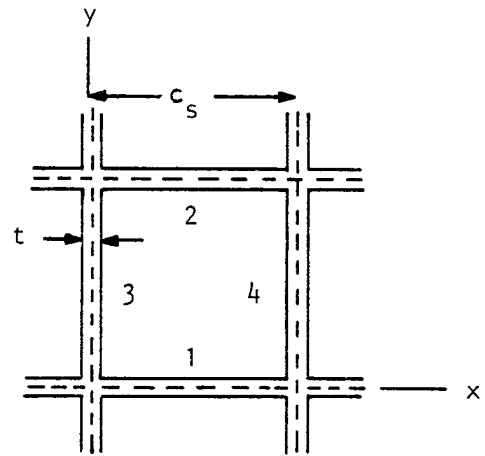
The strain energy for the equivalent solid core is:

$$U_e = \frac{1}{2} \int_V (\gamma_{xz}^2 + \gamma_{yz}^2) G_e dv$$

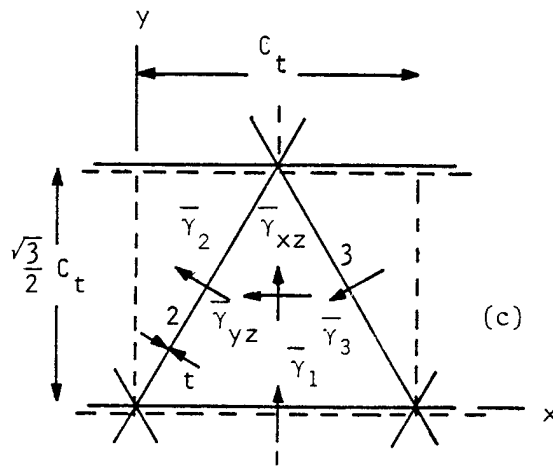
The equivalent shear modulus is found by equating the strain energy from the webbed core to that of the equivalent solid core. Before doing this, the shear strains within the webs, γ_i , must be put in terms of the shear



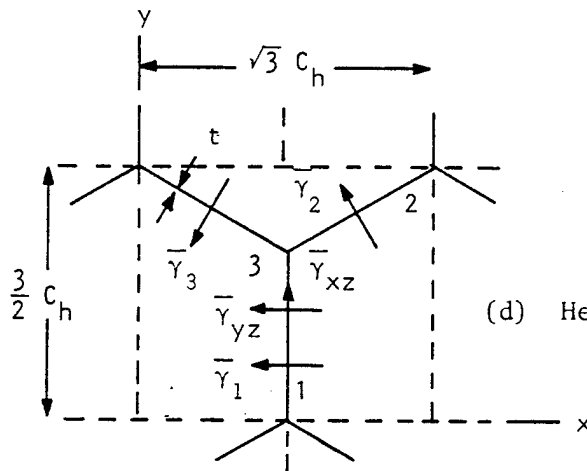
(a) Side view of sandwich plate.



(b) Top view of square core.



(c) Triangular core.



(d) Hexagonal core.

Fig. 3.9. Modeling Webbed Core as Equivalent Solid Core.

strains of the repeating unit, γ_{xz} and γ_{yz} . This is trivial only for the square core. For the triangular and hexagonal cores, shear strains are represented as vectors in Fig. 3.9. This is allowable since infinitesimal rotations are vector quantities. The total shear strain vector for the repeating unit is:

$$\bar{\gamma} = -\gamma_{yz}\hat{i} + \gamma_{xz}\hat{j}.$$

The web shear strain γ_i is the magnitude of the component of $\bar{\gamma}$ in the direction of $\bar{\gamma}_i$, i.e.,

$$\gamma_i = \bar{\gamma} \cdot \frac{\bar{\gamma}_i}{|\bar{\gamma}_i|}$$

From equating the masses of the webs within the repeating unit to that of an equivalent solid core, a relation between the mass densities ρ and ρ_e is found.

Table 3.2 lists results for the three cores. Also included in the table is the quantity, p , called pitch. If p is substituted into the expressions for G_e and ρ_e , for all three cores these equations take the forms:

$$G_e = \frac{t}{p} G$$

$$\gamma_e = \frac{2t}{p} \gamma.$$

Table 3.2 Mechanical properties of three sandwich cores

<u>Property</u>	<u>Square</u>	<u>Triangular</u>	<u>Hexagonal</u>
γ_1	γ_{xz}	γ_{xz}	γ_{yz}
γ_2	γ_{xz}	$\cos 30^\circ \gamma_{yz} + \sin 30^\circ \gamma_{xz}$	$\sin 30^\circ \gamma_{yz} + \cos 30^\circ \gamma_{xz}$
γ_3	γ_{yz}	$\cos 30^\circ \gamma_{yz} - \sin 30^\circ \gamma_{xz}$	$\sin 30^\circ \gamma_{yz} - \cos 30^\circ \gamma_{xz}$
γ_4	γ_{yz}		
U	$\frac{1}{2} G t C_s h (\gamma_{xz}^2 + \gamma_{yz}^2)$	$\frac{3}{4} G t C_t h (\gamma_{xz}^2 + \gamma_{yz}^2)$	$\frac{3}{4} G t C_h h (\gamma_{xz}^2 + \gamma_{yz}^2)$
U_e	$\frac{1}{2} G_e C_s^2 h (\gamma_{xz}^2 + \gamma_{yz}^2)$	$\frac{\sqrt{3}}{4} G_e C_t^2 h (\gamma_{xz}^2 + \gamma_{yz}^2)$	$\frac{3\sqrt{3}}{4} G_e C_h^2 h (\gamma_{xz}^2 + \gamma_{yz}^2)$
G_e	$\frac{t}{C_s} G$	$\frac{\sqrt{3}t}{C_t} G$	$\frac{t}{\sqrt{3}C_h} G$
ρ_e	$\frac{2t}{C_s} \rho$	$\frac{2\sqrt{3}t}{C_t} \rho$	$\frac{2t}{\sqrt{3}C_h} \rho$
ρ	C_s	$\frac{C_t}{\sqrt{3}}$	$\sqrt{3}C_h$

Flat Plates

Richard and Malvick (1973) have shown that the structural action of a lightweight mirror can be accurately represented by membrane elements. In their work membrane elements were used for the webbed core and the face-plates. The improvement in the overall mirror deflection from replacing these membrane elements by bending elements is negligible. They also found that results are not affected by cell size, as long as the size is kept sufficiently small. This indicates that a sandwich core modeled by homogeneous solid elements would work equally well for predicting over-all deflections.

SAP IV Flat Plate Analysis

Using the SAP IV program, a segment of sandwich material was modeled using membrane elements as top and bottom faces and a solid element for the core, as shown in Fig. 3.10.

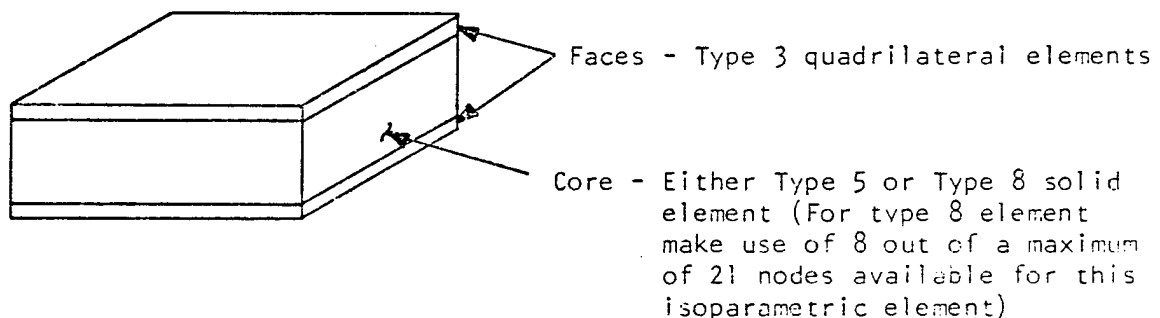


Fig. 3.10. Sandwich model.

Incompatible displacement modes improve the bending properties of Type 3 quadrilateral elements for bending in the plane of the element, i.e. for bending moment vectors with directions perpendicular to the elements. Since the loading of the sandwich beam and mirror models will not cause this

in-plane bending, incompatible displacement modes are not used for the quadrilaterals. Type 5 solid elements also utilize incompatible displacement modes. Without these modes the element would be overly stiff in bending, since the basic element does not adequately represent the shear strain of bending. Type 8 solid elements do not utilize incompatible displacement modes.

Two finite element models of a homogeneous, annular flat plate were analyzed and compared with theoretical calculations. The finite element models are shown in Fig. 3.11. The only difference between the two models is the type of solid elements, either Type 5 or Type 8. The geometry and material properties of the two models are identical. In order to easily compare results with an analytical solution, (1) the plates are flat, not spherical, as in the actual mirror and (2) the plates are homogeneous, not honeycomb, so material properties for the membrane and solid elements are identical. In the analyses the models were simply supported along the outer edge. Two distinct loads were applied to each model. These loads and the support conditions are shown in Fig. 3.12. Theoretical results were calculated using equations presented by Timoshenko and Woinowsky-Krieger (1959, pp. 59-61). A comparison of results is given in Table 3.3.

Table 3.3. Results of SAP IV Flat Plate Analysis

Analysis	Load	Max Deflection $w(r=b)$	% Error
SAP IV - Type 5 elements	q	1.21×10^{-1}	4
SAP IV - Type 5 elements	Q_0	1.26×10^{-6}	3
SAP IV - Type 8 elements	q	2.05×10^{-2}	84
SAP IV - Type 8 elements	Q_0	2.26×10^{-7}	83
Plate Theory (Timoshenko)	q	1.26×10^{-1}	--
Plate Theory (Timoshenko)	Q_0	1.30×10^{-6}	--

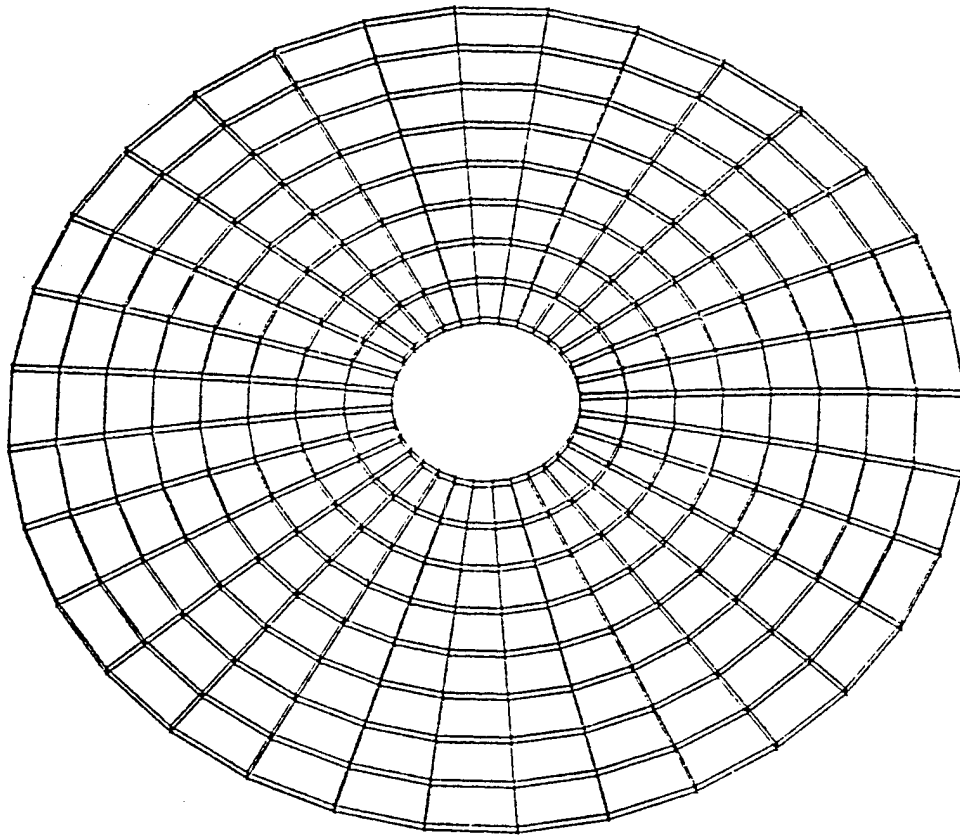


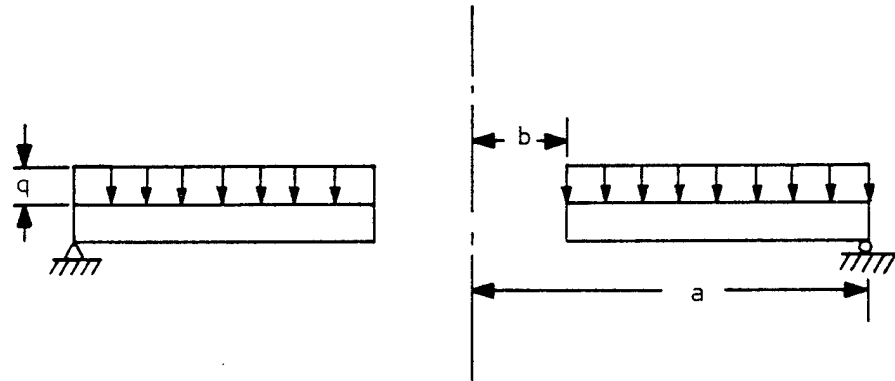
Fig. 3.11. SAP IV Flat Plate Model.

Model Specifications:

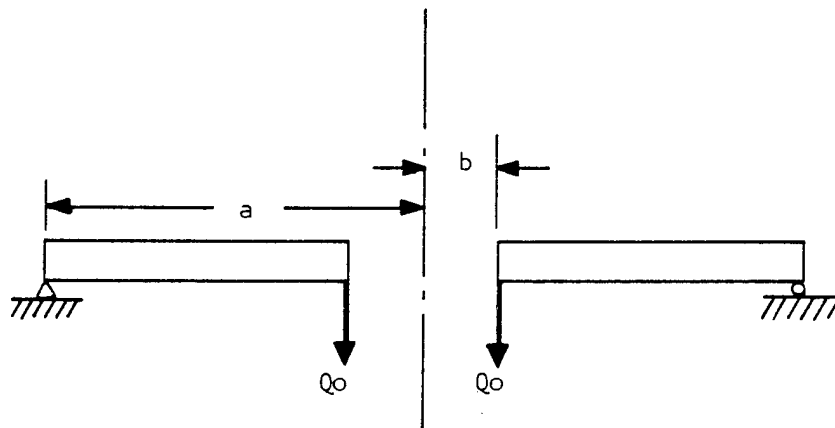
576 Nodes

512 Type 3 membrane elements

256 Type 5 or Type 8 solid elements



Uniform Distributed Load q



Uniform Shear Load Q_o

Fig. 3.12. Supports and Loads for Flat Plate Models.

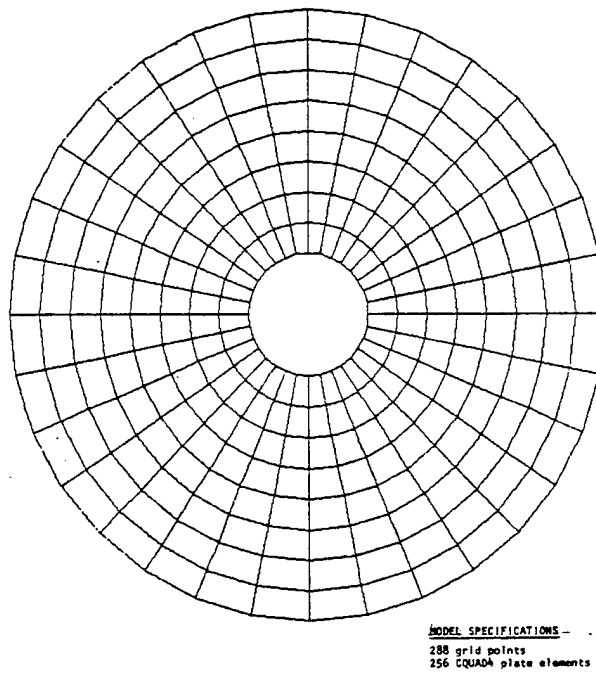
The performance of Type 5 elements is far superior to that of Type 8 elements. Inaccuracies for Type 5 elements due to utilizing incompatible modes for elements that are not rectangular parallelepipeds are trivial as compared to inaccuracies for Type 8 elements which do not use incompatible modes.

The honeycomb, spherical mirror model was generated by making minor modifications to the model of the homogeneous, annular flat plate with Type 5 solid elements. These modifications consisted of modifying the node coordinates perpendicular to the plate to achieve a spherical shape, and reducing the moduli of elasticity and rigidity of the core to 5% of that of solid material. Results from an analysis of the spherical mirror model are shown in Fig. 4.10.

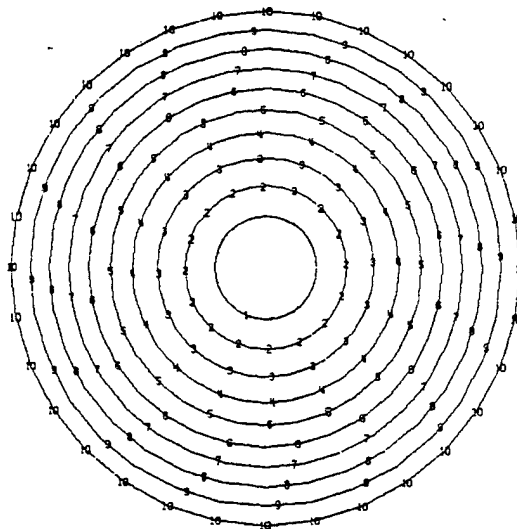
MSC/NASTRAN Flat Plate Analysis

The MSC/NASTRAN finite element computer program is superior to the SAP program for our particular application, since NASTRAN has nonhomogeneous plate elements that can be used to model a sandwich plate. For a segment of a sandwich plate, one NASTRAN plate element models the two faces and the core, whereas three elements were needed with SAP.

A NASTRAN model of the same homogeneous, annular flat plate used in the previously described SAP IV analysis was generated with CQUAD4 plate elements. This model is shown in Fig. 3.13(a). The model was analyzed under gravity loading and the results were compared to plate theory. For the NASTRAN model the deflection was 1.24×10^{-1} , giving an error of 1.6 %. The SAP IV analysis has a 4% error. A contour plot of deflection normal to the plate is shown in Fig. 3.13(b).



(a) NASTRAN model.



(b) Contour Plot

Fig. 3.13. NASTRAN Flat Plate Model.

Later the material properties of the annular flat plate were changed to coincide with those of two mirrors used in the 40-actuator system. For the lightweight plate, Plantema's (1966) theory, accounting for both bending and shear deformation, was used to calculate theoretical results. For the solid plate, deflection to three significant figures was unaffected by the inclusion of shear deformation. Results are presented in Table 3.4.

Table 3.4. Results of NASTRAN flat plate analysis.

Flat plate	Load	Max deflection from NASTRAN	Max deflection from plate theory	% Error
Solid	q	1.73	1.76	1.7
Solid	Q_0	1.12	1.14	1.8
Lightweight	q	.479	.488	1.8
Lightweight	Q_0	1.93	1.96	1.5

In addition to mesh coarseness, three factors that affect the accuracy of the model are the element's aspect ratio, skew and warp. The largest aspect ratio for the CQUAD4 elements is 2. It occurs for the elements on the outer edge of the annular plate. MacNeal (1978) has reported test results claiming that single element torsional deflections are correct to within 1.5% for aspect ratios up to 20 and that bending - torsion displacements are accurate to 1.% for aspect ratios up to 11. The skew angle for all elements in the mode is about 11%. Schaeffer (1979) claims that good results are obtained for skew angles up to 45° for the CQUAD4 element. Element warping is negligible.

MCS/NASTRAN has another feature, cyclic symmetry analysis, that is not available with SAP IV and that may be applied in future work. In cyclic symmetry, or rotational symmetry, one segment of a model is supplied by the user and the program transforms the properties of that segment to assimilate a model in which the fundamental segment is repeated at equal intervals about an axis of symmetry. Loads in the analysis can be applied over the entire model and do not have to be symmetrically located with respect to the axis of symmetry. Advantages to using this technique include only having to model one segment of a cyclic symmetric structure and reduction in computer costs in most situations. A disadvantage is that NASTRAN provides only a contour plot of the fundamental segment. In addition, both the structure and its boundary conditions must be symmetric in order to use cyclic symmetry, so at best, a structure mounted on a three-point support can be reduced to one third of the model.

Testing on the flat plate models has shown cyclic symmetry to not be economically feasible when total program costs are considered. However, the cyclic symmetry capability in NASTRAN is being upgraded, and as models become more complex it may be desirable, if not essential, to make use of this capability.

Contour Plot Interpretation

All of the contour plots in this report are for the z-displacement of the surface of the mirror. Each plot has ten displacement contours. To calculate the value of displacement for a particular contour line, refer to the maximum and minimum values on each figure. The maximum value occurs at contour line 10 and the minimum at contour 1. The contour intervals are constant and are one-ninth of the total difference between the extreme values. Displacement units are centimeters.

The shape of the deflection surface is the critical information gleaned from the contour plots. For linear analysis the displacement coordinates for the surface are proportional to the magnitude of the load.

CHAPTER 4

40-ACTUATOR MIRROR

Analysis of the mirror aids both the design of the mirror and its support structure. Even though the support structure is not included in the finite element model of the mirror, a "perfectly rigid" support is simulated by constraining to zero all uncontrolled degrees of freedom of actuator attachment grid points on the mirror. The "perfectly rigid" support is used to study localization of mirror deformation due to normal position control and slope controls and to study deformation due to gravity. Results of analyzing individual controls, either normal position or slope of a single actuator, then serve as a guide in designing the support structure, which is carried out in the next chapter. The gravity analysis is important, since most of the inter-actuator sag due to gravity release cannot be removed by active actuators, either by using normal position control alone or in union with slope controls.

The finite element mirror model is also used to investigate scalloping around the outer and inner edges of the mirror due to defocus, and to enforce an astigmatic aberration. Both defocus and astigmatism are investigated, because the former results in a nondevelopable shape, while the latter results in a developable shape. A developable shape has no stretching of the middle surface, and is much easier to achieve with active controls than a nondevelopable shape.

Intra-cell deflections of a lightweight mirror due to both gravity and lap loads are calculated using plate theory, since the finite element model does not include that level of detail. These deflections influence the choice of physical dimensions of the individual structural elements of a lightweight mirror, e.g., cell wall thickness, cell spacing, etc.

The FRINGE computer program is used to reduce the mirror surface deflection from a finite element analysis into a "bottom line" rms value and span of the residual wavefront.

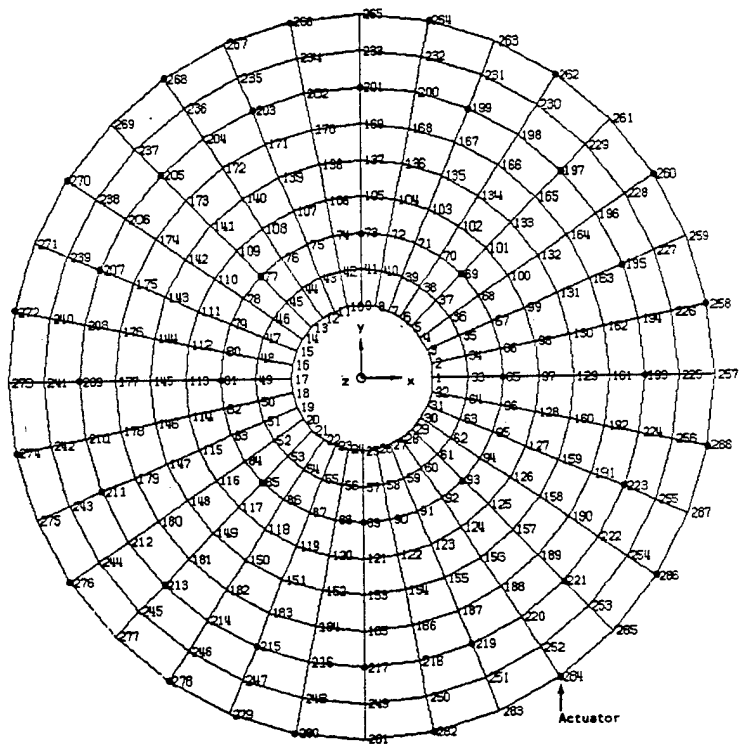
Finite Element Models

The mirror for the 40-actuator system has the following physical dimensions:

Diameter (Aperture)	4 m
f/no.	1.5
Radius of Curvature	12 m
Central Hole Diameter	80 cm or 20% of aperture

The geometry of the mirror models differs from the flat, annular plate models only in the z coordinates of the nodes. The NASTRAN model is shown in Fig. 4.1. The locations on the mirror where actuators would attach are designated on the top view. The numbers of elements and grid points, or nodes, are given on the flat plate models shown in Fig. 3.11 (SAP IV model) and 3.13 (NASTRAN model).

The mirror is a doubly curved surface, and bending and in-plane forces will not result in independent deformations. It is modeled by flat plate elements for which bending and membrane stiffness



(a) Top View



(b) Side View

Fig. 4.1. Mirror Model.

are uncoupled. Zienkiewicz (1977, p. 344) demonstrates that for a model composed of triangular and quadrilateral flat plate elements, behavior converges to that of the actual shell as mesh size decreases.

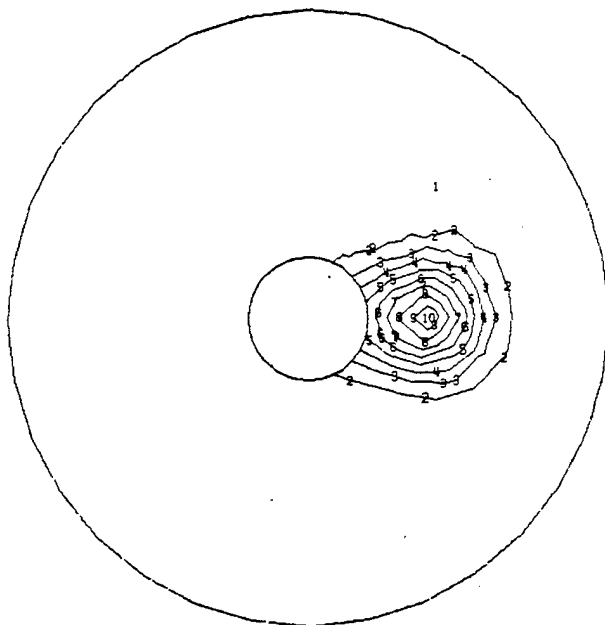
Normal Position and Slope Controls

Actuators are located on three different radii in the 40-actuator system. Each actuator has normal position control and tangential and radial slope control. This makes nine unique controls which must be analyzed. For each control all actuator degrees of freedom are fixed except for the degree of freedom being given a unit displacement. Contour plots of the mirror's z displacement for each of the nine unique controls were generated for each of three mirror designs. Mirror cross section dimensions and material properties are given in Fig. 5.2. Contour plots for the solid mirror and thin lightweight mirror are shown in Figs. 4.2-4.7. Contour plots for the thick lightweight mirror are similar to plots for the thin lightweight mirror except for the radial slope control of the 80-cm actuator, which is more localized for the thick mirror. Contour plots for the thick lightweight mirror were published by Shannon, Richard and Hansen (1980, pp. 25-27) and are not repeated here. It is interesting that the three sets of contour plots are so similar, even though the structures of the three mirrors are so different.

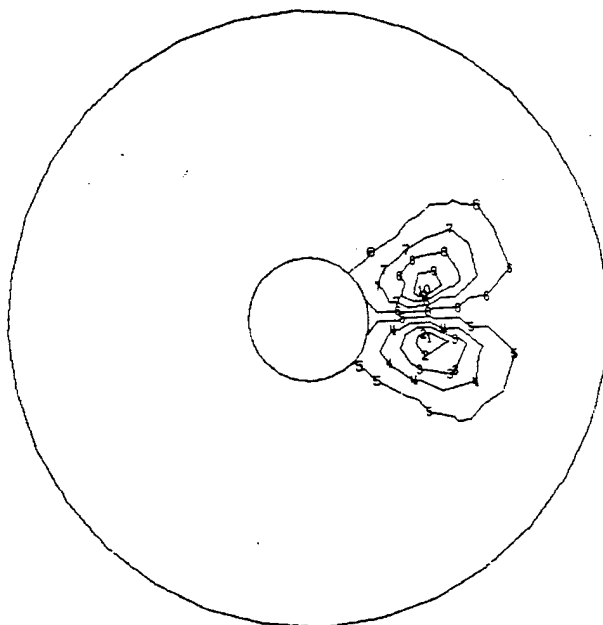
Notice how the deformations are localized to the immediate vicinity of the displaced actuator. If one were to mark the actuator locations on the contour plots, one would see that for all but one plot

Max-Def = 1.00
Min-Def = -3.41×10^{-2}

Max-Def = 6.05
Min-Def = -6.05

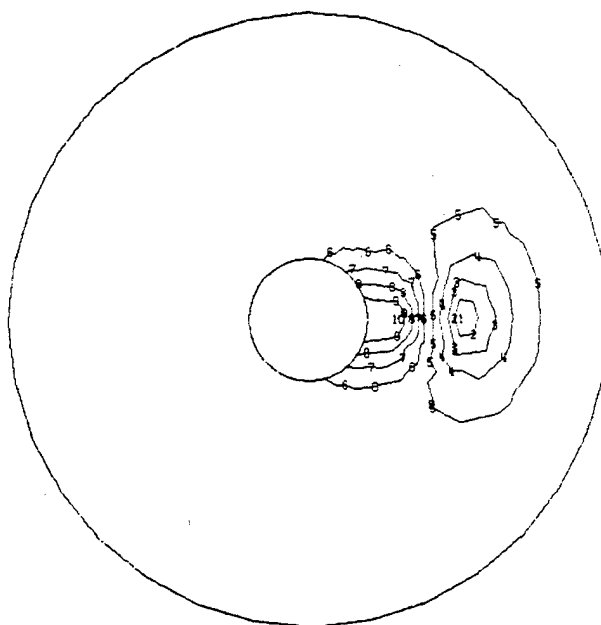


(a) Normal Position Control



(b) Tangential Slope Control

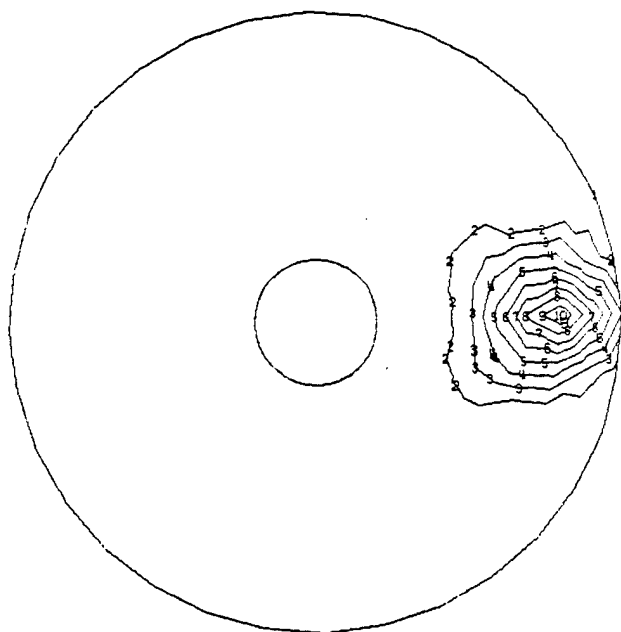
Max-Def = 7.37
Min-Def = -6.68



(c) Radial Slope Control

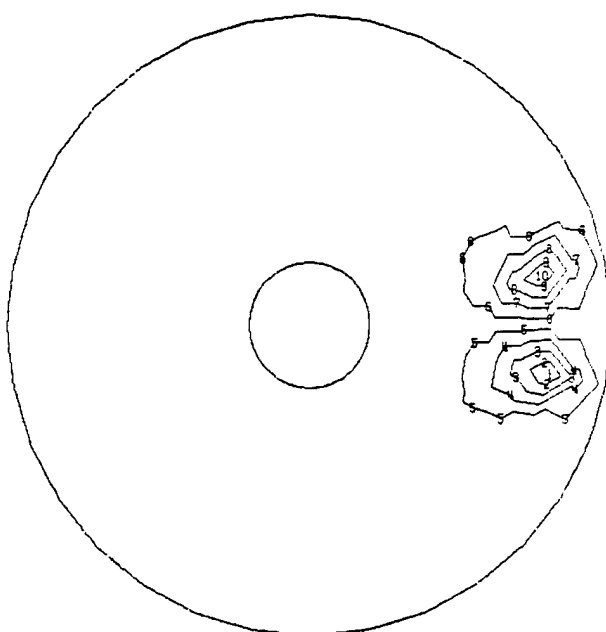
Fig. 4.2. Solid Mirror Model, 80-cm Actuators.

Max-Def = 1.00
Min-Def = -3.58×10^{-2}



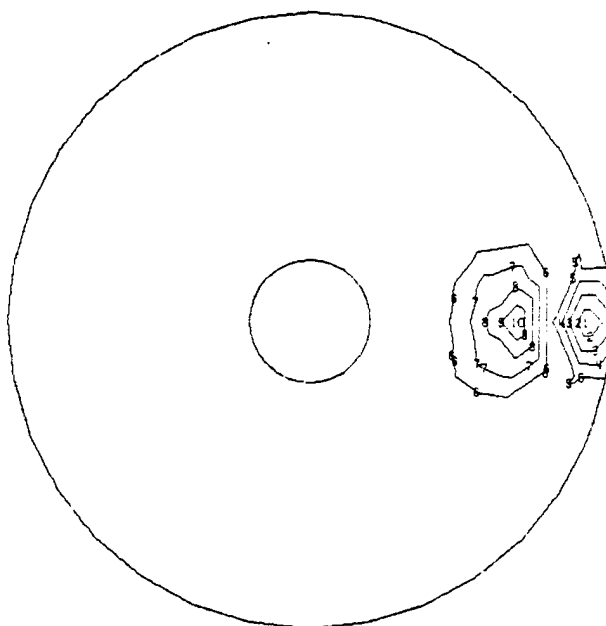
(a) Normal Position Control

Max-Def = 5.71
Min-Def = -5.71



(b) Tangential Slope Control

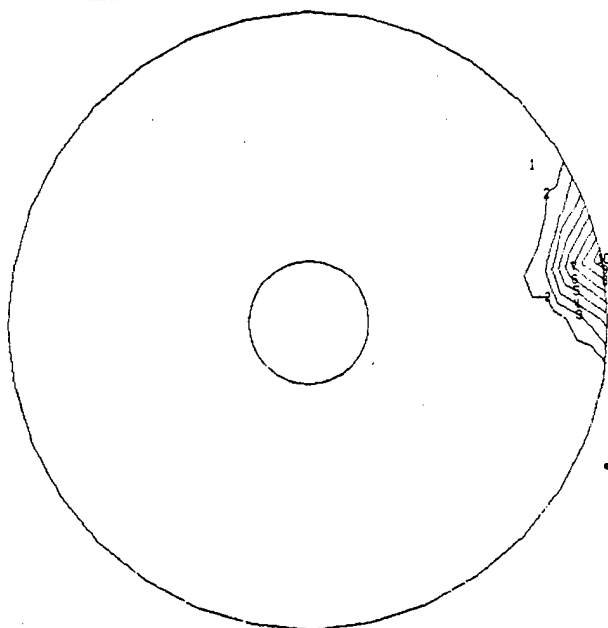
Max-Def = 7.41
Min-Def = -6.83



(c) Radial Slope Control

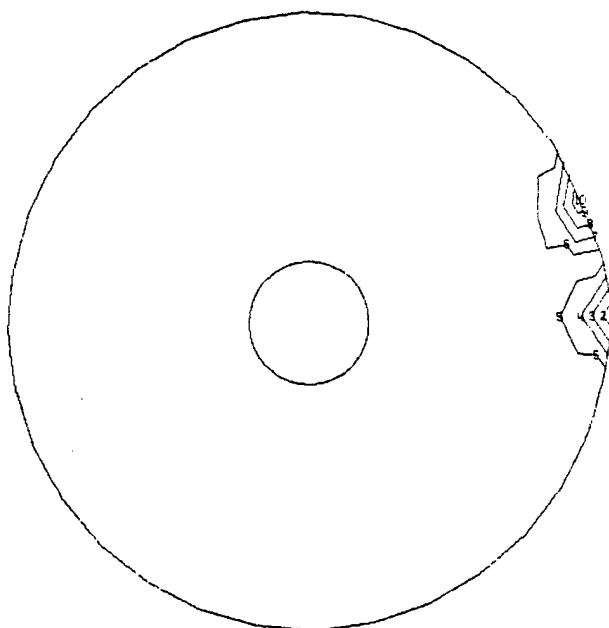
Fig. 4.3. Solid Mirror Model, 160-cm Actuators.

Max-Def = 1.00
Min-Def = -1.50×10^{-2}



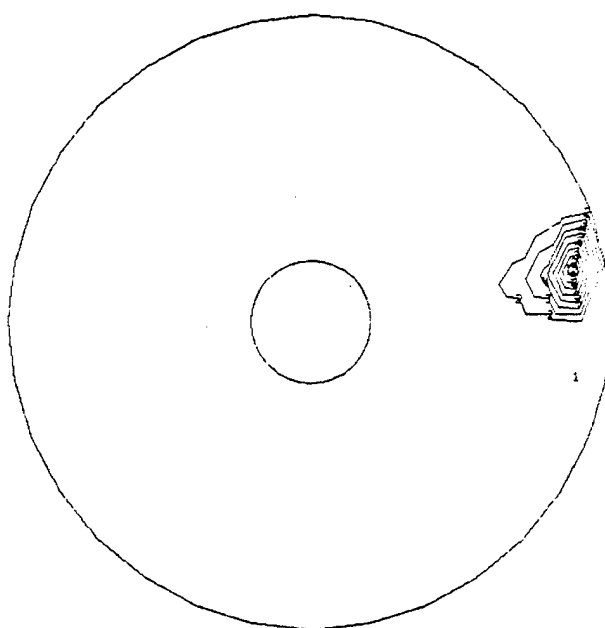
(a) Normal Position Control

Max-Def = 8.15
Min-Def = -8.15



(b) Tangential Slope Control

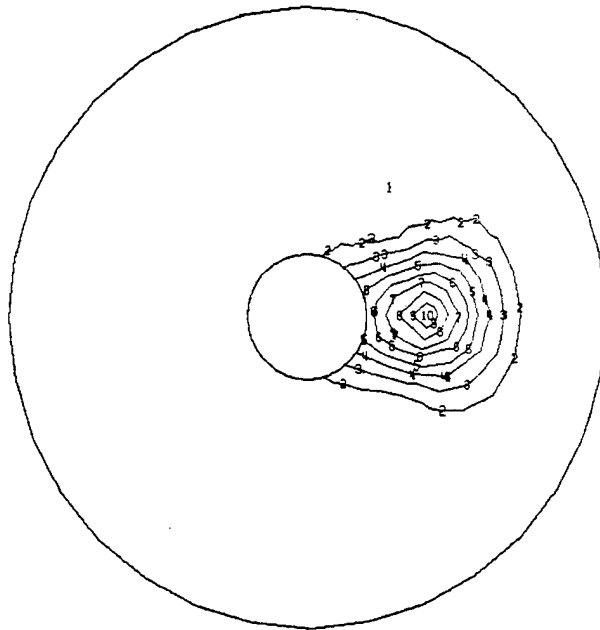
Max-Def = 6.16
Min-Def = -3.90×10^{-1}



(c) Radial Slope Control

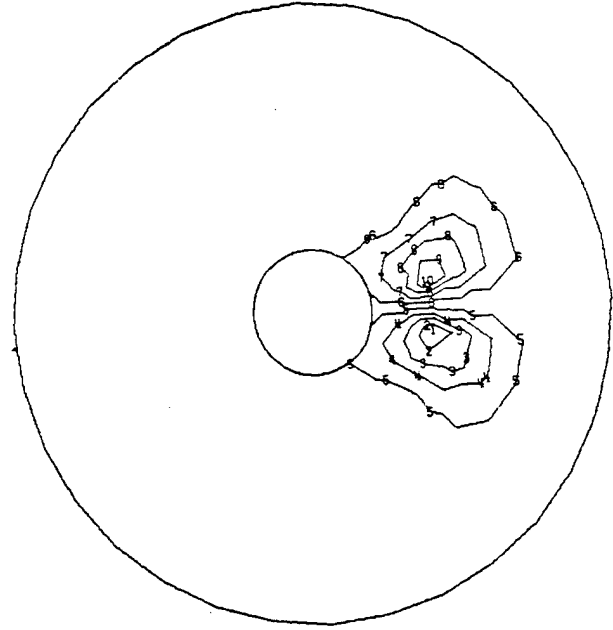
Fig. 4.4. Solid Mirror Model, 200-cm Actuators.

Max-Def = 1.00
Min-Def = -3.26×10^{-2}



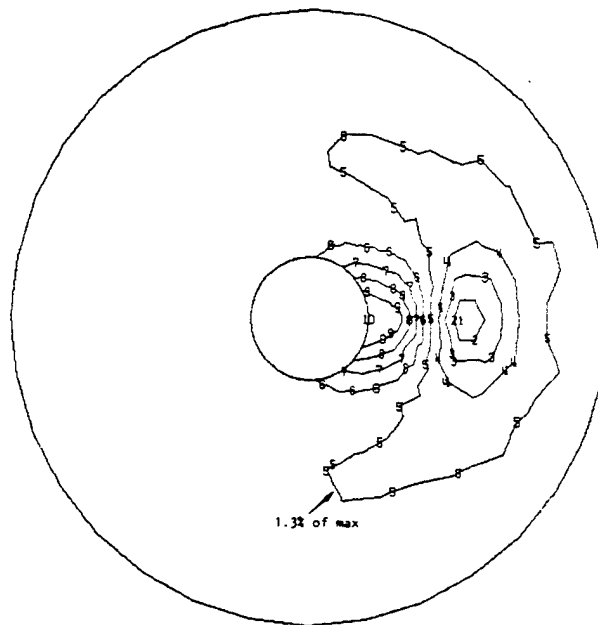
(a) Normal Position Control

Max-Def = 5.32
Min-Def = -5.32



(b) Tangential Slope Control

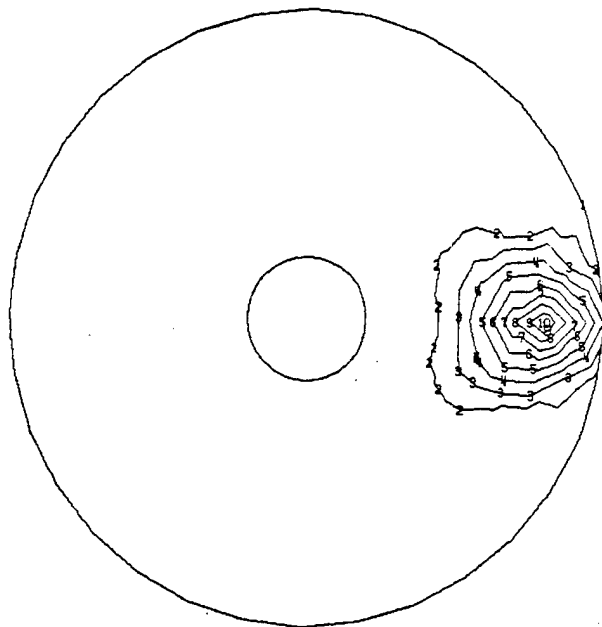
Max-Def = 7.13
Min-Def = -5.87



(c) Radial Slope Control

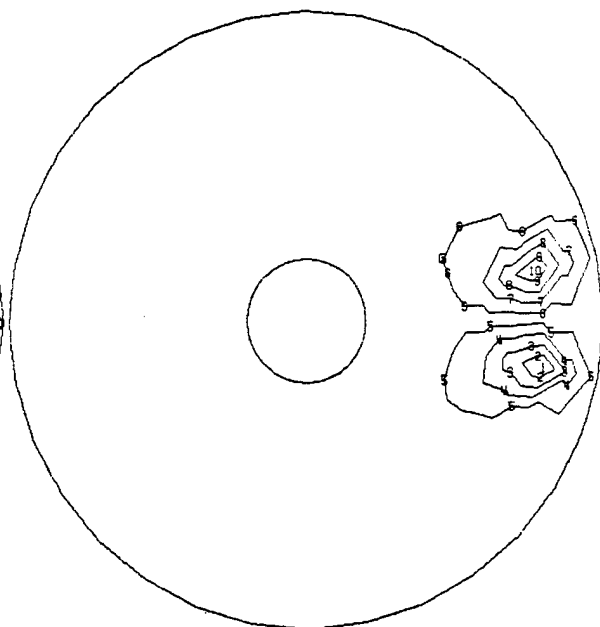
Fig. 4.5. Thin Lightweight Mirror Model, 80-cm Actuators.

Max-Def = 1.00
Min-Def = -4.41×10^{-2}



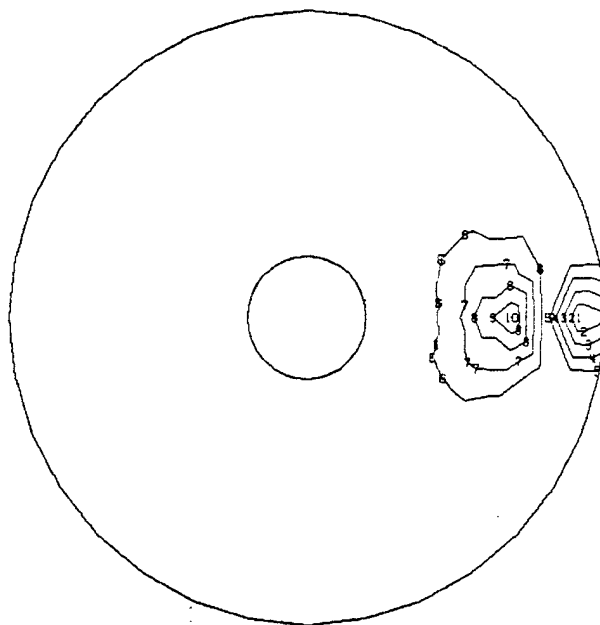
(a) Normal Position Control

Max-Def = 4.69
Min-Def = -4.69



(b) Tangential Slope Control

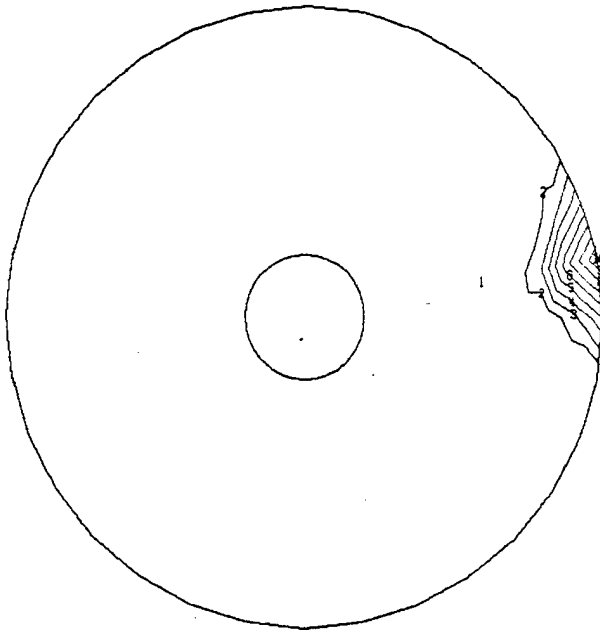
Max-Def = 7.12
Min-Def = -7.08



(c) Radial Slope Control

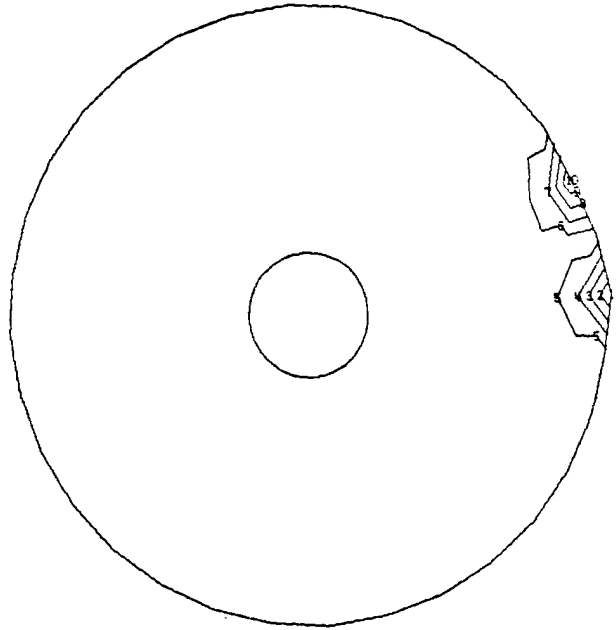
Fig. 4.6. Thin Lightweight Mirror Model, 160-cm Actuators.

Max-Def = 1.00
Min-Def = -9.74×10^{-3}



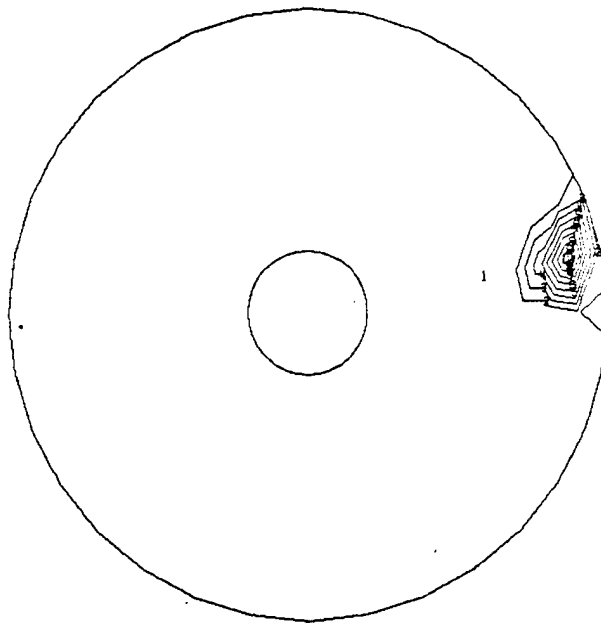
(a) Normal Position Control

Max-Def = 7.09
Min-Def = -7.09



(b) Tangential Slope Control

Max-Def = 6.25
Min-Def = -1.67×10^{-1}



(c) Radial Slope Control

Fig. 4.7. Thin Lightweight Mirror Model, 200-cm Actuators.

all contour lines drawn are contained within the region bounded by the actuators neighboring the displaced actuator. For that plot, which is radial slope control of the 80-cm actuator for the thin lightweight mirror, the deviate contour line represents a magnitude of only 1.3% of the maximum vertical displacement. The localized behavior reduces coupling between actuator controls and significantly reduces the complexity of the required control system. These contour plots will later be compared to those from analyses of 40-actuator systems where support structures have finite stiffness.

Defocus and Astigmatism

Scalloping, which was demonstrated early in our active optics studies, is a result of attempts to make slight changes in a mirror's radius of curvature. When a focus change was made to a 9-actuator system, significant scalloping occurred as seen in Fig. 2.11. A pure radius change of the shell of the mirror would require a state of stress that had for its boundary conditions a uniform radial membrane stress due to a uniform pressure applied to the surface of the shell. Bending and shear stresses along the boundary would not exist. In attempting to produce this change through the bending of the shell by a discrete number of actuator points, deflections that are functions of angular position are obtained. Since the membrane stiffness (the stiffness associated with middle surface stretching) for the mirror is several orders of magnitude larger than the bending stiffness (the stiffness associated with the formation of a developable shape), and

these are coupled in shell action, the membrane stiffness effect dominates, forcing considerable bending to occur in order to accommodate the enforced displacements at the actuator points. Since, for a homogeneous plate, the membrane stiffness varies with the thickness, t , and the bending stiffness with t^3 , it is apparent that by increasing the mirror thickness, the scalloping effect may be reduced. An alternative to a thicker solid mirror is a mirror with sandwich construction and a lightweight core.

Scalloping ensues when the mirror is defocused. The deflection surface is an elliptic paraboloid. The equation for the paraboloid used for the z deflection, w , and a cross-sectional view of the resulting deflection pattern are shown in Fig. 4.8.

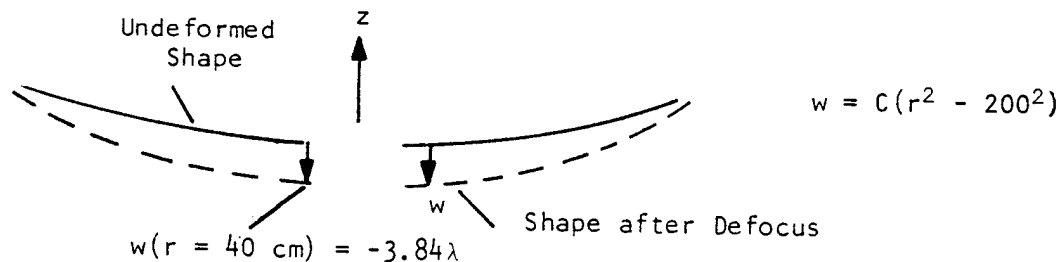
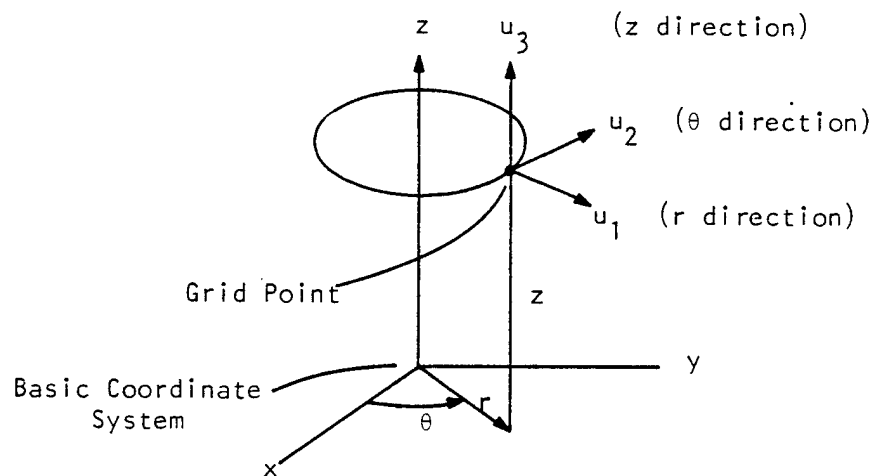


Fig. 4.8. Cross Section of Ideal Defocus.

Of course, since the analysis is linear, any convenient magnitude of displacement could have been chosen. The value of C was chosen so that the deflection would be in units of λ , where both here and throughout this report $\lambda = 6328 \text{ \AA}$. Vertical displacements and slopes were computed for each actuator location. Two separate analyses were executed, and they can best be illustrated with the aid of degrees of freedom defined

for the cylindrical coordinate system shown in Fig. 4.9. For actuator normal position control at each actuator, degree of freedom T3 was enforced, while the other five freedoms were left free. For actuator normal position and slope controls at each actuator, degrees of freedom T3, R1 and R2 were enforced, while the other three degrees of freedom were left free.

Results are shown with contour plots, Figs. 4.10-4.12 and in deflections of radial cross sections of the mirror, Figs. 4.13-4.15. Deviation from the ideal surface as a function of angle can best be portrayed with contour plots. Contour plots should consist of a series of concentric circles spaced closer together as radius increases. The relative amounts of circle flattening show that the thick lightweight mirror can be defocused more accurately than the solid mirror or the thin lightweight mirror. The deviation from the ideal surface as a function of radius is best illustrated by radial cross section deflections. The thick lightweight mirror does quite well at both the inner and outer edge. The other mirrors do well only at the outer edge, due to deployment of two outer rings of actuators. At the unsupported inner edge, several scallop and edge wrap exist, especially for the solid mirror. Severe outer edge scallop exhibited by the 9-actuator system has been eliminated. Results for a similar SAP IV analysis are included on Fig. 4.10 for the thick lightweight mirror. For the SAP analysis the mirror was modeled with separate elements for the two face sheets and the core, as described for the SAP flat plate model. The correlation between SAP and NASTRAN results is



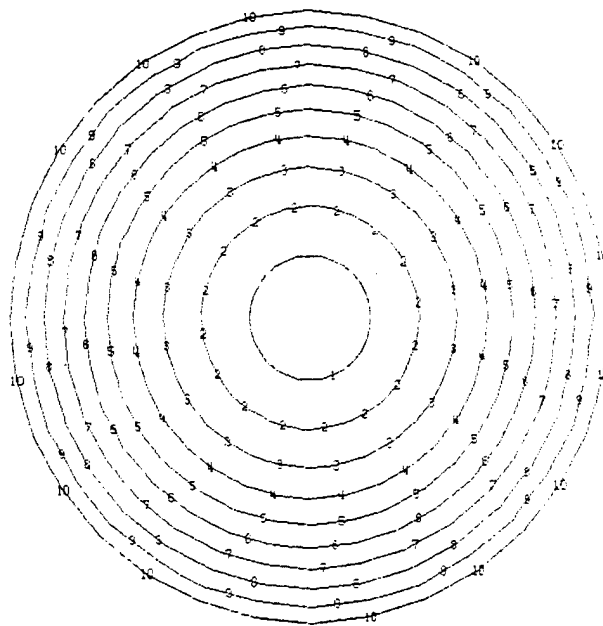
Degrees of Freedom

T1, T2, T3 - translations in 1, 2 and 3 directions

R1, R2, R3 - rotations about 1, 2 and 3 axes

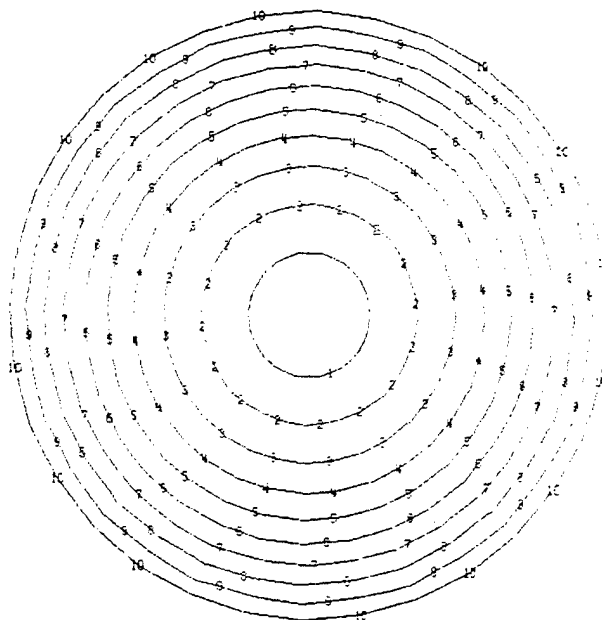
Fig. 4.9. Cylindrical Coordinate System.

Max-Def = 0.
Min-Def = -2.47×10^{-4}



(a) Normal Position Control

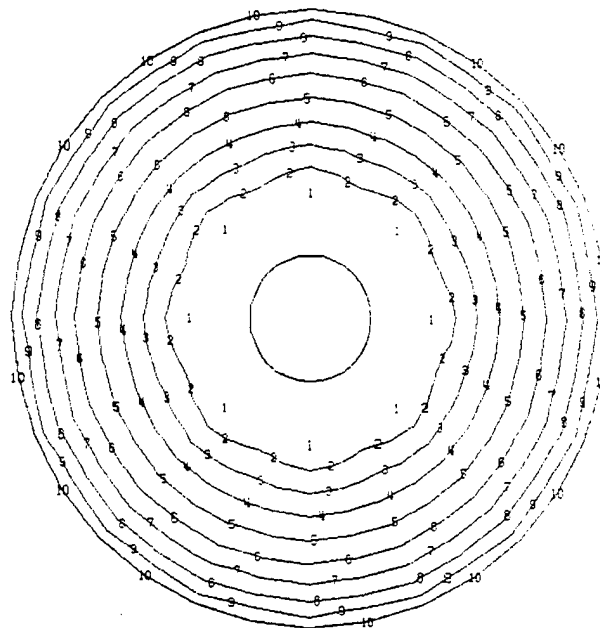
Max-Def = 0.
Min-Def = -2.46×10^{-4}



(b) Normal Position and Slope Controls

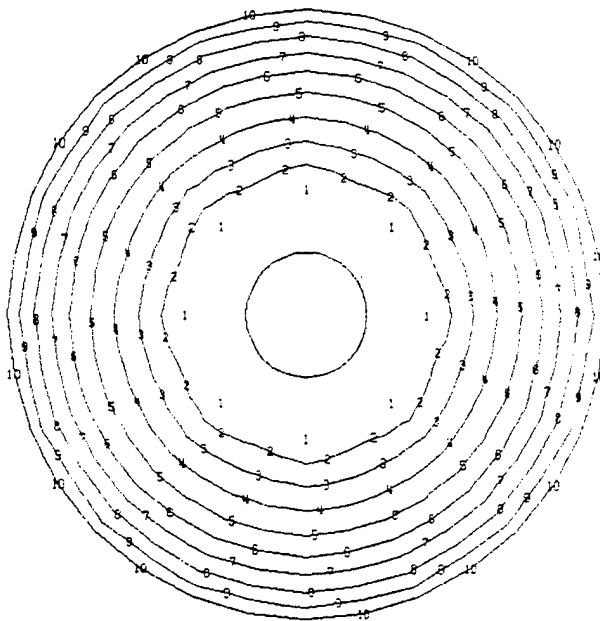
Fig. 4.10. Thick, Lightweight Mirror Model, Defocus.

Max-Def = 0.
Min-Def = -2.13×10^{-4}



(a) Normal Position Control

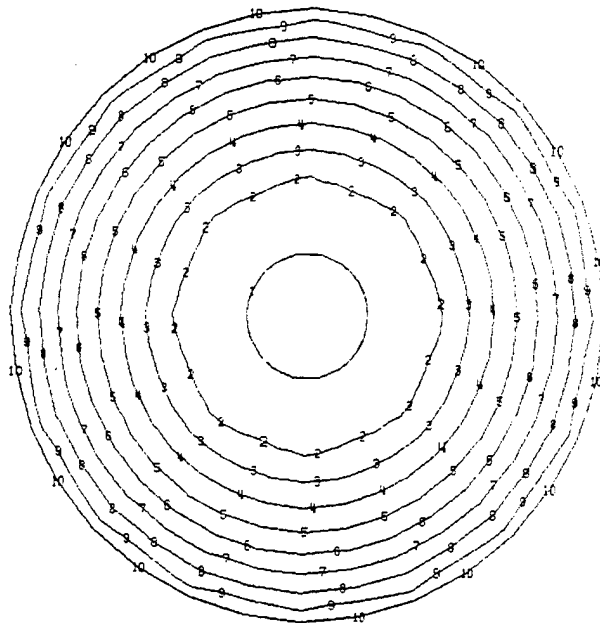
Max-Def = 0.
Min-Def = -2.13×10^{-4}



(b) Normal Position and Slope Controls

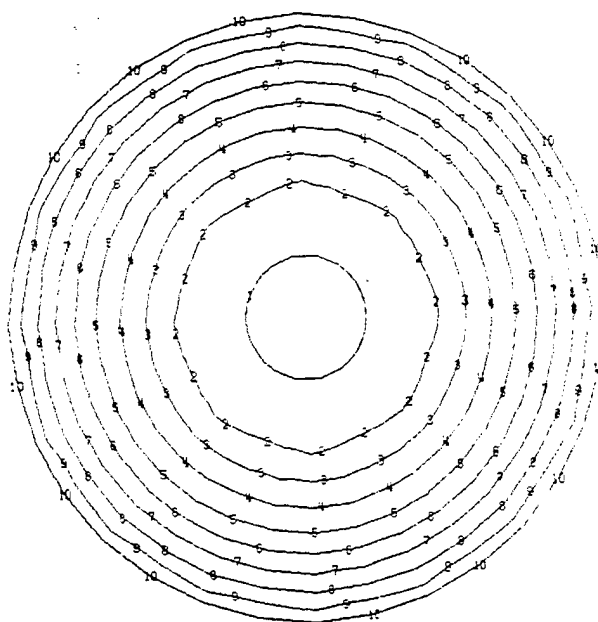
Fig. 4.11. Solid Mirror Model, Defocus.

Max-Def = 0.
Min-Def = -2.25×10^{-4}



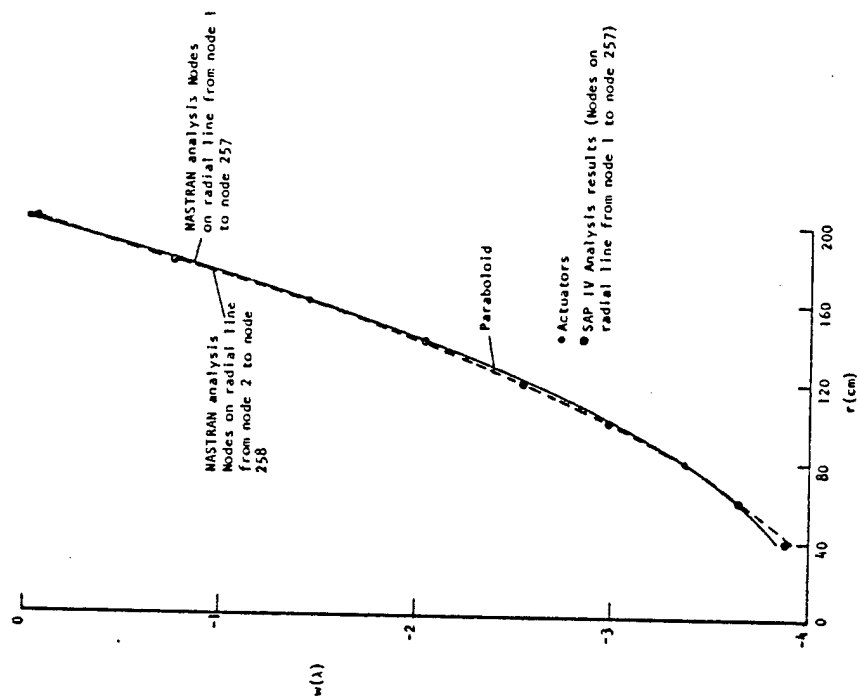
(a) Normal Position Control

Max-Def = 0.
Min-Def = -2.27×10^{-4}

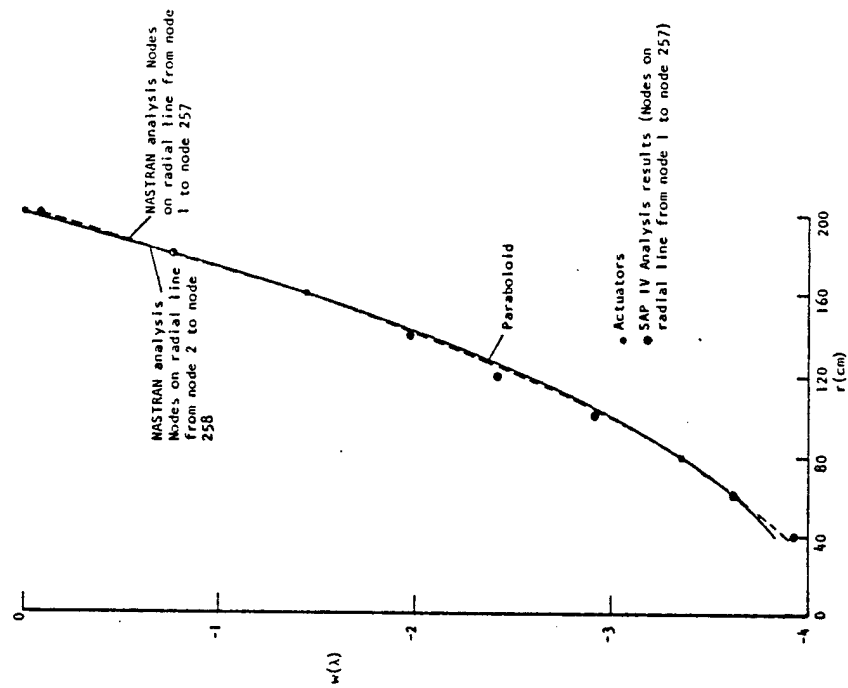


(b) Normal Position and Slope Controls

Fig. 4.12. Thin Lightweight Mirror Model, Defocus.

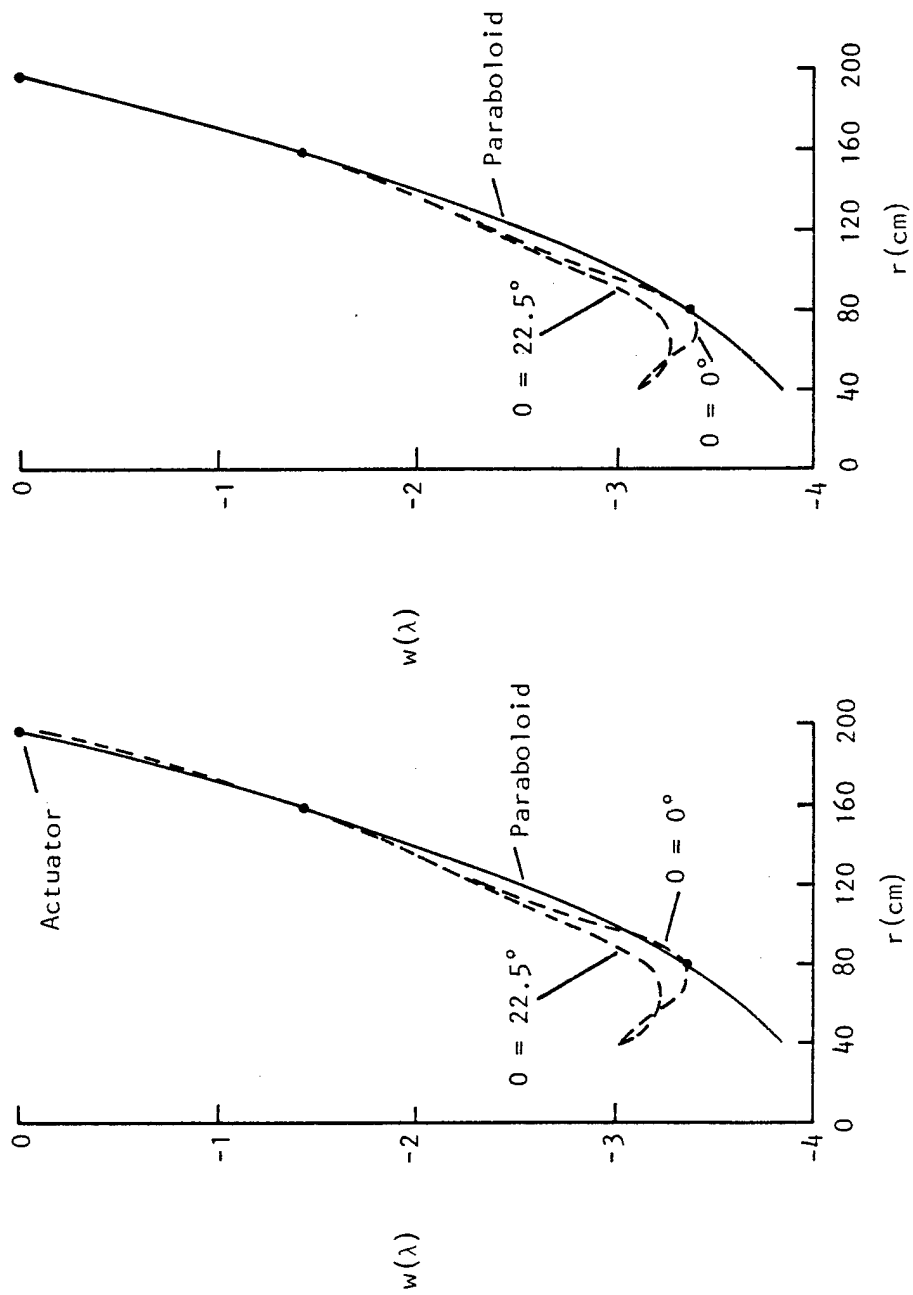


(a) Normal Position Control



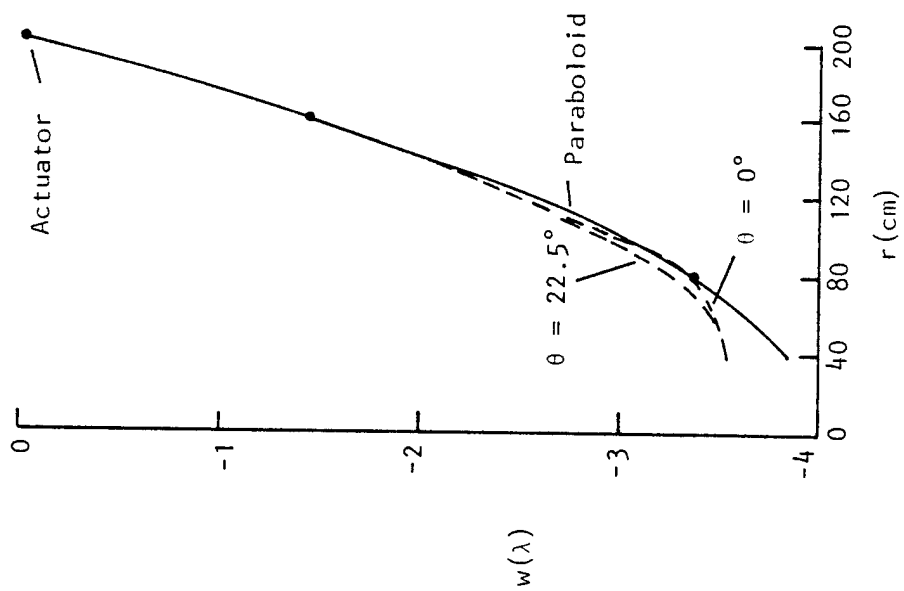
(b) Normal Position and Slope Controls

Fig. 4.13. Thick Lightweight Mirror Model. Cross Sections for Defocus.

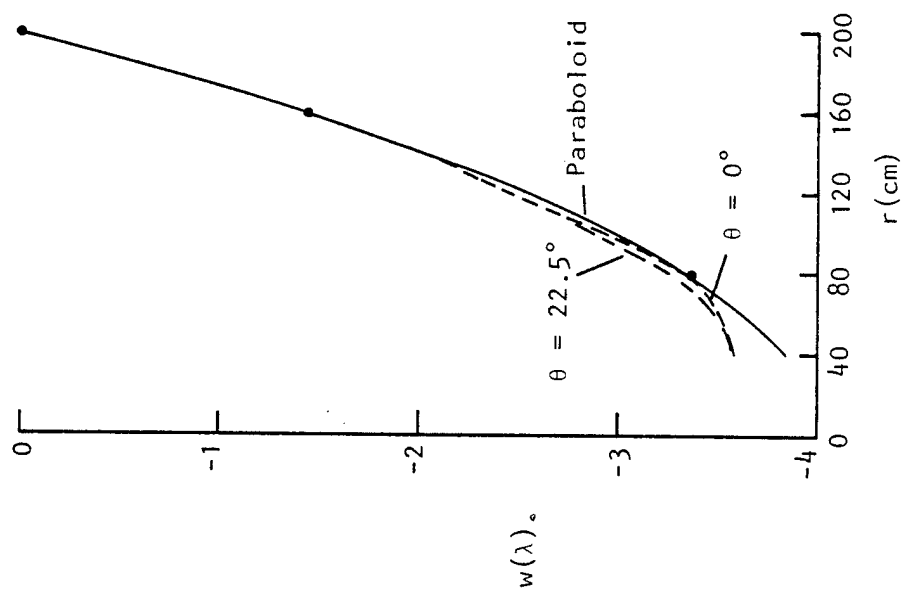


(a) Normal Position Control (b) Normal Position and Slope Controls

Fig. 4.14. Solid Mirror Model, Cross Sections for Defocus.



(a) Normal Position Control



(b) Normal Position and Slope Controls

Fig. 4.15. Thin Lightweight Mirror Model, Cross Sections for Defocus.

excellent. For all mirrors the defocus from displacement and slope control is nearly identical to that from only displacement control. No advantage is demonstrated here by adding slope control.

Mirror deflections were input to the FRINGE computer program to determine the rms value and span of the residual wavefront after defocus was removed. This data, along with an error ratio, is presented in Table 4.1 and further substantiates the superiority of the thick lightweight mirror when shifting focus.

Next, the mirror model was tested to see how well the actuators could position the mirror surface into the shape of an astigmatic aberration. The equation for the astigmatic surface is $w = Cxy$, where C is chosen so that the span is 4λ . Values of vertical displacement and slopes were computed for each actuator attachment grid. As for defocus, first only normal position controls were enforced, and next both normal position and slope controls were enforced at the 40 actuators.

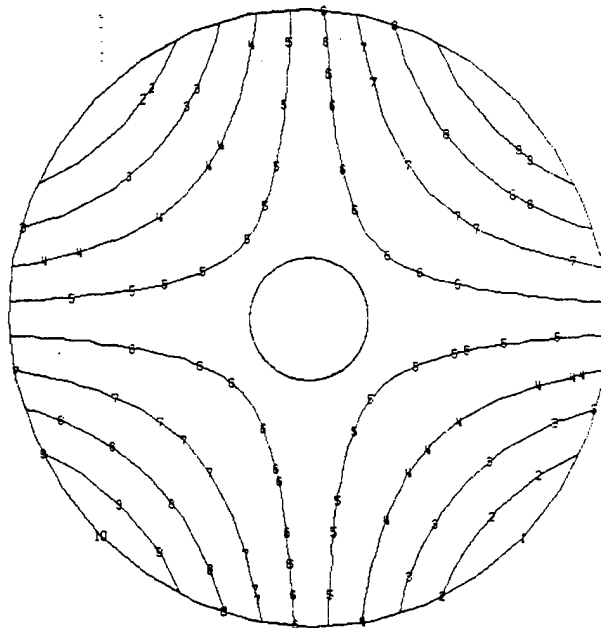
Figure 4.16 has the contour plots for astigmatism of the solid mirror. Plots for the other mirrors are not included, since they are so similar to the given contour plots that differences are undetectable with the naked eye. The data was numerically reduced by FRINGE into rms values, spans and error ratios appearing in Table 4.1. Error ratios are less than 1% for each of the three mirrors. The solid mirror has the largest error ratio for astigmatism, although it is still quite adequate. This same mirror had the lowest error ratio for defocus, since it has the largest ratio of membrane to bending stiffness. As for defocus, the addition of slope controls to normal position control has a negligible effect.

Table 4.1. Residual Wavefront Variations for Defocus and Astigmatism of Three Mirror Models

Mirror	Aberration	Span of Desired Aberration (λ)	Normal Actuation			Normal & Slope Actuation		
			rms (λ)	Span (λ)	Error Ratio (%)	rms (λ)	Span (λ)	Error Ratio (%)
Solid	Defocus	3.84	.0932	.687	18.	.082	.304	7.9
	Astigmatism	4.	.0016	.0090	.23	.0008	.0072	.18
Thick Lightweight	Defocus	3.84	.0213	.101	2.6	.0162	.0838	2.2
	Astigmatism	4.	.0024	.0243	.61	Data Not Available		
Thin Lightweight	Defocus	3.84	.0322	.246	6.4	.0275	.215	5.6
	Astigmatism	4.	.0016	.0147	.37	.0015	.0154	.39

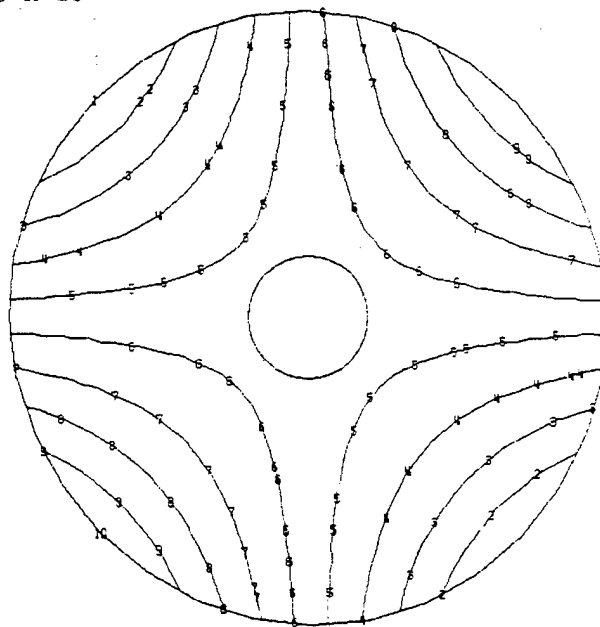
Note: Error Ratio = $\frac{\text{Span of Error After Actuation}}{\text{Span of Desired Aberration}}$

Max-Def = 1.26×10^{-4}
Min-Def = -1.26×10^{-4}



(a) Normal Position Control

Max-Def = 1.26×10^{-4}
Min-Def = -1.26×10^{-4}



(b) Normal Position and Slope Controls

Fig. 4.16. Solid Mirror Model, Astigmatism.

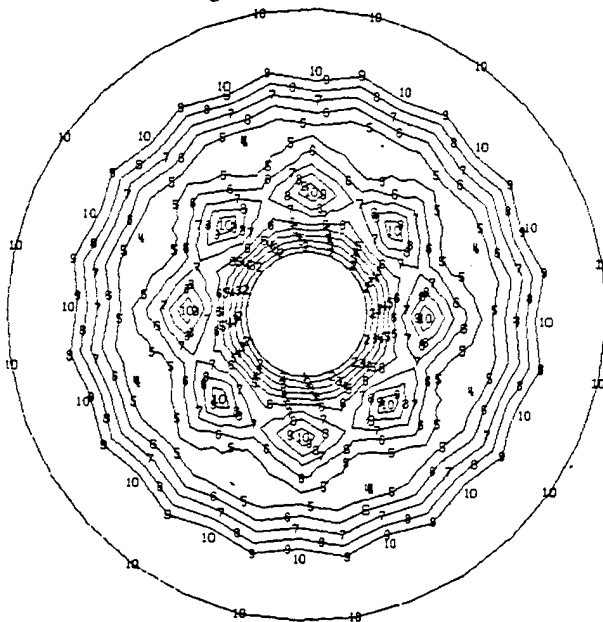
Gravity and Lap Loads

Gravity loads cause three different types of mirror deflection. The first is over-all mirror deflection. To analyze this, gravity is applied to the entire 40-actuator system finite element model. This will be reported in the next chapter. A second type of deflection is the sag between actuators, termed the inter-actuator deflection. Of course, this is part of the over-all mirror deflection. Nevertheless, it is studied here as a separate effect by using the mirror model with "perfectly rigid" supports of zero motion at the actuator grids. The only way to reduce the sag is to add more actuators and/or to stiffen the mirror. The third type of mirror deflection is intra-cell deflection and only applies to lightweight mirrors. Intra-cell deflections must be calculated analytically and superimposed upon deflections from the finite element method to arrive at the total deflection. When the mirror was modeled as a sandwich plate rather than as individual webs and faceplates, the assumption was made that over-all bending and intra-cell bending behave independently.

Intra-cell deflection actually comes from two sources, gravity and lap loads. For a square cell pattern the deflection equation of a square flat plate clamped on all edges is from Timoshenko and Weinowsky-Krieger (1959): $w = .00126 q a^4/D$. A square plate 4 cm across was loaded by a 1 g load normal to the plate and by a 1 psi lap load. The assumption is made that the lap tool is perfectly flexible. Intra-cell deflections are listed in Fig. 4.17(a). Deflections from

	<u>Solid Mirror</u>	<u>Thin Lightweight Mirror</u>	<u>Thick Lightweight Mirror</u>
Intra-cell deflection from gravity		.0021	.00076
Intra-cell deflection from 1 psi lap load		.23	.049
Gravity-induced sag between 2 inner rings of actuators (NASTRAN analysis)	21		
Gravity-induced sag between 2 inner rings of actuators (analytical)	21	8.9	1.9
Percent of previous analytical deflection due to shear	.18%	2.7%	11%
Gravity-induced sag at inner edge of mirror (NASTRAN analysis)	31		
Gravity-induced sag at inner edge of mirror (analytical)	31	13	2.7

(a) Mirror intra-cell and inter-actuator peak-to-peak deflections in wavelengths.



(b) Contour plot of inter-actuator sag of solid mirror due to gravity.

Fig. 4.17. Mirror Deflections Due to Gravity and Lap Loads.

gravity are negligible. Those due to the lap load are too large and somehow have to be reduced, either by using a thicker faceplate, by decreasing the cell dimension or by altering the lap load. With a 4 cm square cell and a 10% dense core, the webs are only 0.2 cm thick, which is already a meager value. For a triangular or hexagonal core, equations for deflections of plates of those shapes are available in Leissa and Nietenfuhr (1965).

Inter-actuator sag from gravity is shown in a contour plot in Fig. 4.17(b). The most severe sags occur along the unsupported inner edge of the mirror and between the inner and middle rings of actuators. A NASTRAN analysis was run for the solid mirror only. To predict deflections for the two lightweight mirrors, three 80-cm diameter circular flat plates simply supported along the outer edge are loaded by gravity. Again, the deflection equation

$$\frac{(5 + \nu)}{64(1 + \nu)} \frac{q R^4}{D}$$

is from Timoshenko and Weinowsky-Krieger (1959). The plate dimension was chosen to coincide with that of the unsupported section of the mirror. Fig. 4.17(a) lists the inter-actuator sag between the two inner rings of actuators as 21λ for the NASTRAN analysis. For the solid circular flat plate the result is 26 cm. The constant in the deflection equation was scaled to change this to 21λ and the same scaling factor was used for the lightweight plates. The same deflection equation can be scaled to predict the deflection at the inner edge of the lightweight mirrors. It is not necessary to change the radius or

the constant due to the boundary conditions, since these changes would be eliminated when the analytical solution is scaled by the NASTRAN result. The inter-actuator sags are too large to be ignored, especially for the solid mirror, and they are a controlling factor in the design, testing and operation of an active primary mirror.

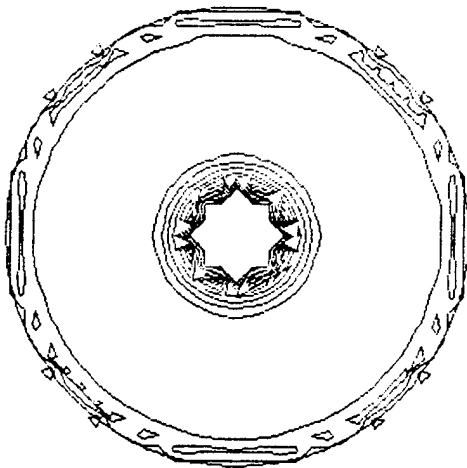
FRINGE Data Reduction

FRINGE (Loomis, 1976) is a computer program for the analysis of interferometric test data. It is used here to subtract a reference surface from mirror deflections and to calculate the root-mean-square value and span of the residuals. A percentage error ratio between inactive and active mirrors is based on these values. The reference surface may include tilt, focus and/or astigmatism.

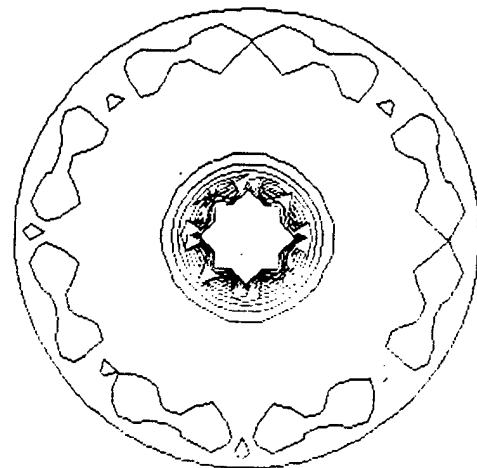
Three different residuals are found by FRINGE. The first residual is obtained by subtracting the reference surface from each of the mirror displacements at 288 grid points on the mirror. The second residual is obtained by subtracting the reference surface from the Zernike polynomial approximation to the data calculated over a mesh of uniformly spaced points. The third is from subtracting the reference from a mesh of uniformly spaced data points calculated by linear interpolation of the displacement of 288 grid points. The second and third residuals are better than the first, since they in effect weight the grid point displacements based on surface area. The preference between the second and third residuals depends upon the accuracy of the Zernike polynomial fit. Data is provided to show that the fit is poor. Thus the rms value using the residual based upon linear

(a) Rms Deviation between Polynomial and Grid Point Displacements in Wavelengths--"None" and "Normal" Refer to no Correction and Normal Position Control, Respectively.

No. of Terms	x gravity of 1 g		z gravity of 1 g		Axial thermal gradient of 1° C		Uniterm thermal soak of 1° C	
	None	Normal	None	Normal	None	Normal	None	Normal
0	19.3	2.00	62.6	13.5	.038	.036	.241	.014
2	13.1	1.99	53.8	13.5	.038	.036	.241	.014
3	13.1	1.99	48.4	9.30	.037	.032	.039	.011
8	6.12	1.98	25.0	9.26	.027	.023	.033	.018
15	4.05	1.85	11.4	9.23	.022	.020	.029	.009
24	2.82	1.72	8.57	7.23	.012	.011	.019	.007
36	2.11	1.57	4.22	2.91	.005	.006	.009	.006



(b) Contour plot of 36 term Zernike polynomial



(c) Contour plot of linear interpolation of grid point displacements

Fig. 4.18. Fringe Data to Support Choice of Residual for rms Calculation.

interpolation of the displacements was used to generate values appearing throughout this report.

Tabulated data in Fig. 4.18(a) demonstrates the decrease in rms deviation between polynomials with increasing numbers of terms and the displacements at the 288 grid points. Displacements are from four different loads applied to the 40-actuator system and will be discussed further in the next chapter. If the polynomial fit the data perfectly, the rms deviation would be zero. Even for the complete 36 term Zernike polynomial, rms values are typically not reduced on order of magnitude from that of the raw data (number of terms = 0). For the worst case the rms value for the complete polynomial is 79% of the rms of the raw data. Figures 4.18(b) and (c) are two contour plots for the mirror loaded by a 1°C axial thermal gradient, corrected by normal position control and with no reference surface removed. These plots were generated by FRINGE and should be compared to the NASTRAN generated plot in Fig. 5.28(b). The plot from linear interpolation of nodal point displacement gives a better representation of the NASTRAN plot than the 36 term Zernike polynomial plot. Part of the problem with the 36 term polynomial is that the highest order angular terms involve sin and cos of 5θ , while there are 16 actuators in each of the two outer actuator rings.

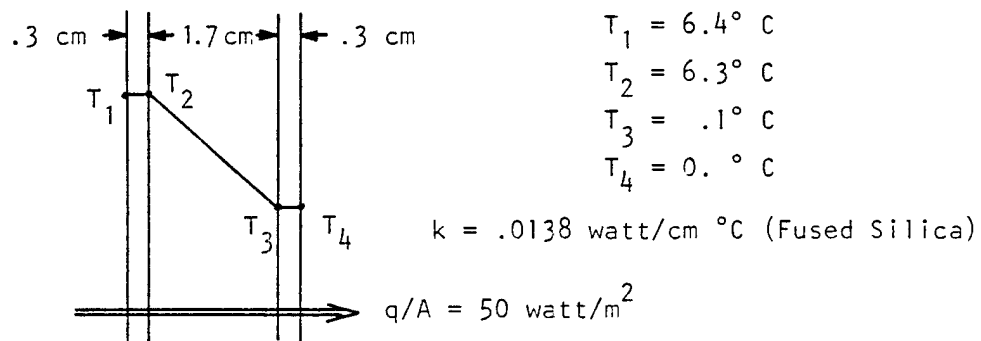
Heat Transfer

Heat transfer analyses were performed to estimate temperatures across the mirror cross section. It was assumed that the axisymmetric axis of symmetry of the mirror was pointing toward the sun, so that the support structure was hidden in the shadow of the mirror. This would be a "worst case" of radiation input.

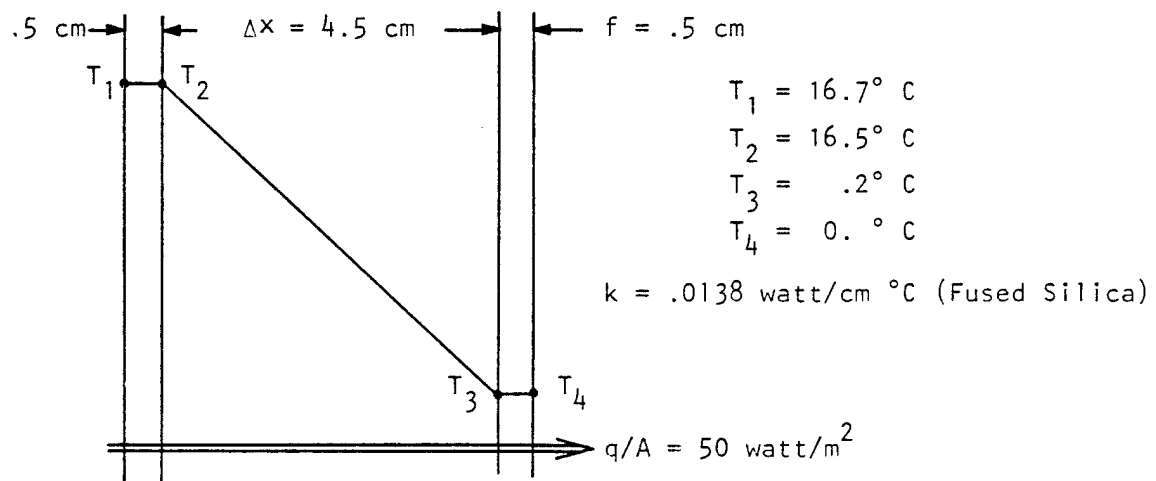
A one-dimensional steady state heat conduction analysis was performed, since it was assumed that thermal gradients from this type of analysis would be an upper bound. Using a heat transfer rate per unit area of $q/A = 1 \text{ kW/m}^2$ for sunlight and assuming a 5% mirror coating absorbtivity, the rate through the mirror becomes $q/A = 50 \text{ W/m}^2$. Temperatures from that analysis are shown in Fig. 4.19.

The temperature gradient across the core is the same for both sandwich mirrors. The temperatures for the solid mirror were input to a NASTRAN structural analysis of the 40-actuator system. Since both the heat transfer and structural analyses are linear, a change in the value of the heat transfer rate can be accomodated by scaling of the results of the structural analysis.

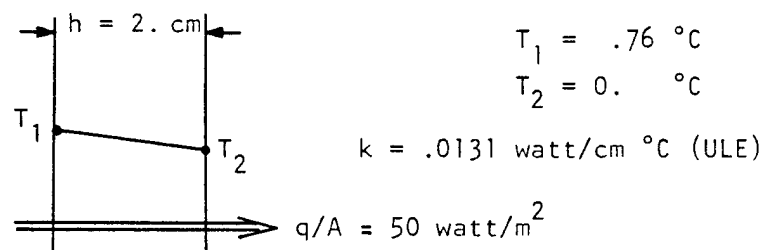
Other heat transfer analyses that could be performed include (1) transient analyses to confirm that the temperature gradient due to steady-state heat conduction is indeed an upper bound, (2) two- and three-dimensional analyses, (3) heating of the support structure due to conduction and radiation, and (4) heating of the entire system due to orienting the system in different positions with respect to the sun.



(a) Thin Lightweight Mirror



(b) Thick Lightweight Mirror



(c) Solid Mirror

Fig. 4.19. Approximate Thermal Models.

It may be desirable to utilize NASTRAN's heat transfer analysis capability in further refinements.

CHAPTER 5

40-ACTUATOR SYSTEM

The description of the finite element model for the complete 40-actuator system includes tables of material properties, structural cross sections and mass summaries. The 2 cm thick ULE solid mirror is given priority in analyses over lightweight mirrors of sandwich construction. Ultra high modulus graphite epoxy is used for the support structure. A three point kinematic mount is most frequently employed, but benefits of a flexural mount are also explored. The mechanical design utilizes flexures for positive, frictionless connections and electric servomotors. Actuation forces in the model are introduced by temperature changes to structural elements.

Results from individual normal position and slope controls are extremely encouraging. A system with a small reference plate weighing only 35% of the solid mirror has less than 4.5% cross coupling between normal position controls. Apparently the optimization curves developed for the 2-dimensional system model are applicable to the 3-dimensional model.

For all remaining analyses the determination of actuator forces, which would be accomplished by an on board computer in the operational system, is performed apriori by yet another complicated series of analyses. The control system makes optical displacement measurements of both position and slope at actuator attachment points on the mirror surface and controls actuator forces to set the actuator

displacements to a predetermined magnitude. For gravity and thermal loads the magnitude is zero.

Analyses to evaluate the design of the 40-actuator system involve the following mechanical loads: (1) gravity loads to determine deflection due to a 1 g release in the space environment, (2) a thermal gradient through the mirror thickness to simulate sunlight, (3) a uniform thermal soak of the entire system to simulate a change in temperature in the spaceborne telescope from that of final figuring and testing, (4) loads to defocus the mirror to investigate scalloping, and (5) loads to deform the mirror into the shape of fourth-order astigmatism. For these analyses the solid mirror with a small reference plate were used most often. Analyses were performed twice, once for normal position control and once for both normal position and slope controls, so that the added complexity and expense of slope controls could be weighed versus increased performance. The FRINGE computer program removed tilt and defocus from deflections, so rms values correspond to the variation from the best fit sphere. Tilt and defocus were not removed from contour plots. In many instances two rms values were calculated for the same mirror deflection. Since there are no actuators at the edge of the hole in the mirror, deflections along this edge are predominant and are reduced by masking. One rms value is based upon the deformation of the entire mirror, while a second rms is for the section of the mirror within the inner ring of actuators masked off, reducing surface area 12.4%.

For the solid mirror it is impossible to defocus with accuracy, but astigmatism can be very accurately enforced, especially when including slope control. All previous arguments about ease of enforcement of developable vs nondevelopable shapes apply once again.

Gravity caused deformations are so great for the system with a solid mirror, a small reference plate and a kinematic mount, that even if the mirror were stood on edge the residual after control is 1λ rms. This mirror may need some means of support for ground testing. A flexural mount around the entire periphery of the reference plate alleviates gravity deformations and leaves them susceptible to control, especially when the mirror is stood on edge.

For the solid mirror system deflections due to exposure to sunlight and from a uniform thermal soak of the entire system are very well behaved, because of the efficiency of the integrated structure. Actuation admirably corrects the latter load, but is incapable of handling the former.

Stresses throughout the system have adequate safety margins for all loads, including the 10 g launch load. Buckling is not a problem either.

Actuator strength and stroke and actuation sensitivity (based on mirror deflection) aid in the choice of the servomotor.

Finite Element Models

The finite element model of an active mirror system with 40 actuators and a 4-meter diameter primary mirror was generated using the Graphics-Oriented Interactive Finite Element Time-Sharing System (GIFTS)

on an Eclipse minicomputer at the University of Arizona. GIFTS is an effective preprocessor for NASTRAN. The entire model was generated, plotted, and checked for accuracy using GIFTS in a fraction of the time of conventional methods. An interface program was written to convert the output data from GIFTS into input data for NASTRAN. Structural analyses were then performed on the model using the MSC/NASTRAN computer program on the AFWL Cyber 176 computer at Kirtland AFB, New Mexico. The same Eclipse minicomputer used to generate the model was configured to emulate a Control Data 200 User's Terminal that was connected by telephone to the AFWL computer.

Specifications

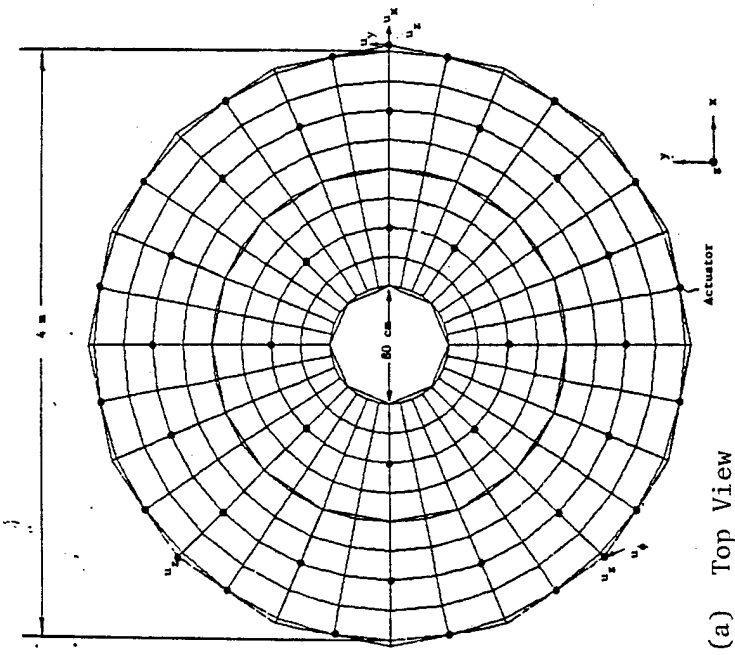
Three views of the mathematical model are shown in Fig. 5.1.

The model is composed of the following:

Mirror	256 plate elements (CQUAD4)
Reference Plate	104 beam elements (CBAR)
Actuator Posts	80 beam elements
Sliders	40 beam elements
Truss Members	160 beam elements
Dummy Rods	40 rod elements (CROD)
Entire Model	530 grid points

After constraints are applied, the solution involves 2,642 simultaneous equations. Beams account for shear deformation by incorporation of a cross sectional form factor.

Material properties and structural cross sections are defined in Fig. 5.2. Mirror cross section dimensions are larger than desired, but



(c) Orthographic Projection of Top View
Rotated -30° about x axis

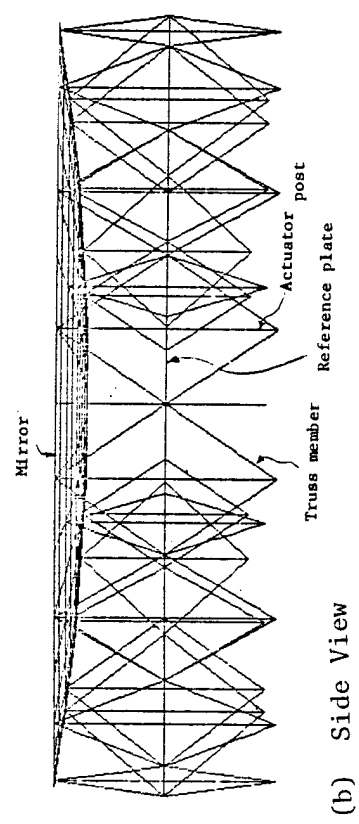
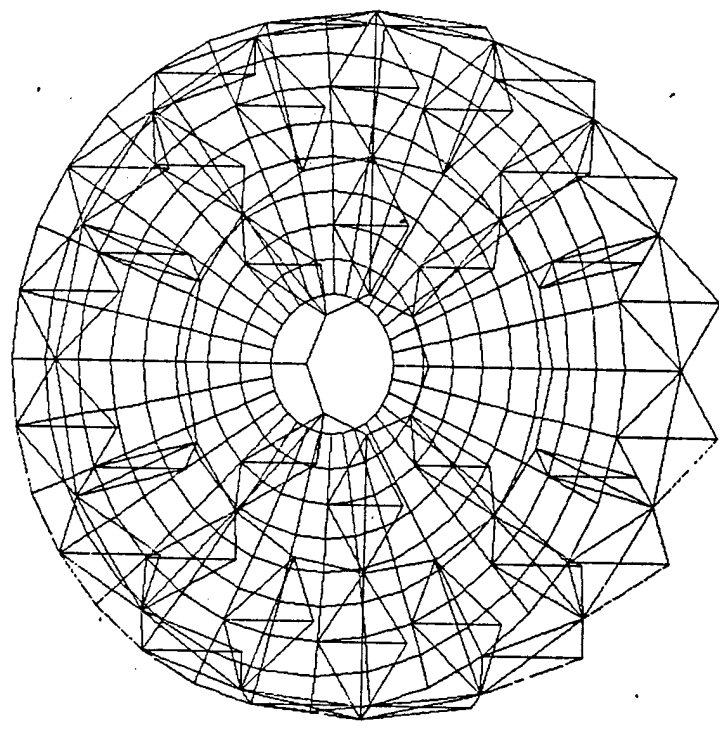
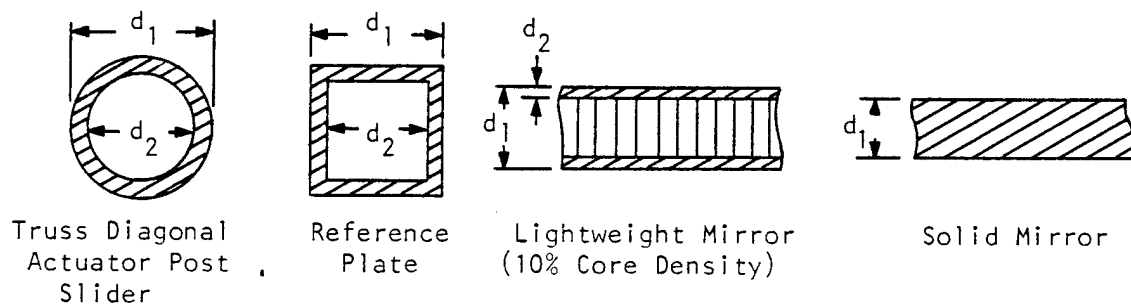


Fig. 5.1. 40-Actuator System. Undeformed Shape.



(a) Cross Sections

<u>Member</u>		<u>d_1 (cm)</u>	<u>d_2 (cm)</u>
Truss Diagonal		2.16	1.52
Actuator Post		4.32	3.05
Slider		2.79	2.16
Reference Plate	- Small	6.99	4.45
	Normal	12.7	10.2
Mirror	- Thick Lightweight	5.5	.5
	- Thin Lightweight	2.3	.3
	- Solid	2.	

(b) Cross Section Dimensions

<u>Material</u>	<u>E (dyne/cm²)</u>	<u>μ</u>	<u>ρ (gm/cm³)</u>	<u>α (/°C)</u>	<u>σ_{ULT} (psi)</u>
ULE	6.76×10^{11}	.17	2.214	$.03 \times 10^{-6}$	7,200
Graphite Epoxy	2.14×10^{12}	—	1.55	$.18 \times 10^{-6}$	52,000

(c) Material Properties

Fig. 5.2. Cross Sections and Material Properties for 40-Actuator System.

were chosen as being representative of the minimum feasible for a 4-m diameter mirror. In a few situations the values are different from those in Fig. 5.2. This occurs for results extracted from a prior work. Comments in the text will identify these situations.

The graphite epoxy material system chosen was ultra high modulus GY-70/X-30 rather than a high strength system. The symmetric layup [0/45/0/135/0] was chosen over a pseudoisotropic layup [0/45/90/135]. For the symmetric layup E is 72% higher, while α for the pseudoisotropic layup is about the same as for ULE. The higher stiffness has priority over the ultra low thermal expansion. Composite properties are from two reports (Holmes, 1979; Armstrong and Ellison, 1979).

Table 5.1 summarizes the mass of three different versions of the 40-actuator system. Servomechanism weight is 2 lb at each of 40 locations, and is based upon the weight of the servomechanisms in the 41-actuator physical model. The mass of the intelligence of the control system has not been included.

Mounts

For most analyses, and unless specified otherwise, the 40-actuator system is mounted by a three point kinematic mounting system at the reference plate. Figure 5.1(a) identifies the six degrees of freedom on the periphery of the reference plate that are constrained to zero motion. Displacements u_x , u_y , and u_z are displacements in the x, y, and z directions, while u_ϕ is the displacement in a skewed direction, normal to the line connecting two of the support points. With this ball, vee and flat arrangement the telescope tube can distort due to thermal loading without any restraint from the supports.

Table 5.1 Mass Summary for Three Versions of 40-Actuator System

Structure	System with solid mirror and small reference plate	System with solid mirror and nominal reference plate	System with thin lightweight mirror and small reference plate
Mirror	534	534	206
Reference Plate	189	377	189
Actuator Posts	47	47	47
Truss Rods	30	30	30
Sliders	8	8	8
Servomechanisms	36	36	36
Total Mass (Kg)	844	1032	516
Total Weight (Lb)	1870	2280	1140
Total Mass/Mirror Surface Area (Kg/m ²)	70	86	43

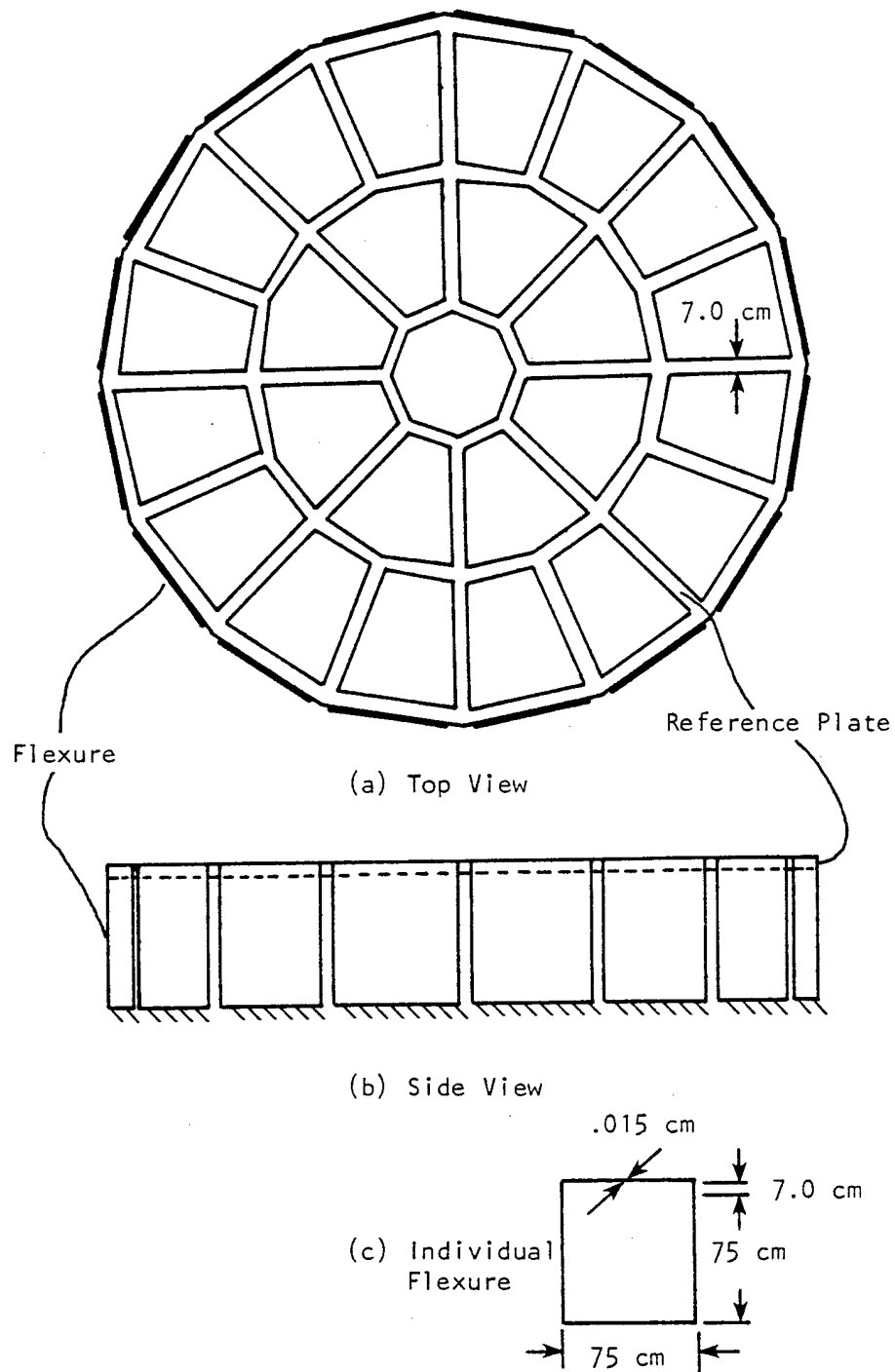
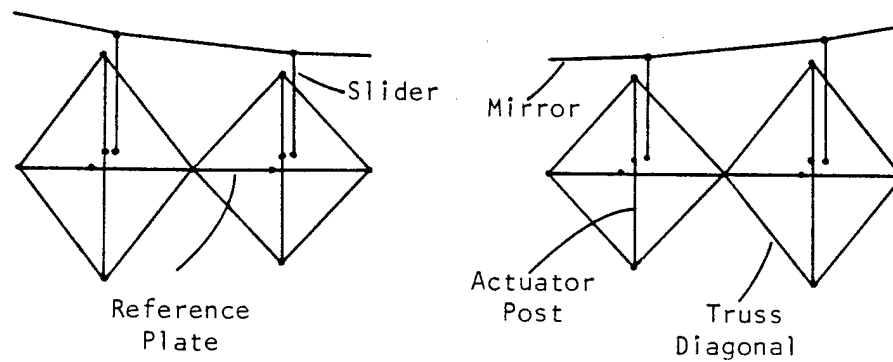
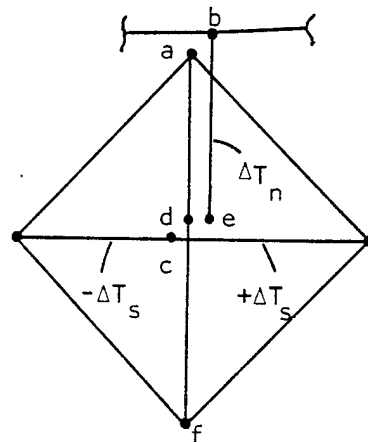


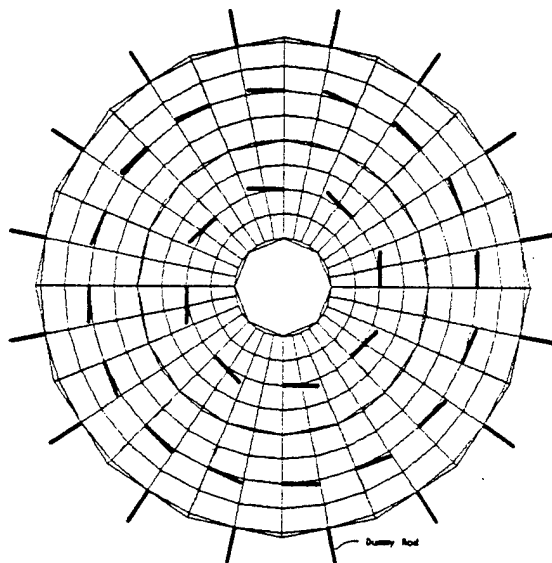
Fig. 5.3. Reference Plate and Supporting Flexures.



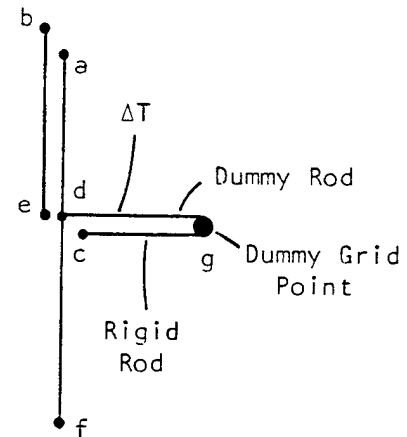
(a) Section View of Finite Element Model Along x-Axis



(b) Normal Position Control and In-Plane Slope Control

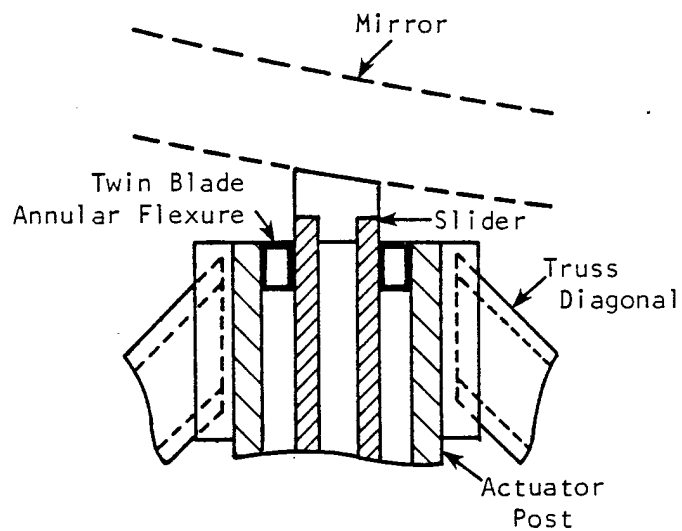


(c) Dummy Rod Locations on Finite Element Model

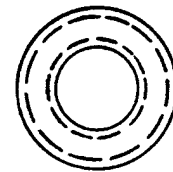


(d) Out-of-Plane Slope Control

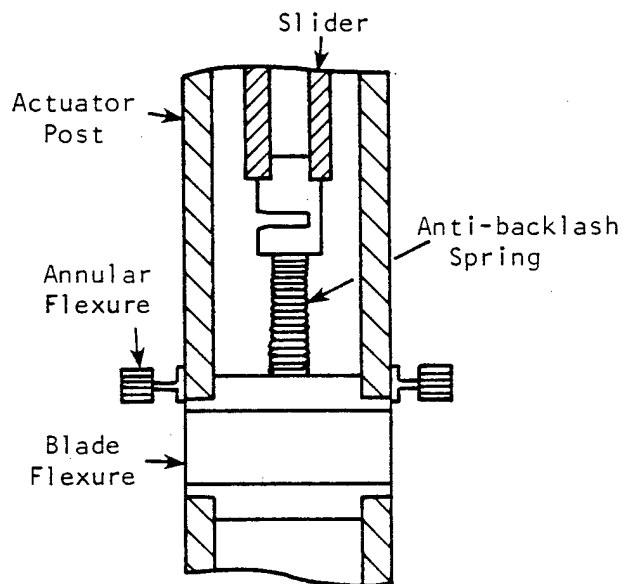
Fig. 5.4. Normal Position Control and Slope Control Models.



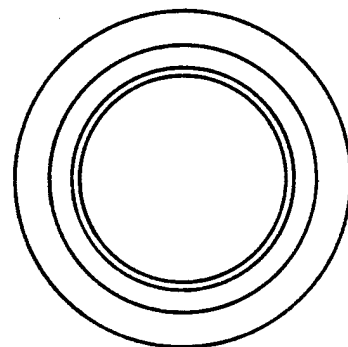
(a) Top of Actuator Post



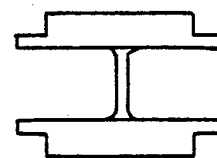
(b) Twin Blade Annular Flexure



(c) Middle of Actuator Post



(d) Annular Flexure



(e) Blade Flexure

Fig. 5.5. Actuator Post Flexures.

Print through of the three point support, exhibited at the mirror's surface, dictated consideration of the flexural mount in Fig. 5.3. This figure also presents an unobstructed view of the reference plate. Using thin flexures, the reference plate can grow radially with inconsequential reactions from the flexures. The design criteria for sizing the flexures is to uncouple the mirror from dynamic disturbances in the telescope by making the natural frequencies of the mount exceed 30 Hz (ITEK, 1970, pp. 5-22). To model the flexures, 16 bar elements and 16 grid points were added to the model. Bar elements were used instead of plates to account for the individuality of the flexures.

Mechanical Design of Controls

A sectional view of the model cut by the plane with $y = 0$ is shown in Fig. 5.4(a). In two regions the individual grid points are shown slightly offset for clarity, but the coordinates of these grids coincide in the finite element model. The three active controls, normal position control and in-plane and out-of-plane slope controls, will be discussed one at a time with the aid of mechanical drawings of actuator post flexures and of the servomechanisms. Special attention will be given to actuation loads and connections between structures for both the mechanical design and the finite element model.

The model for normal position control is Fig. 5.4(b). Figure 5.5 shows that the slider physically moves up and down inside the tubular actuator post. Chapter 3 analysis of a 2-dimensional model of an

integrated active mirror system concluded that nodes a and b, at the top of the actuator post and slider, should be rigidly attached except for vertical motion. This motion coincides with degree of freedom (d.o.f.) T3 of the cylindrical coordinate system in Fig. 4.9. To provide the necessary restraint, a twin blade annular flexure connects the top of the slider to the post. In the finite element model, NASTRAN zero length rigid bars conveniently generate multipoint constraint (MPC) equations that equate displacements of nodes a and b for d.o.f.'s T1, T2, R1, R2, and R3. Effectively, the spring stiffness for five relative motions are infinite, and stiffness for the sixth motion is zero. All flexure connections will be modeled this way, by either rigid or perfectly flexible connections. Justification of this simplification is also in Chapter 3. Mating of the bottom of the slider to the actuator post was shown with the 2-dimensional model in Chapter 3 to be critical only for vertical motion. Figure 5.6 depicts an eccentric arm on the output shaft of the normal position control servomechanism. This arm fits into the slot at the bottom of the slider in Fig. 5.5. A preload spring between the actuator post and the slider eliminates backlash. In the finite element model at grid points d and e only d.o.f. T3 is connected between the slider and the actuator post. The other five d.o.f.'s are released with NASTRAN pin flags in the slider element.

Now that the various mechanical parts required for normal position control have been interconnected, the model must be loaded to simulate the vertical motion of the slider due to rotation of the eccentric arm. As discussed in Chapter 3, in order to mathematically

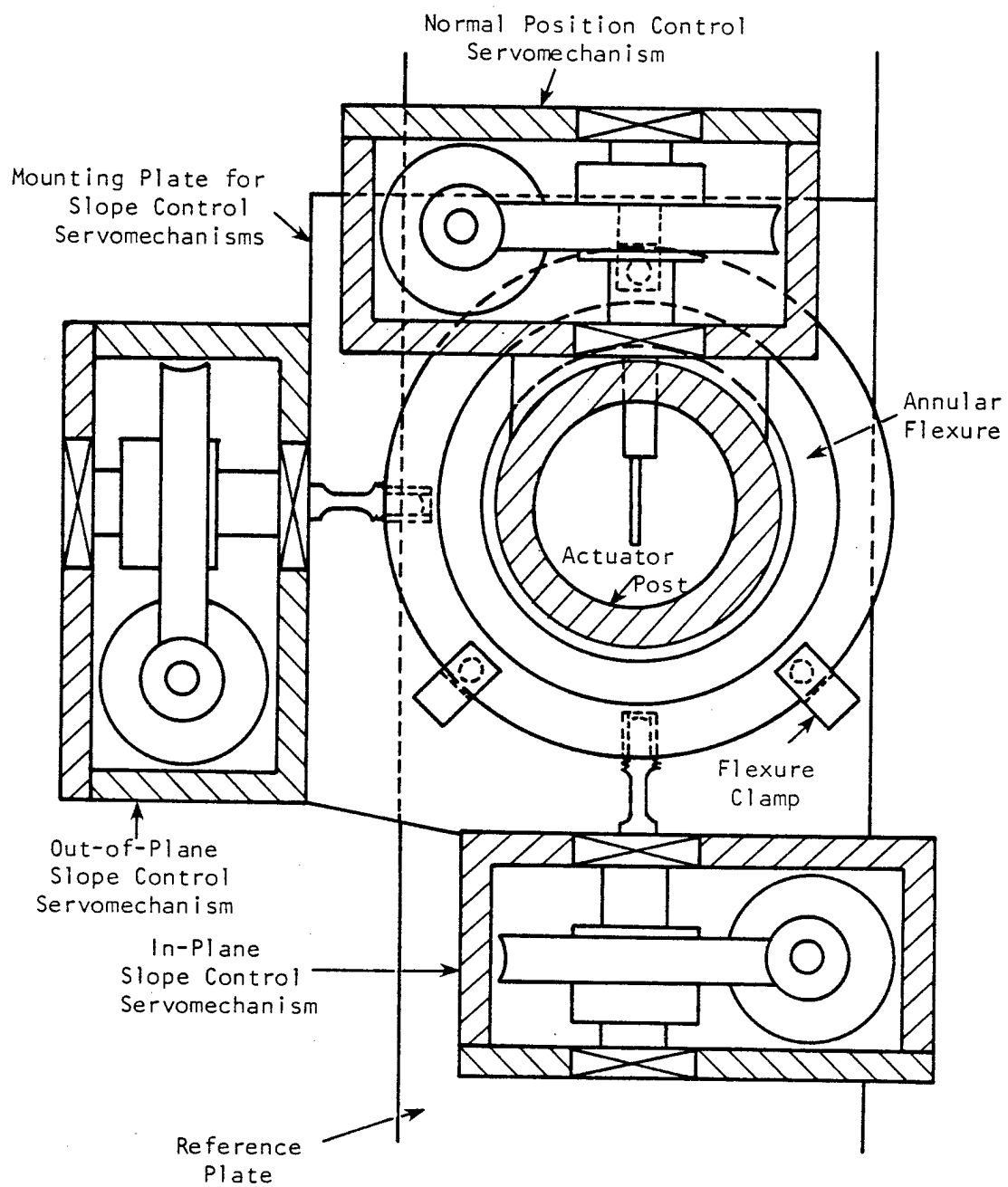


Fig. 5.6. Plan View of Servomechanisms.

determine loads necessary to enforce a prescribed deflection pattern upon the mirror, grid connections must remain unchanged. Therefore, instead of temporarily disconnecting grid points d and e for d.o.f. T3 and applying equal but opposite forces on these members, these grids are held fixed and a change in temperature ΔT_n is applied to the slider.

In-plane slope control is also shown in Fig. 5.4(b). The connection between the middle of the actuator post and the reference plate is with an annular flexure, permitting relative motion for d.o.f.'s T3, R1 and R2 between grids c and d. The flexure is represented by a zero length rigid bar. Figure 5.6 illustrates that both in-plane and out-of-plane slope control servomechanisms utilize a screw drive to position the annular flexure, which in turn positions the middle of the actuator post. Three spring loaded clamps with Teflon bearing surfaces keep the annular flexure in alignment. A blade flexure, which acts like a hinge, is inserted in the middle of the actuator post to reduce the force required to rotate the mirror. The flexure is modeled by a pin flag at grid d, which allows no moment transmission about a local axis perpendicular to the plane of the truss. The influence of the flexure upon the deflections of the actuator post is shown in Figs. 5.8(c) and (d). The deflection of the post and the ensuing mirror rotation are instigated by positive and negative temperatures of equal magnitude applied to the two bar elements representing the reference plate.

To implement out-of-plane slope control on the computer, it was necessary to add dummy rods, rigid rods and dummy grid points.

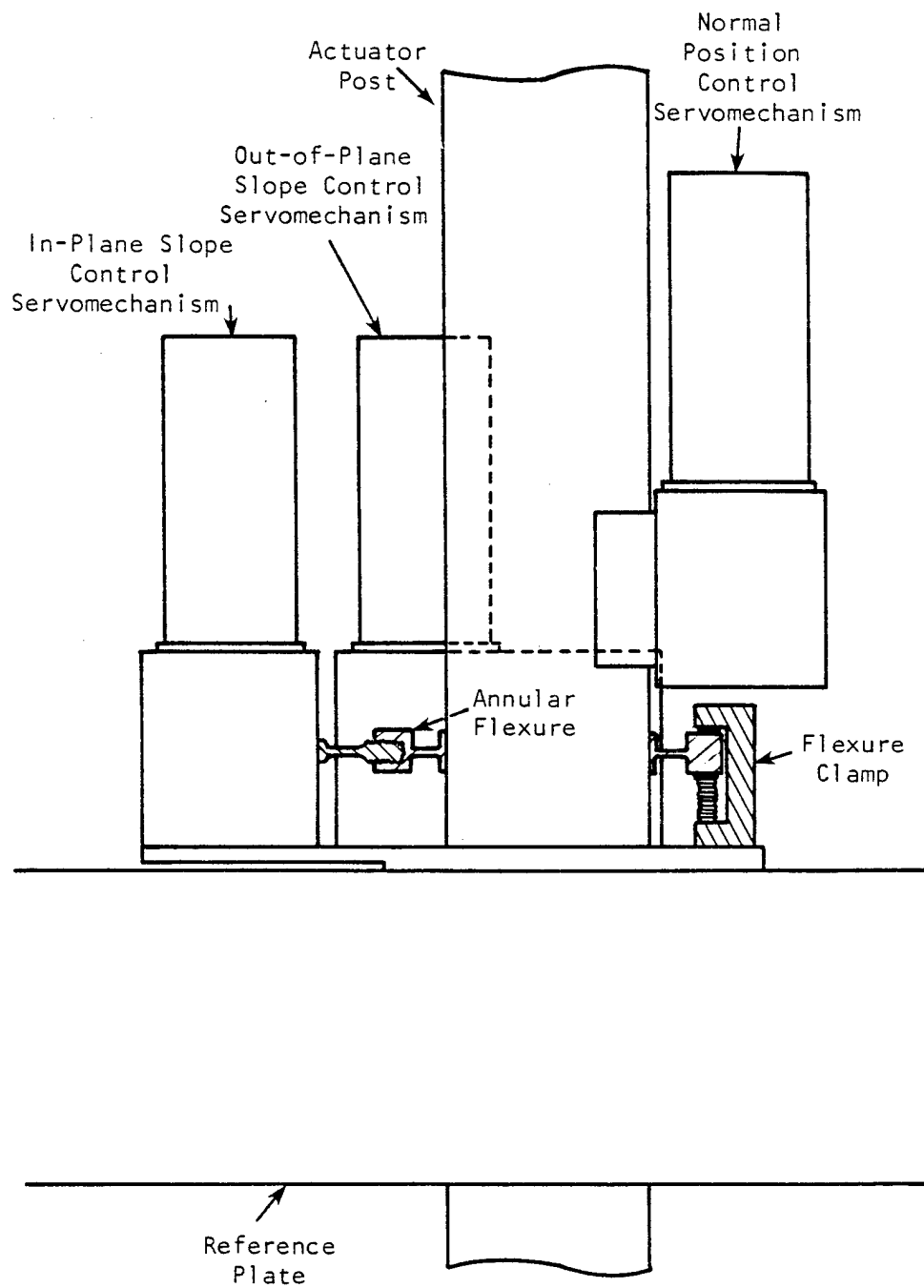
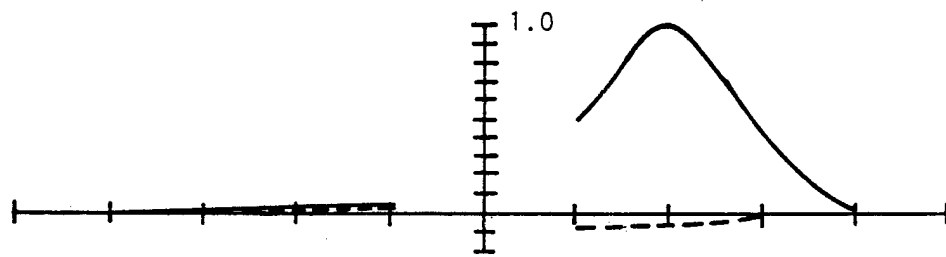
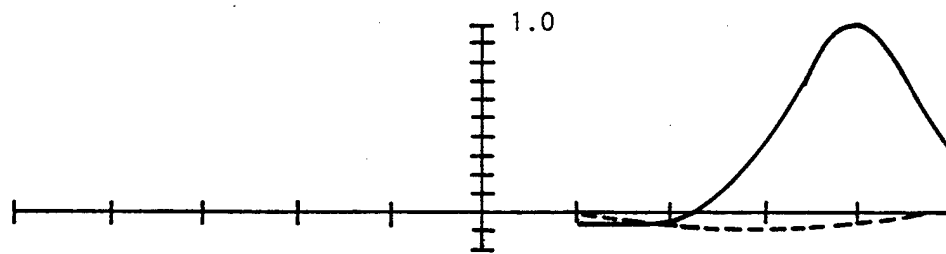


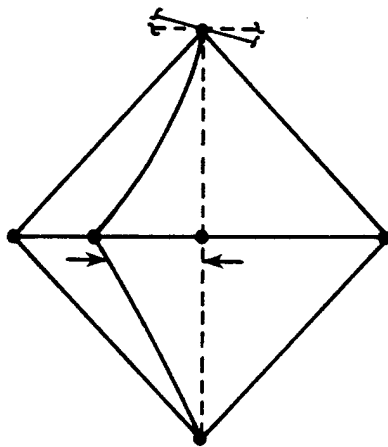
Fig. 5.7. Side View of Servomechanisms.



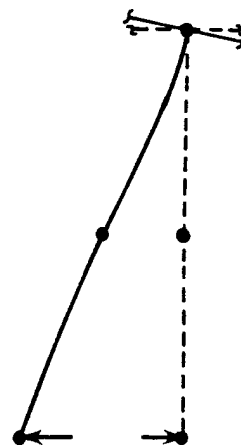
(a) Normal Position Control for 80 cm Actuator.



(b) Normal Position Control for 160 cm Actuator.



(c) In-Plane Slope Control



(d) Out-of-Plane Slope Control

Fig. 5.8. Normalized Deflections for Normal Position Control and Slope Controls.

Figure 5.4(c) shows all the dummy rods, each positioned normal to a truss. In Fig. 5.4(d) the dummy rod and rigid rod are shown offset for clarity, but they actually coincide. The rigid rod connects to the reference plate at c and the dummy rod connects to the actuator post at d, and both connect to the dummy grid. When the length of the dummy rod is altered by a change in its temperature, the mirror rotates. The displacement coordinate system for the dummy grid is aligned with the dummy rod, and translation parallel to the rod is unrestricted, while all the other five d.o.f.'s are held fixed. This requires 40 different coordinate systems, one for each dummy grid.

Servomotors are similar to the ones used by Radau (1977, p. 124) for the experimental test of the 41-actuator system. In each of the three servomechanisms in Fig. 5.6 and 5.7, the servomotors couple to the drive shafts through worm and wheel gears. The teeth lock when the wheel on the output shaft attempts to drive the worm. In addition to this gear, the gear ratio of the servomotor must be high and the coupling mechanism to the driven part must be precise to control motion to fractions of a wavelength. For instance, a differential screw with thread sizes of 30 and 31 threads/in is equivalent to a simple drive screw with 930 threads/in. Also the eccentricity of the arm for normal position control may be minute.

Testing the Model

The finite element model was meticulously tested. During its formulation, GIFTS plots were generated interactively on a CRT. The

GIFTS to NASTRAN interface was checked by NASTRAN plots. The NASTRAN computed system weight agreed with hand calculations. Rigid body checks verified constraints from MPCs and rigid elements. At a grid point, one rigid body motion was given a unit displacement while the other five motions were constrained, and displacements of all grid points were examined. This was done for each of the six rigid body motions with one stiffness matrix decomposition by using the SPCD card which, internal to NASTRAN, transforms enforced displacements into loads. The following is a list of some items checked on the model:

- (1) element connectivity, length, area, aspect ratio and warpage
- (2) grid point d.o.f. sets
- (3) diagonal terms of assembled global stiffness matrix
- (4) maximum ratio of terms on diagonal of assembled stiffness matrix to corresponding terms on diagonal of upper triangular factor, i.e., a measure of stiffness matrix conditioning
- (5) grid point force balance, listing element and constraint forces
- (6) residual load vector $\delta P = Ku - P$
- (7) ratio of work by residual load vector to work by applied load vector

$$\epsilon_e = \frac{u^T \delta P}{u^T P} \quad (\text{Joseph, 1979, pp. 7.5-11})$$
- (8) forces of single point constraint
- (9) load vectors
- (10) element force, stress and strain energy
- (11) grid point displacement

Normal Position and Slope Controls

The structure supporting the mirror includes a reference plate, actuator posts and truss diagonals. The stiffness required of the mirror's support structure depends upon the mirror stiffness. The goals of the integrated active mirror system are to localize deflections due to individual controls while minimizing weight. Figure 5.8 demonstrates localized deflections for the system with the solid mirror and the lightweight reference plate. In Figs. 5.8(a) and (b) normalized mirror (solid line) and reference plate (dashed line) deflections are superimposed for grids along the x axis. Mirror deflection is localized to an area of roughly one-fifth the mirror's diameter. Deflection of the reference plate is more broad, with its maximum value less than 10% that of the mirror. Plots showing the mirror's localized deflection during slope controls are labeled theory in Fig. 2.10. These plots are for the 41-actuator system, but localization of deflection for the 40-actuator system is analogous. Figure 5.8(c) and (d) portray actuator post deflection during slope controls. Deflections are greatly exaggerated, but the actuator post's shape is accurately drawn.

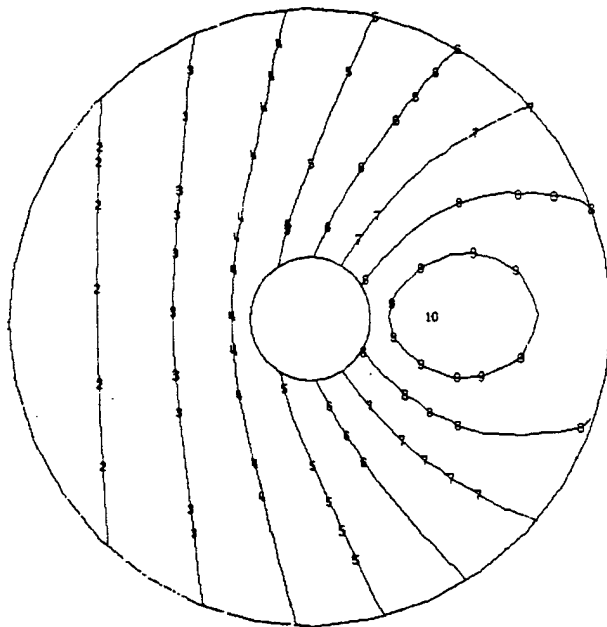
Several different combinations of mirrors and support structures were analyzed for the 40-actuator system. The remaining figures in this section are contour plots for normal position and tangential and radial slope controls for some of the combinations. Contour plots are included for nine controls, i.e., for normal position, tangential slope and radial slope controls for actuators located 80 cm, 160 cm and 200 cm from the center of the

mirror. Loads in these analyses are provided by a 1°C temperature change in the appropriate structural element(s). Such small loads created fractional wavelengths of displacement, but since analyses are linear, results can be scaled. To evaluate the effectiveness of the integrated structure, these contour plots should be compared to those in Chapter 4, generated with the mirror model with its "perfectly rigid" support structure.

Contour plots in Figs. 5.9-11 for the thick lightweight mirror reveal that the deflection of the mirror surface by one actuator is not localized to the vicinity of that actuator. Significant deflections occur across the entire mirror. This is totally unsatisfactory. It occurs since the bending stiffness of the mirror is large relative to the stiffness of the support structure. The reference plate and the remainder of the support structure for this system were more flexible than the system shown in Fig. 5.2. The structural properties of the thick lightweight mirror system have been documented (Shannon, Richard, and Hansen, 1980, p. 36). To design a stiffer support structure, stiffnesses were calculated for each of the major components of the system, i.e., extensional stiffness of an individual truss, bending stiffness of the section of reference plate bounded by a single truss, and bending stiffness of a circular section of mirror with diameter equal to the horizontal span of a single truss. Additional material was added where appropriate.

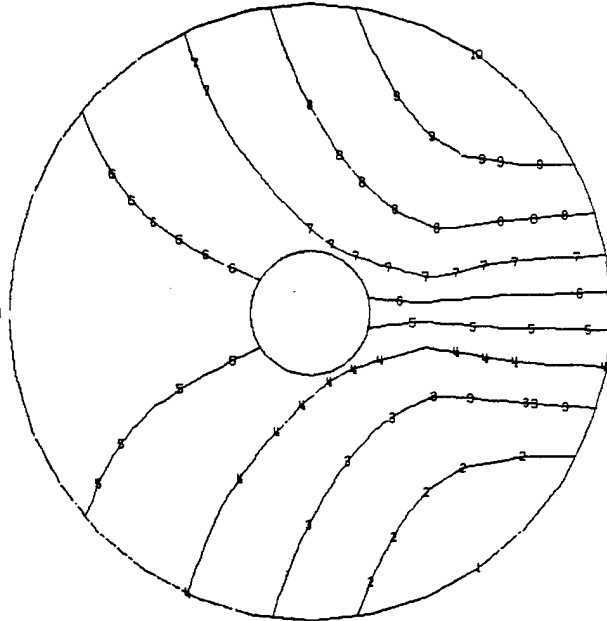
During design iteration, the truss members were changed from steel wires, which would require pretensioning, to graphite epoxy truss rods, which could support compressive forces and therefore would not

Max-Def = 1.41×10^{-13}
 Min-Def = -3.32×10^{-14}



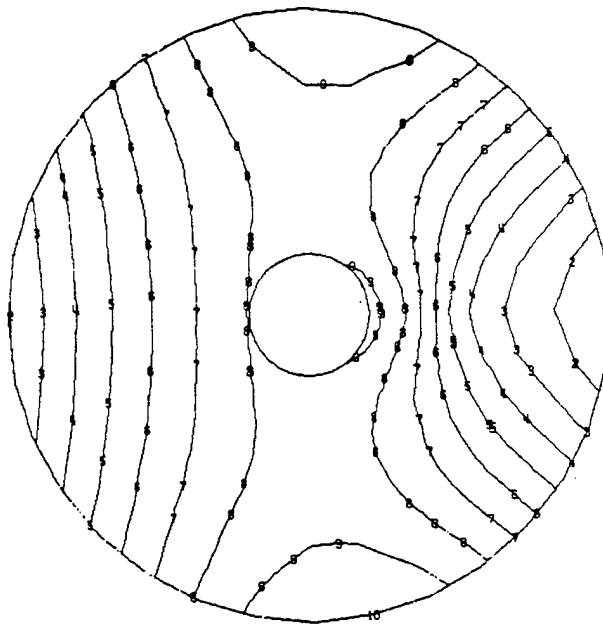
(a) Normal Position Control

Max-Def = 1.45×10^{-10}
 Min-Def = -1.45×10^{-10}



(b) Tangential Slope Control

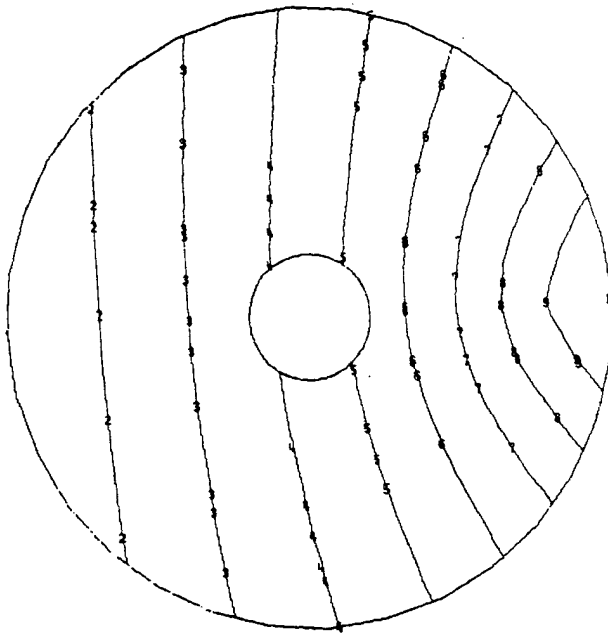
Max-Def = 6.06×10^{-11}
 Min-Def = -1.85×10^{-11}



(c) Radial Slope Control

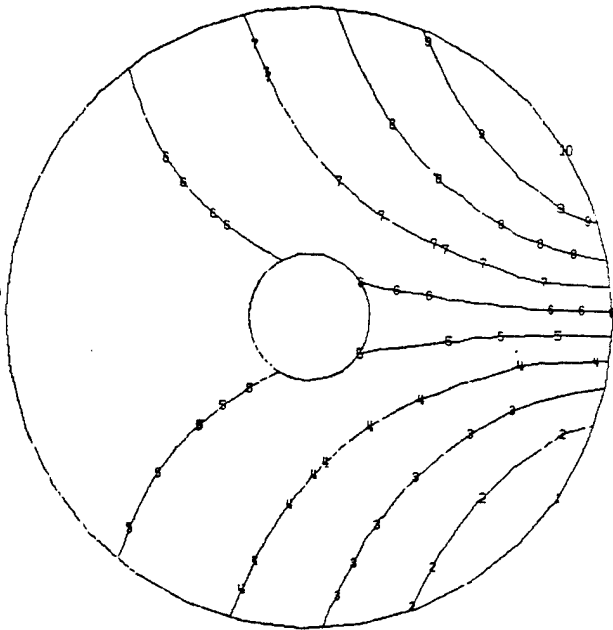
Fig. 5.9. System Model with Thick Lightweight Mirror, 80-cm Actuators.

Max-Def = 5.61×10^{-13}
 Min-Def = -7.13×10^{-14}



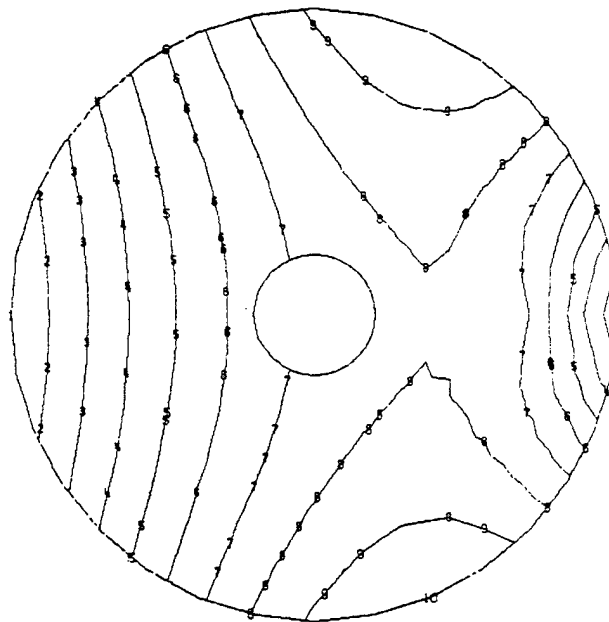
(a) Normal Position Control

Max-Def = 2.55×10^{-10}
 Min-Def = -2.55×10^{-10}



(b) Tangential Slope Control

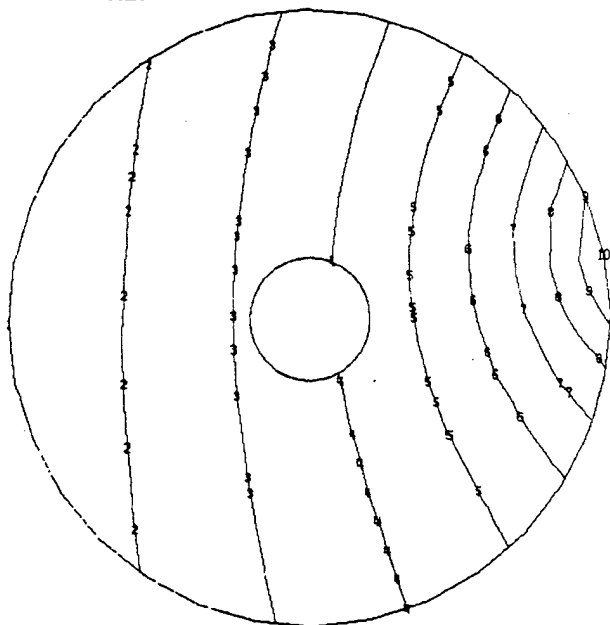
Max-Def = 1.30×10^{-10}
 Min-Def = -3.60×10^{-11}



(c) Radial Slope Control

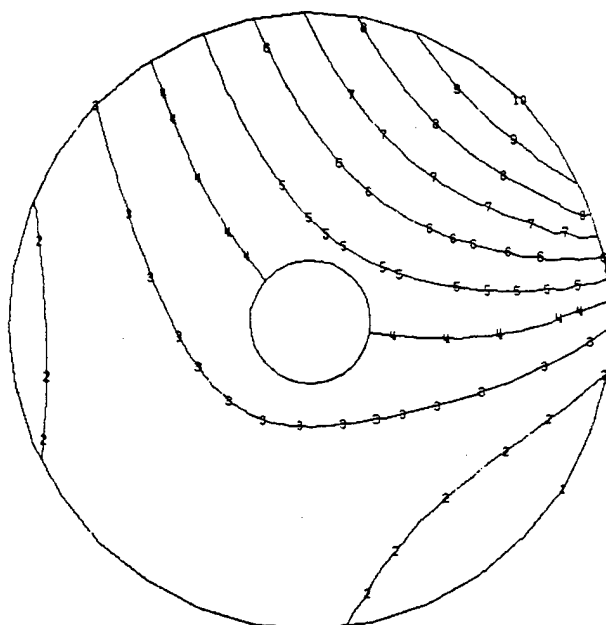
Fig. 5.10. System Model with Thick Lightweight Mirror, 160-cm Actuators.

Max-Def = 9.71×10^{-13}
 Min-Def = -8.14×10^{-14}



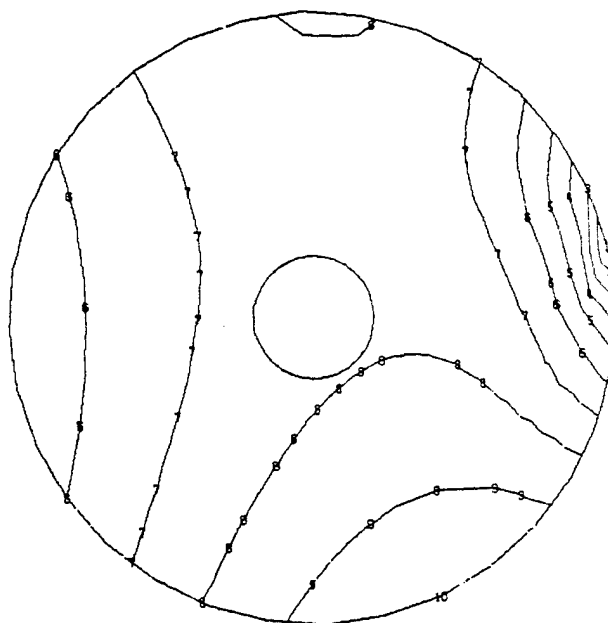
(a) Normal Position Control

Max-Def = 2.73×10^{-10}
 Min-Def = -5.62×10^{-11}



(b) Tangential Slope Control

Max-Def = 1.83×10^{-10}
 Min-Def = -2.33×10^{-10}



(c) Radial Slope Control

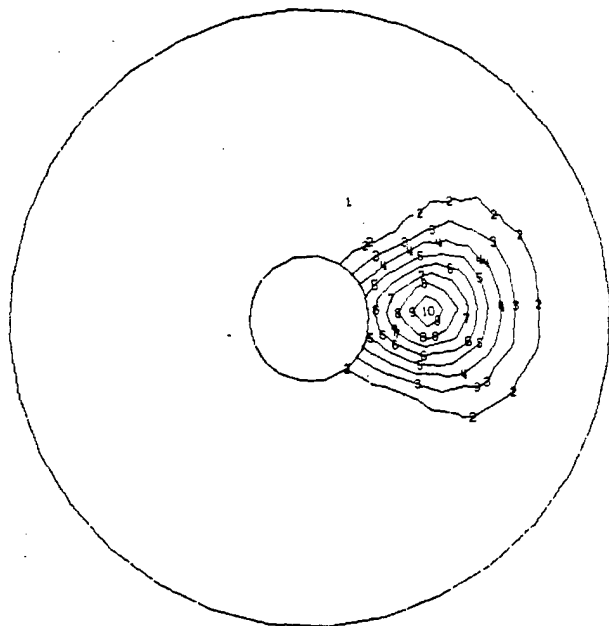
Fig. 5.11. System Model with Thick Lightweight Mirror, 200-cm Actuators.

require pretensioning. This greatly simplifies the initial system assembly.

For the system with a solid mirror and a nominal reference plate, contour plots are shown in Fig. 5.12-15. For the usual nine controls, deflections are adequately localized, all except for radial slope control of the 160 cm actuator, where the three point kinematic mount at the reference plate is reflected in the mirror figure. For all the other eight controls, contour plots for the 40-actuator system are nearly as localized as for the mirror model analysis with a "perfectly rigid" support structure, depicted in Figs. 4.2-4.4. This remarkable circumstance is a testimony to the concept of an integrated active mirror system. To provide a measure of the localization of deflection, consider the three instances of normal position control. The maximum mirror displacement at any non-controlled actuator is less than 3.1% of the mirror displacement of a controlled actuator. In addition to the usual nine controls, plots are included for the actuator with cylindrical coordinates $R = 160$ cm and $\theta = 22.5^\circ$. The contour plot of radial slope control for that actuator is satisfactory. This proves that the problem with the other 160 cm actuator is due to an interaction with the three point mount.

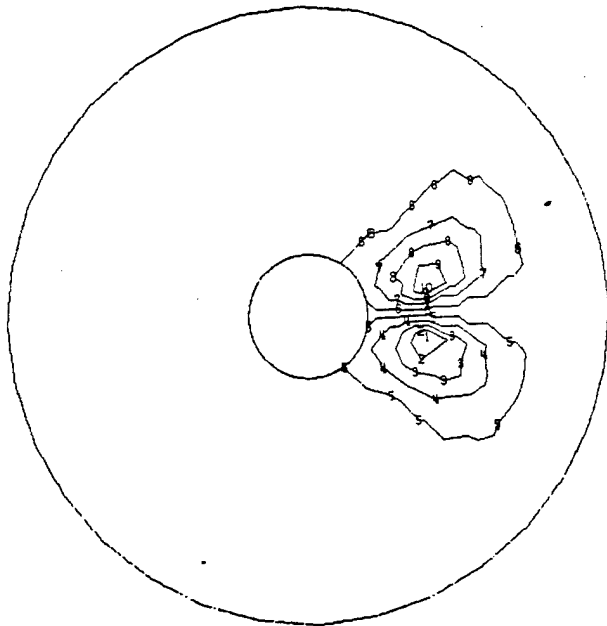
The next set of contour plots, Fig. 5.16-5.18, is for the system with a solid mirror and a small reference plate. The reduction in reference plate size was examined in Chapter 3 for a 2-dimensional model, where the reference plate weight was reduced 65% with no detrimental effects. To be conservative the weight for the 3-dimensional model was

Max-Def = 6.99×10^{-6}
 Min-Def = -3.44×10^{-7}



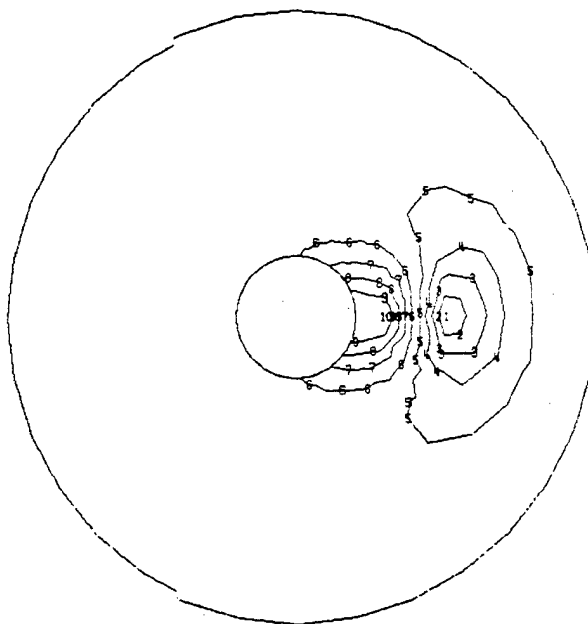
(a) Normal Position Control

Max-Def = 3.96×10^{-7}
 Min-Def = -3.96×10^{-7}



(b) Tangential Slope Control

Max-Def = 6.04×10^{-7}
 Min-Def = -5.45×10^{-7}

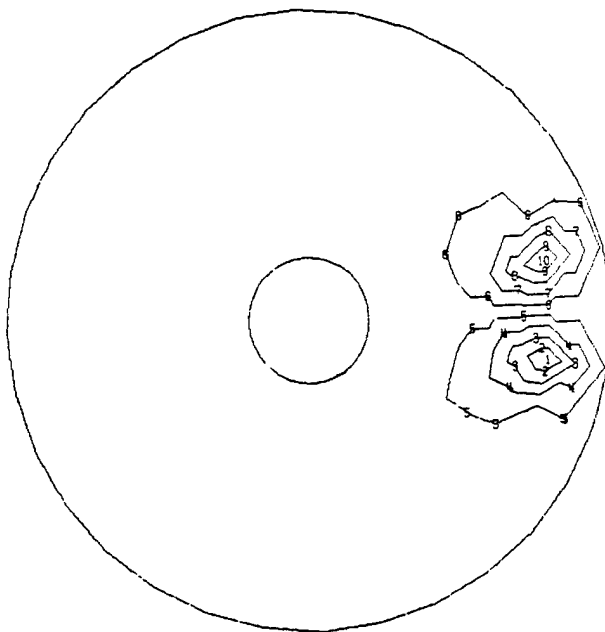
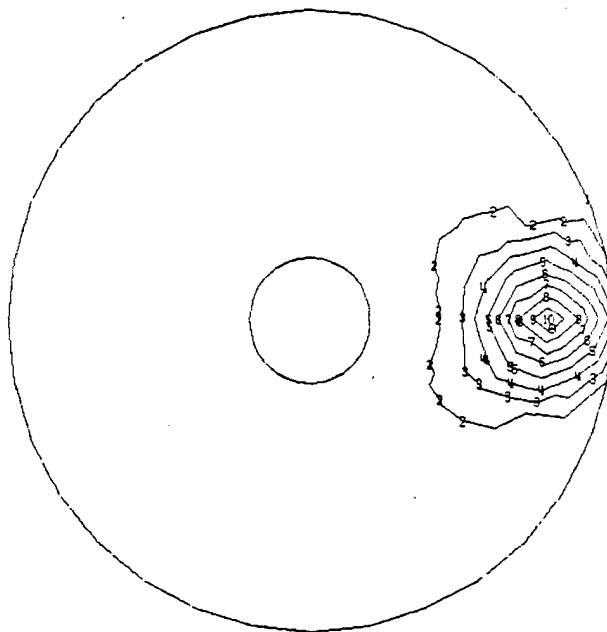


(c) Radial Slope Control

Fig. 5.12. System Model with Solid Mirror and Nominal Reference Plate, 80-cm Actuators.

Max-Def = 8.11×10^{-6}
 Min-Def = -8.58×10^{-7}

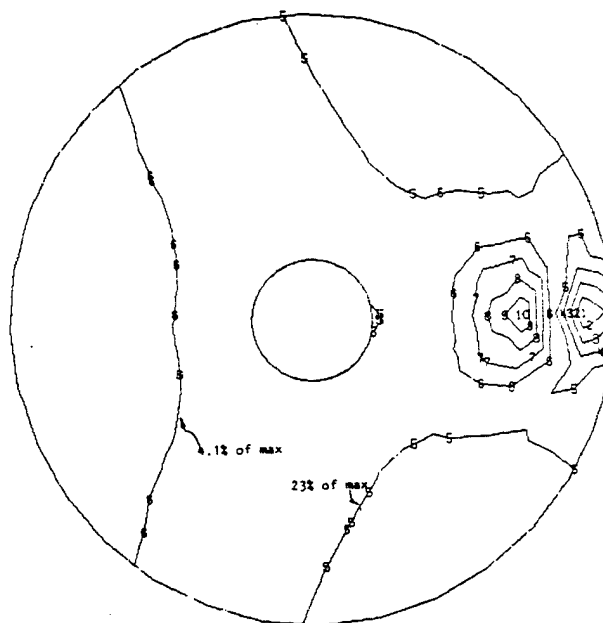
Max-Def = 2.83×10^{-7}
 Min-Def = -2.83×10^{-7}



(a) Normal Position Control

(b) Tangential Slope Control

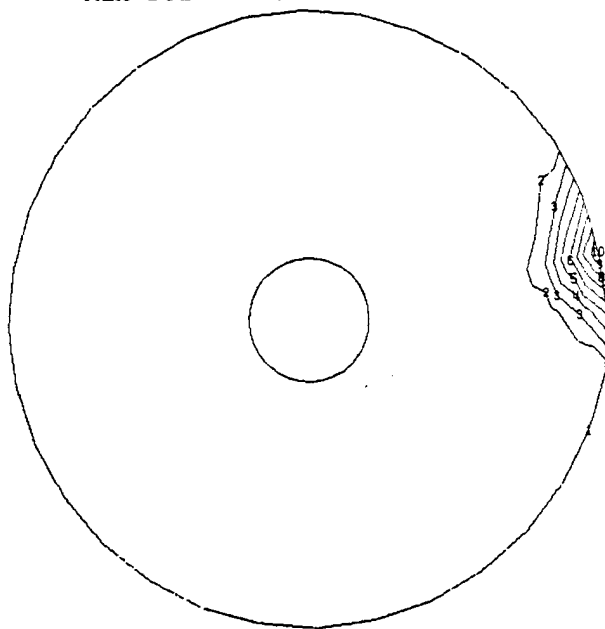
Max-Def = 3.38×10^{-7}
 Min-Def = -4.64×10^{-7}



(c) Radial Slope Control

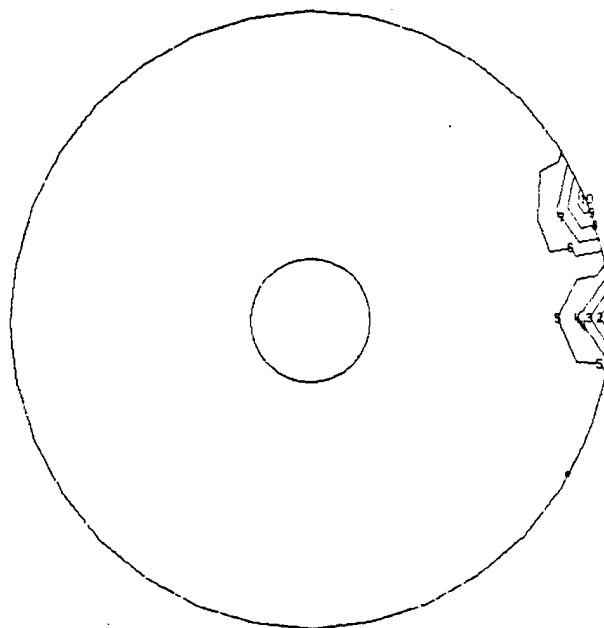
Fig. 5.13. System Model with Solid Mirror and Nominal Reference Plate, 160-cm Actuators.

Max-Def = 9.88×10^{-6}
 Min-Def = -2.62×10^{-7}



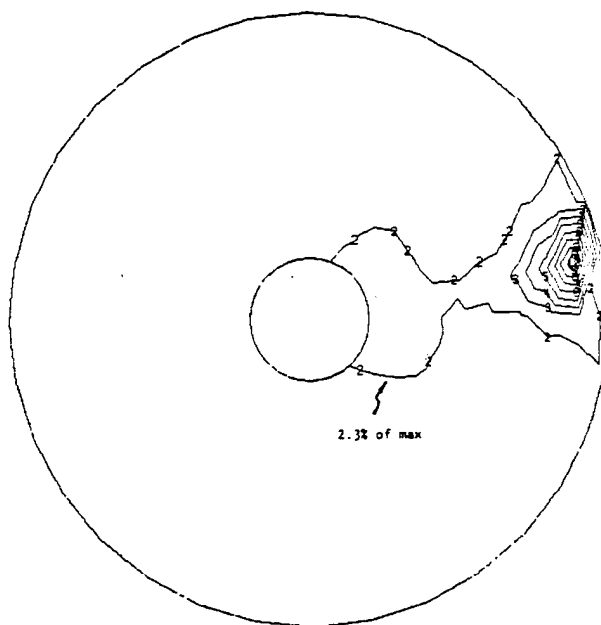
(a) Normal Position Control

Max-Def = 6.25×10^{-7}
 Min-Def = -6.06×10^{-7}



(b) Tangential Slope Control

Max-Def = 3.34×10^{-7}
 Min-Def = -3.32×10^{-8}

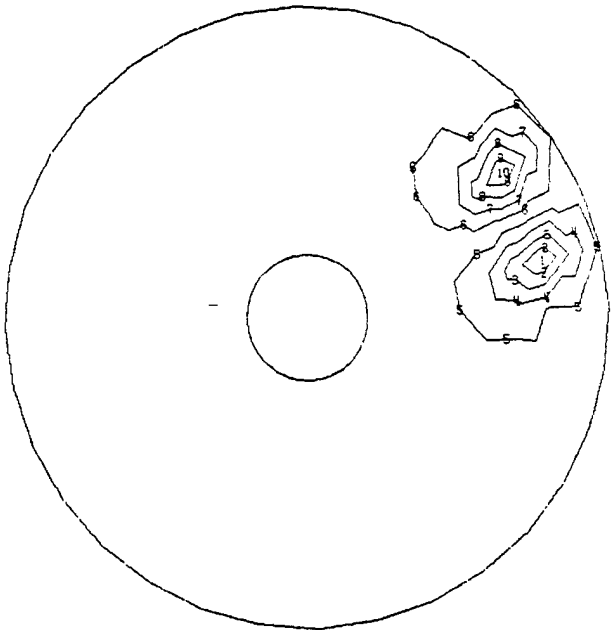
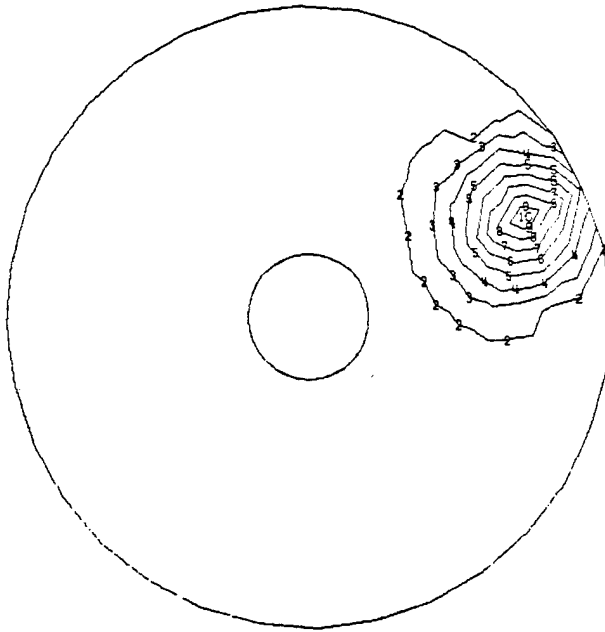


(c) Radial Slope Control

Fig. 5.14. System Model with Solid Mirror and Nominal Reference Plate, 200-cm Actuators.

Max-Def = 8.24
Min-Def = -7.44×10^{-1}

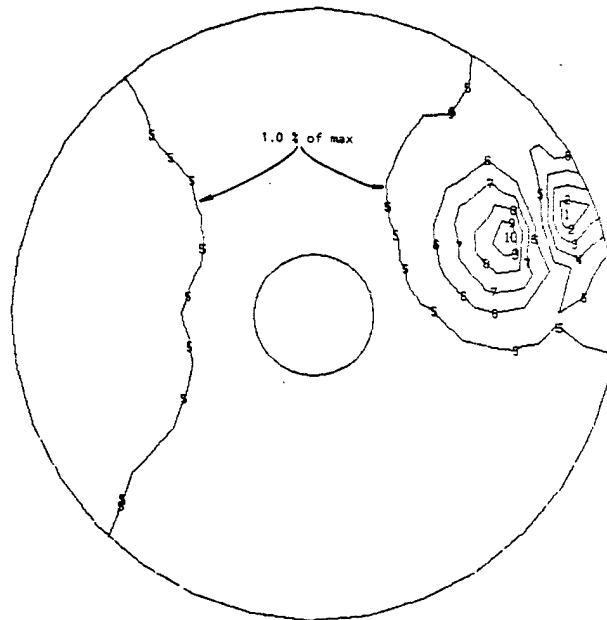
Max-Def = 3.00×10^{-1}
Min-Def = -2.65×10^{-1}



(a) Normal Position Control

(b) Tangential Slope Control

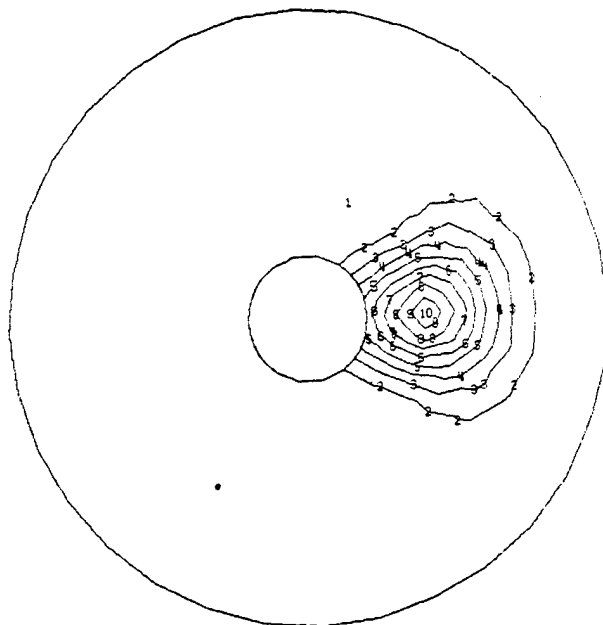
Max-Def = 4.48×10^{-1}
Min-Def = -3.67×10^{-1}



(c) Radial Slope Control

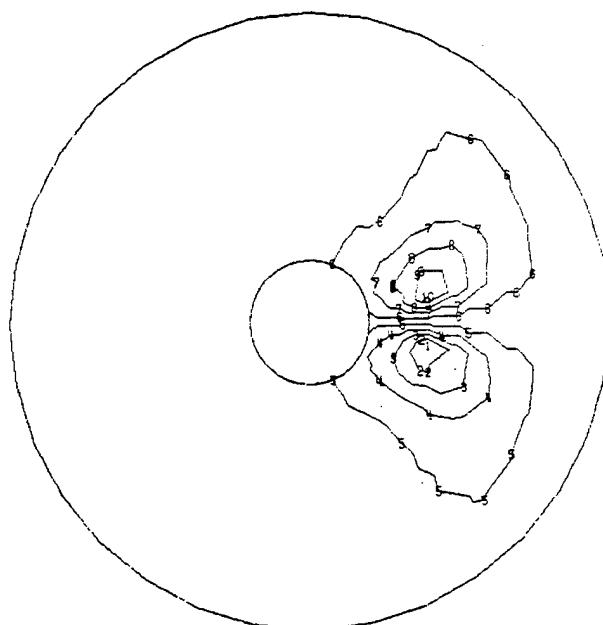
Fig. 5.15. System Model with Solid Mirror and Nominal Reference Plate, 160-cm Actuators ($\theta = 22.5^\circ$).

Max-Def = 6.79×10^{-6}
 Min-Def = -3.24×10^{-7}



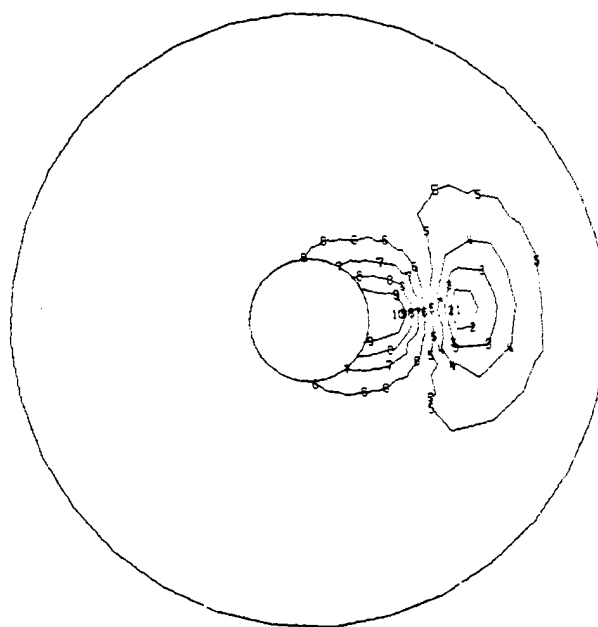
(a) Normal Position Control

Max-Def = 3.99×10^{-7}
 Min-Def = -3.99×10^{-7}



(b) Tangential Slope Control

Max-Def = 5.92×10^{-7}
 Min-Def = -5.58×10^{-7}

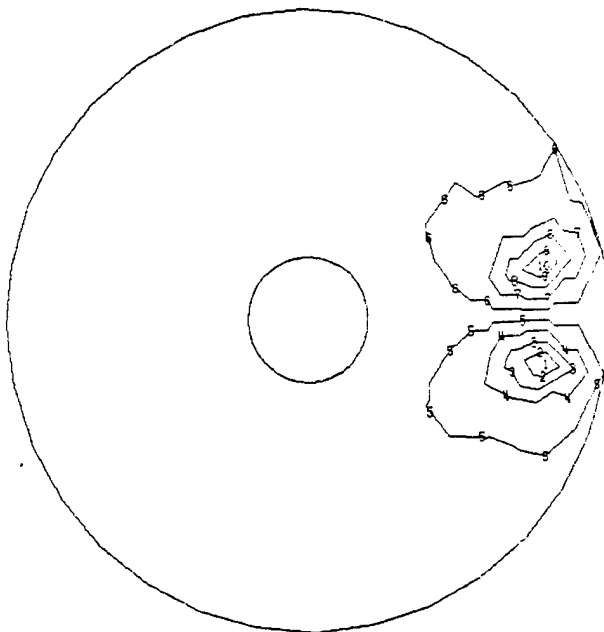
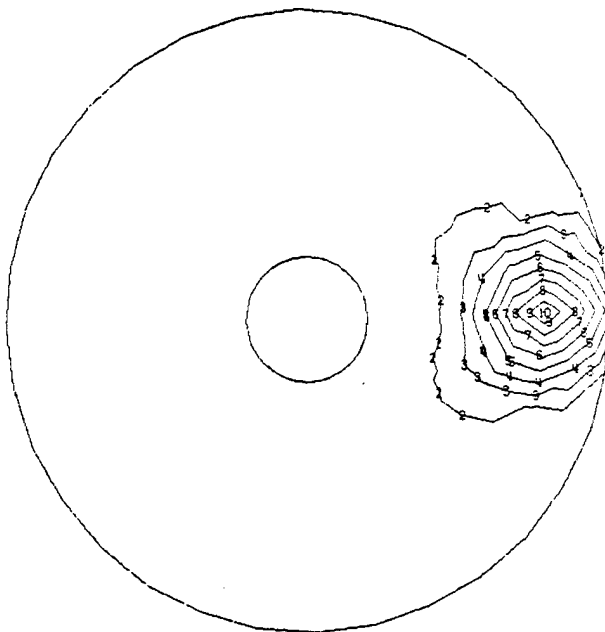


(c) Radial Slope Control

Fig. 5.16. System Model with Solid Mirror and Small Reference Plate, 80-cm Actuators.

Max-Def = 7.95×10^{-6}
 Min-Def = -8.00×10^{-7}

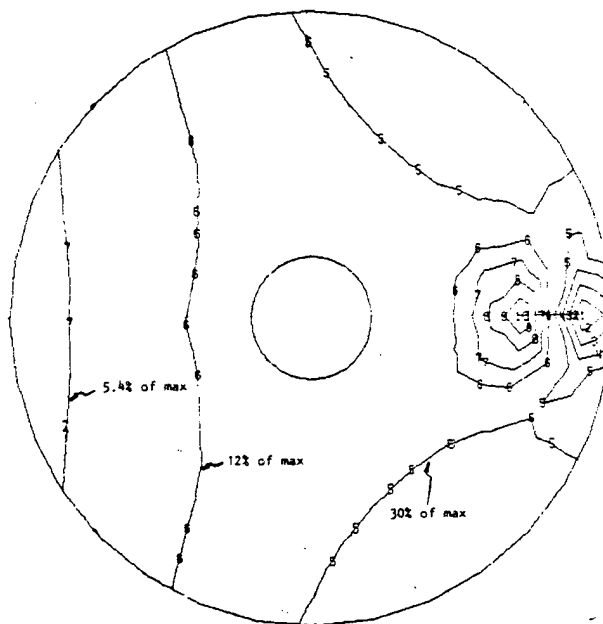
Max-Def = 2.91×10^{-7}
 Min-Def = -2.91×10^{-7}



(a) Normal Position Control

(b) Tangential Slope Control

Max-Def = 2.89×10^{-7}
 Min-Def = -4.98×10^{-7}

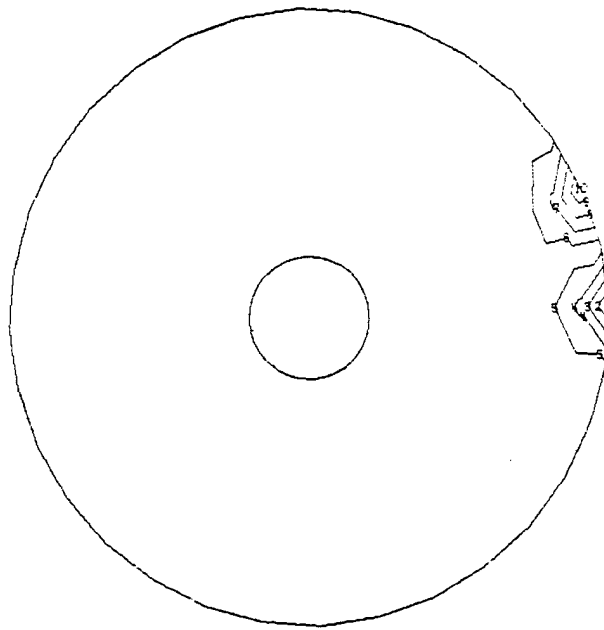
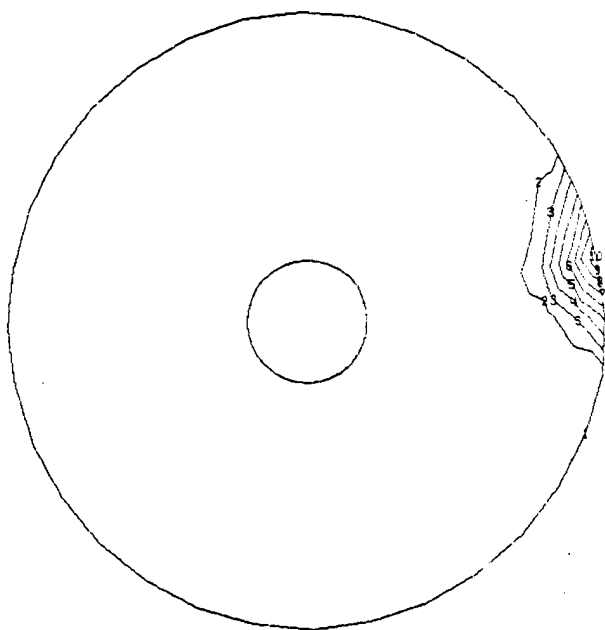


(c) Radial Slope Control

Fig. 5.17. System Model with Solid Mirror and Small Reference Plate, 160-cm Actuators.

Max-Def = 9.89×10^{-6}
 Min-Def = -3.42×10^{-7}

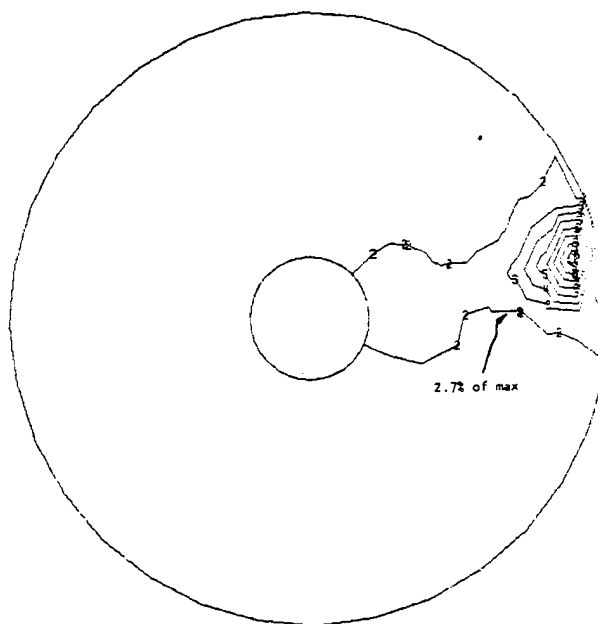
Max-Def = 6.41×10^{-7}
 Min-Def = -6.05×10^{-7}



(a) Normal Position Control

(b) Tangential Slope Control

Max-Def = 3.36×10^{-7}
 Min-Def = -3.17×10^{-8}



(c) Radial Slope Control

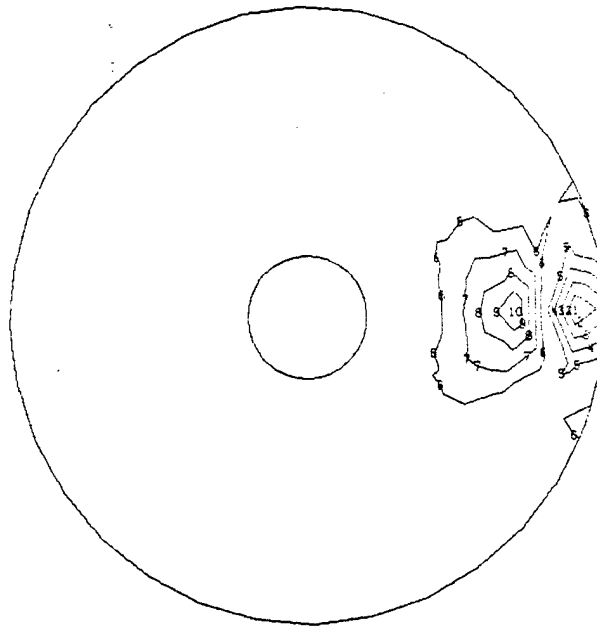
Fig. 5.18. System Model with Solid Mirror and Small Reference Plate, 200-cm Actuators.

reduced only 50%. Comparing results for the small reference plate system to the nominal reference plate system, the nominal position control is almost identical, tangential slope control is in general not quite as localized, and the problem with radial slope control of the 160 cm actuator is further aggravated. Again, to measure localization of deflection, consider the three normal position controls. The maximum mirror displacement at any non-controlled actuator is now less than 4.5% of the mirror displacement of a controlled actuator.

The final contour plots here are for the same solid mirror and small reference plate, but this time with a flexural mount instead of a kinematic mount. Only two contour plots were noticeably different from the previous set incorporating the kinematic mount. The first plot, Fig. 5.19(a), shows a noticeable improvement. Print through of the three point kinematic mount has all but been eliminated by changing to a mount with 16 individual flexures. The second, Fig. 5.19(b), is much worse than its counterpart. The problem of interaction with the kinematic mount has now become a problem of interaction with the flexures.

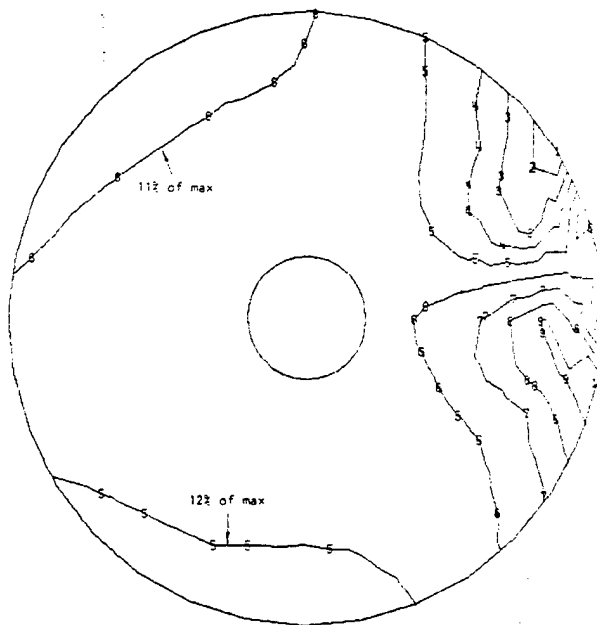
Unfortunately, due to time constraints, the thin lightweight mirror was never analyzed in this 40-actuator system. Results for that mirror should be better than for the solid mirror, since the bending stiffness of the solid mirror is 12% greater than for the sandwich mirror, even neglecting shear deformation. In a previous study (Shannon, Richard, and Hansen, 1980) both the solid mirror and the thin lightweight mirror were analyzed in a 40-actuator system without sliders and with a three point kinematic mount, a nominal reference plate and a different

Max-Def = 3.83×10^{-7}
 Min-Def = -4.17×10^{-7}



(a) 160 cm Actuator Radial Slope Control

Max-Def = 5.11×10^{-7}
 Min-Def = -5.16×10^{-7}



(b) 200 cm Actuator Tangential Slope Control

Fig. 5.19. System Model with Solid Mirror, Small Reference Plate, and Flexure Mount. Two Slope Controls.

method of applying loads to simulate the individual controls. Contour plots of normal position and slope controls for both mirror systems reveal adequate localization of deflection in the vicinity of the active actuator for all of the nine basic controls.

It is conceivable that the contour plots in this chapter for which deflections are not as localized as desired, and which all occur for in-plane slope control, are a product of the method of load introduction. Therefore, for follow-on studies, it is recommended that slope controls be imparted by the method of Case 11 in Fig. 3.6, where a couple is applied to the actuator post with no reaction at the reference plate.

Actuator Force Determination

For all the remaining analyses determination of actuator forces is a complicated process. The first step in this process is to obtain deflections to be applied to actuator degrees of freedom. For the gravity and thermal loads, it was assumed that optical deflection measurements of both position and slope would be made at the actuator attachment points on the mirror surface and the control system would null these deflections. Thus actuator deflections are the negative of the deflections from an analysis of the loaded system model. For defocus and astigmatism, the mirror deflections are the same as were used for the mirror model in Chapter 4.

Now the actuator forces, f_j , that cause the aforementioned deflections, x_i , are obtained with the matrix equation

$$\{x\} = [F]\{f\}$$

where:

x_i is the i^{th} displacement of the mirror surface, either a translation or a rotation,

f_j is the j^{th} temperature, either of a slider (normal position control), a pair of reference plate elements (in-plane slope control), or a dummy rod (out-of-plane slope control),

and F_{ij} is the i^{th} displacement due to a unit j^{th} temperature.

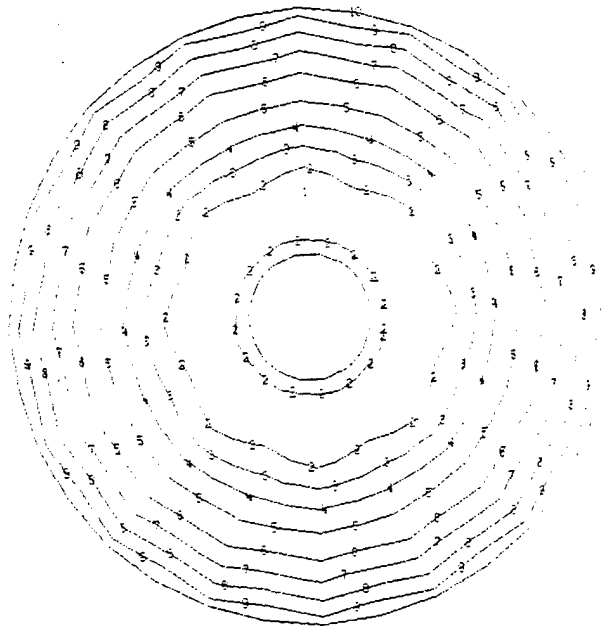
Influence coefficient matrices $[F]$, for normal position control (40x40) and for normal position and slope controls (120x120), are assembled by applying individual unit temperature loads. The appropriate actuator displacements for each load form a column in $[F]$. The IMSL Library (IMSL, Inc., 1979) subroutine LEQT2F solved the systems of 40 and 120 simultaneous equations for $\{f\}$.

To accomplish an analysis, the actuator forces are superimposed with the driving loads.

Defocus and Astigmatism

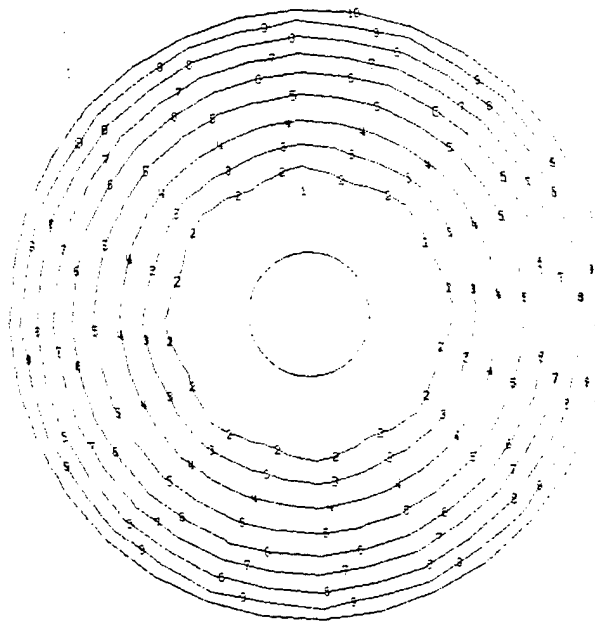
For the system with the solid mirror and the small reference plate, contour plots of defocus are in Fig. 5.20. Contour line flattening is slightly more predominant here than in Fig. 4.11, the contour plots for analysis of the corresponding mirror model. Radial cross-section deflections

Max-Def = 1.82×10^{-9}
Min-Def = -2.13×10^{-4}



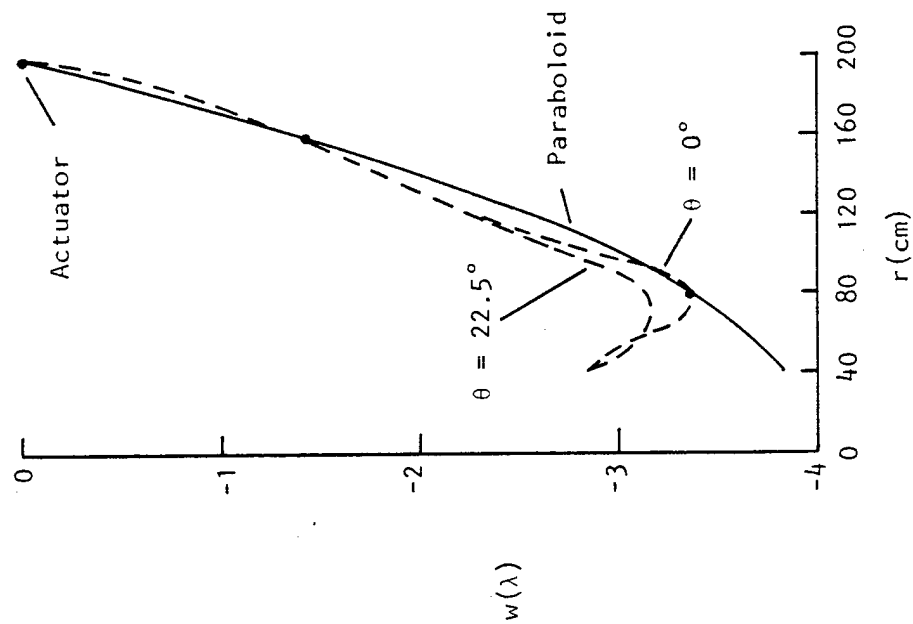
(a) Normal Position Control

Max-Def = 1.82×10^{-9}
Min-Def = -2.13×10^{-4}

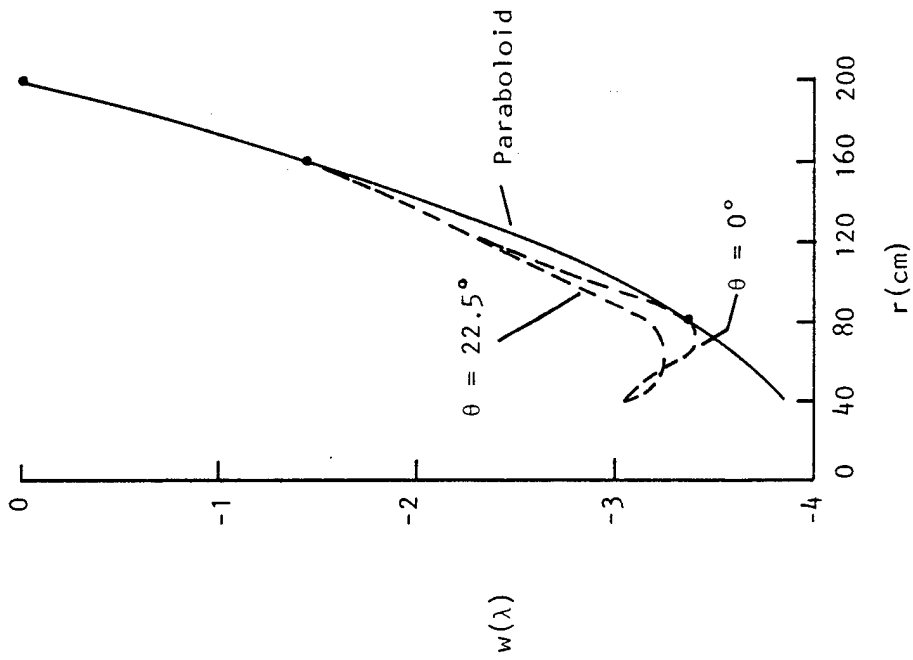


(b) Normal Position and Slope Controls

Fig. 5.20. System Model with Solid Mirror and Small Reference Plate, Defocus.



(a) Normal Position Control



(b) Normal Position and Slope Controls

Fig. 5.21. System Model with Solid Mirror and Small Reference Plate. Cross Sections for Defocus.

for the system model, Fig. 5.21, compare favorably with Fig. 4.14 for the mirror model. Rms values of residual wavefront variations after a defocussed reference surface is removed are in Table 5.2. The lack of actuators at the inner edge of the mirror creates large errors beyond the existing inner ring of actuators, and cannot effectively be eliminated by masking. Scalloping at the outer edge of the mirror has been substantially reduced by the outer two rings of actuators. Since the mirror's ratio of bending stiffness to membrane stiffness is low, the addition of slope control to position control is ineffective. To accurately defocus the mirror, either actuators need be included at the inner edge, or the mirror must be lightweighted. Using a thicker solid mirror would help, but the weight penalty would be too great.

Contour plots for astigmatism are in Fig. 5.22, and rms values in Table 5.2. Again results for the system model mimic these of the mirror model but are slightly less accurate. For astigmatism actuators are not necessary at the inner edge of the mirror. Masking is not productive, but slope control in concert with normal position control is effective in reducing errors by about a factor of 20 as compared to the normal position control alone.

Two conclusions surface from these analyses. It is much easier to deform a mirror into a developable shape, i.e. one in which the middle surface of the mirror is unstretched, such as astigmatism, than it is to deform it into a nondevelopable shape, e.g. defocus. Slope controls are very effective in forming nondevelopable surfaces but not for developable surfaces.

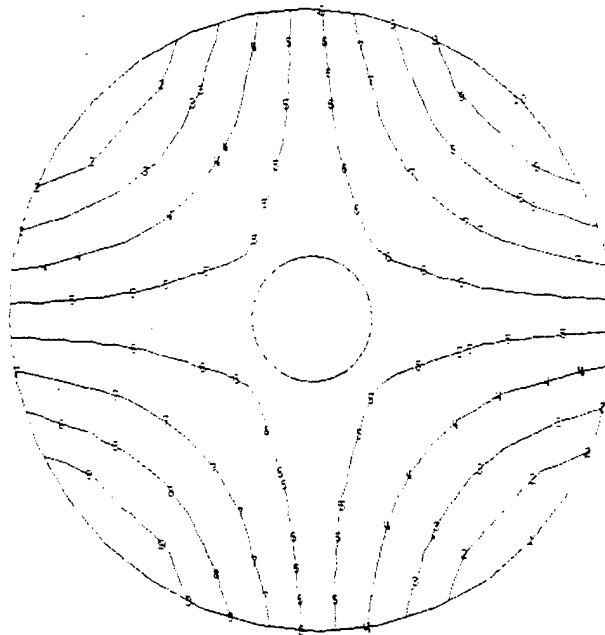
Table 5.2. Residual Wavefront Variations for Defocus and Astigmatism for System Model with Solid Mirror and Small Reference Plate.

Aberration	Magnitude of Desired Aberration (λ)	Residual after Normal Actuation			Residual after Normal and Slope Actuation		
		rms (λ)	Span (λ)	Error Ratio(%)	rms (λ)	Span (λ)	Error Ratio (%)
Defocus	3.84	.116	.853	22.	.0908	.682	18.
	3.36	.0949	.471	14.	.0565	.351	10.
Astigmatism	4.	.0114	.0968	2.4	.0006	.0053	.13
	4.	.0116	.0925	2.3	.0006	.0054	.13

Note: (1) Upper numbers use wavefront from entire mirror and lower numbers use wavefront from masking section of mirror within inner ring of actuators.

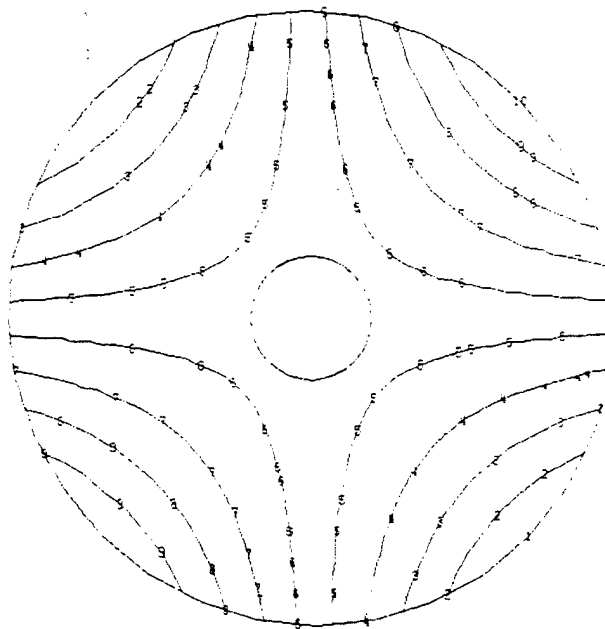
(2) Error Ratio = $\frac{\text{Span of error after actuation}}{\text{Magnitude of desired aberration}}$

Max-Def = 1.20×10^{-4}
Min-Def = -1.20×10^{-4}



(a) Normal Position Control

Max-Def = 1.26×10^{-4}
Min-Def = -1.26×10^{-4}



(b) Normal Position and Slope Controls

Fig. 5.22. System Model with Solid Mirror and Small Reference Plate, Astigmatism.

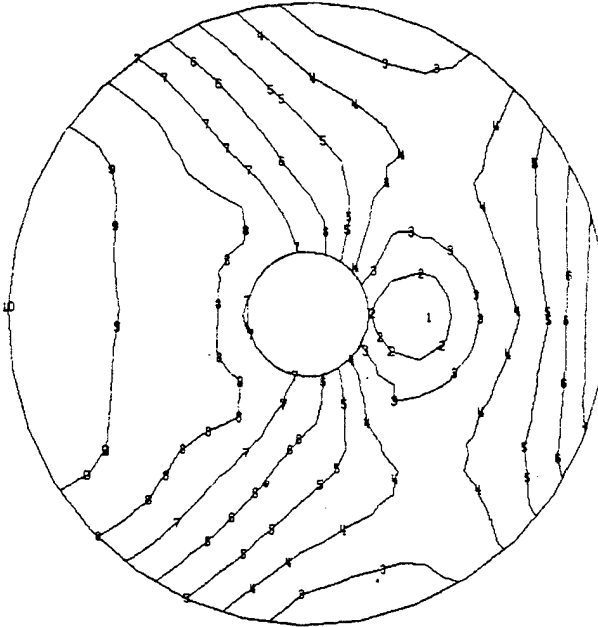
Gravity Loads

Gravity loads of 1g magnitude were applied in the x, y and z coordinate directions in separate analyses. These loads predict the difficulty of obtaining diffraction limited performance both in the 1g earth environment of a test laboratory and in a 0g space environment. Loads were applied parallel to and normal to the mirror in an attempt to find a desirable orientation. Since the kinematic mount does not provide equal reactions at the three support points, the x and y gravity loads yield different mirror figures.

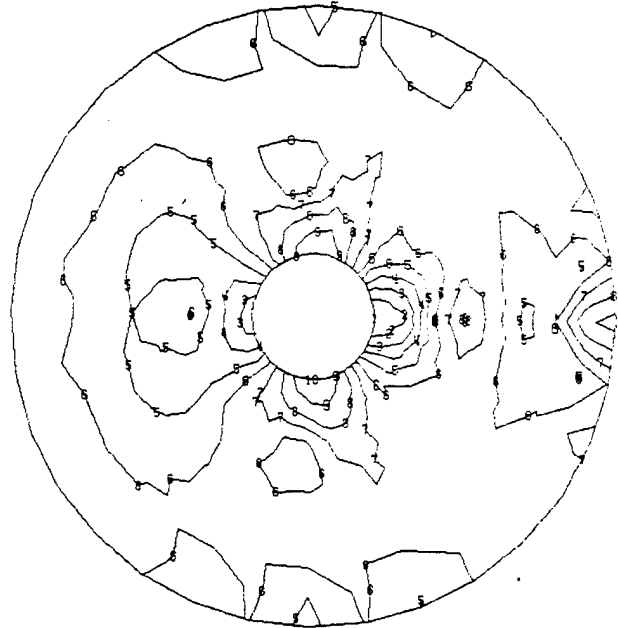
Fig. 5.23-5.25 are contour plots for the three gravity loads. Each set of plots for a particular gravity load includes a plot with no actuator control, one for actuator normal position control and one for both normal position and slope controls. The symmetry patterns for the plots corresponding to no actuator control reflect the action of the three point mount. The z gravity load plots should be compared to Fig. 4.17(b), which is the deflection of the mirror with "perfectly rigid" supports under the same load. Before correction the system model plot looks nothing like the mirror model plot, but after correction the resemblance is striking. This substantiates the premise that inter-actuator sag due to gravity is not controllable. Fig. 5.26 has deflections of radial cross-sections due to the z gravity load. It is evident that slope control can do little more than normal position control in reducing deformation. Table 5.3 summarizes results of FRINGE. For gravity loads error ratios vary around 10%. Errors are not reduced significantly by either masking or by addition of slope

Max-Def. 7.94×10^{-4}
 Min-Def. -3.96×10^{-3}

Max-Def. $= 3.71 \times 10^{-4}$
 Min-Def. $= -4.75 \times 10^{-4}$

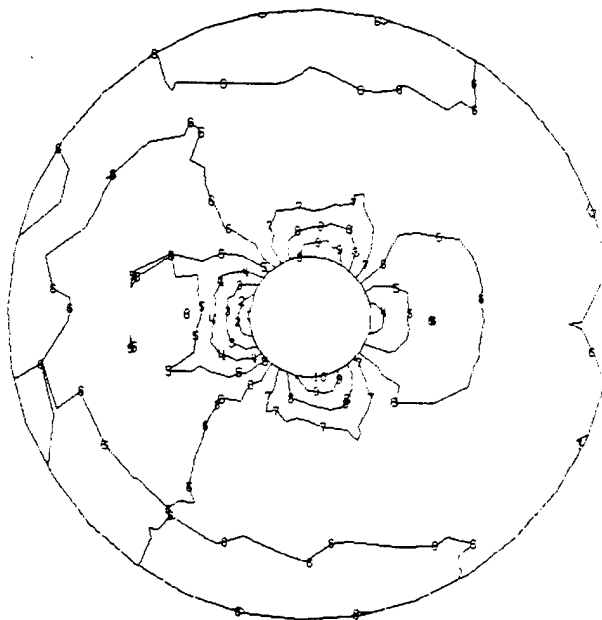


(a) No Actuator Control



(b) Normal Position Control

Max-Def. $= 2.94 \times 10^{-4}$
 Min-Def. $= -3.71 \times 10^{-4}$

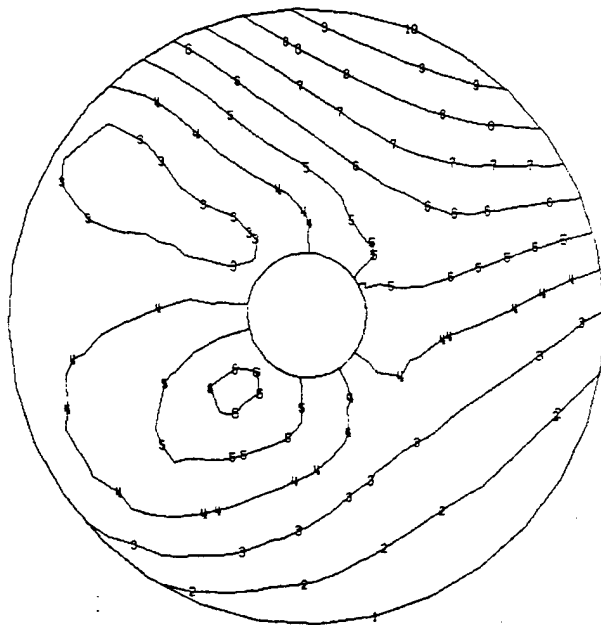


(c) Normal Position and Slope Controls

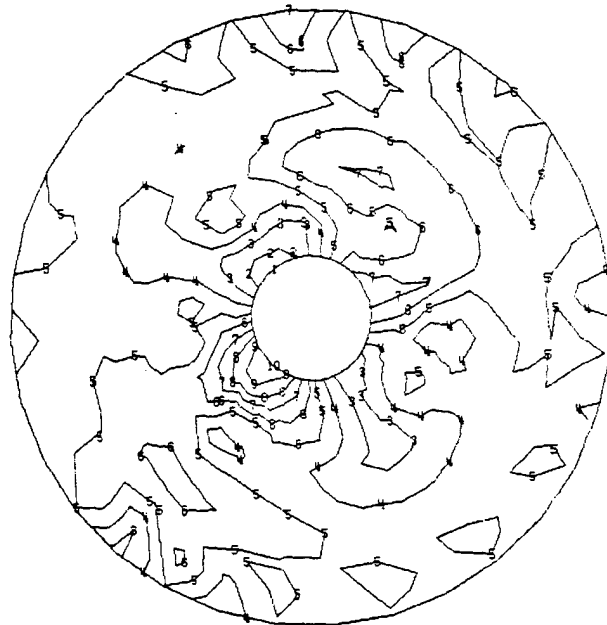
Fig. 5.23 System Model with Solid Mirror and Small Reference Plate,
 x Gravity Load of 1g

Max-Def. = 5.33×10^{-3}
 Min-Def. = -1.39×10^{-3}

Max-Def. = 4.00×10^{-4}
 Min-Def. = -3.08×10^{-4}

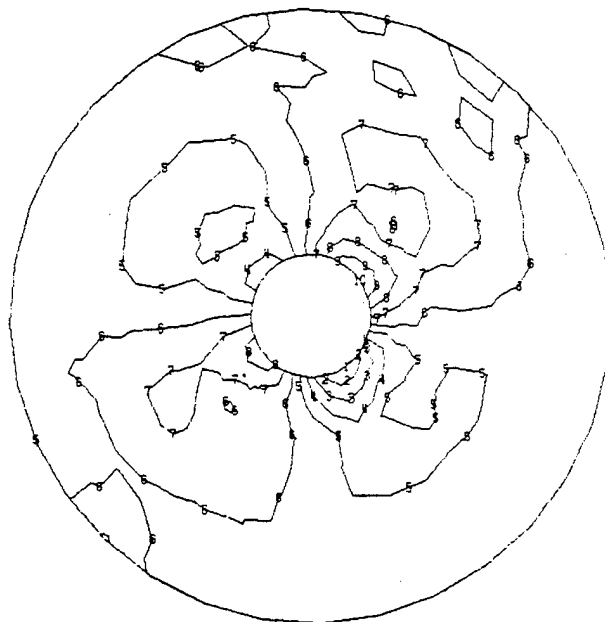


(a) No Actuator Control



(b) Normal Position Control

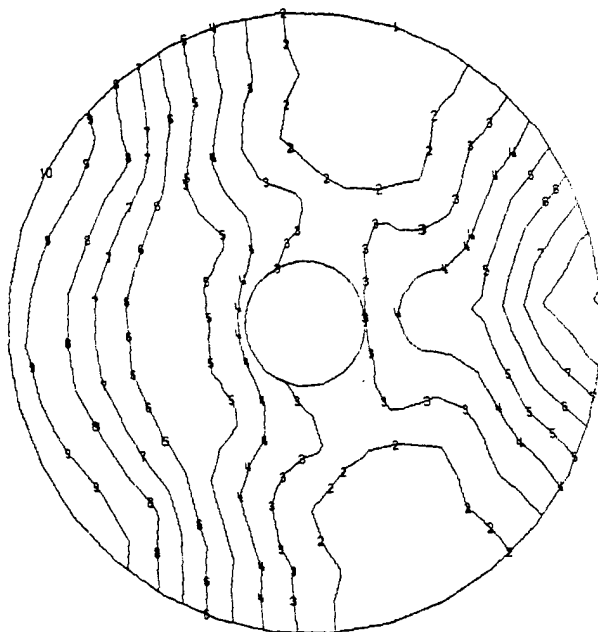
Max-Def. = 2.67×10^{-4}
 Min-Def. = -3.12×10^{-4}



(c) Normal Position and Slope Controls

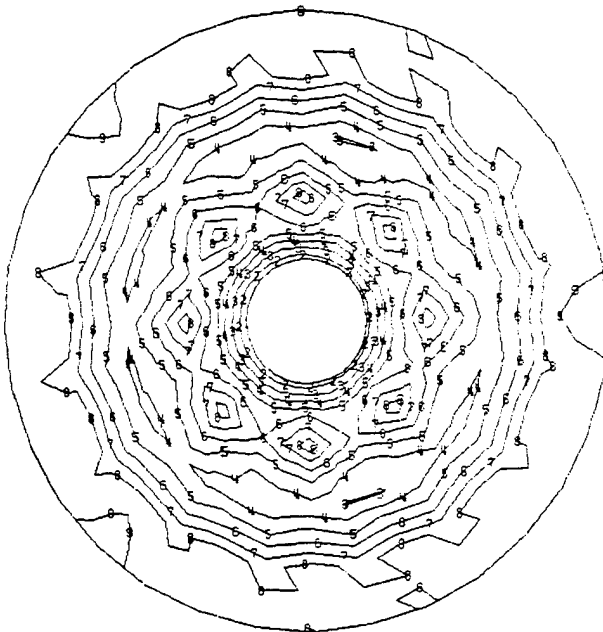
Fig. 5.24 System Model with Solid Mirror and Small Reference Plate,
 y Gravity Load of $1g$

Max-Def. = -4.56×10^{-4}
Min-Def. = -1.63×10^{-2}



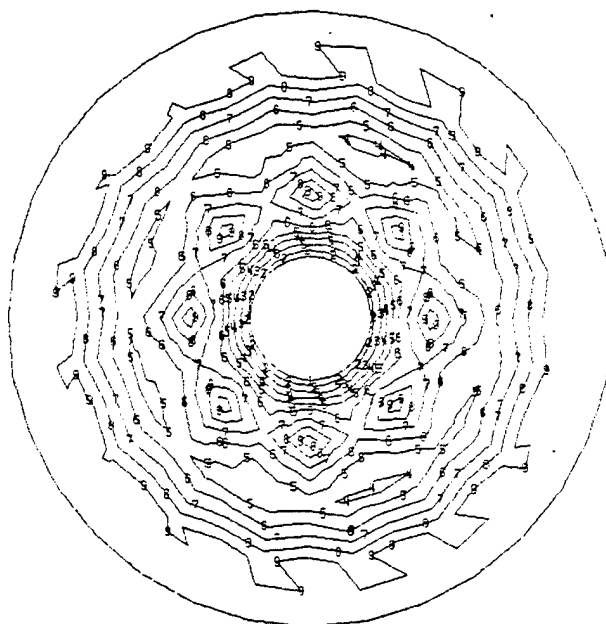
(a) No Actuator Control

Max-Def. = 5.12×10^{-4}
Min-Def. = -2.78×10^{-3}



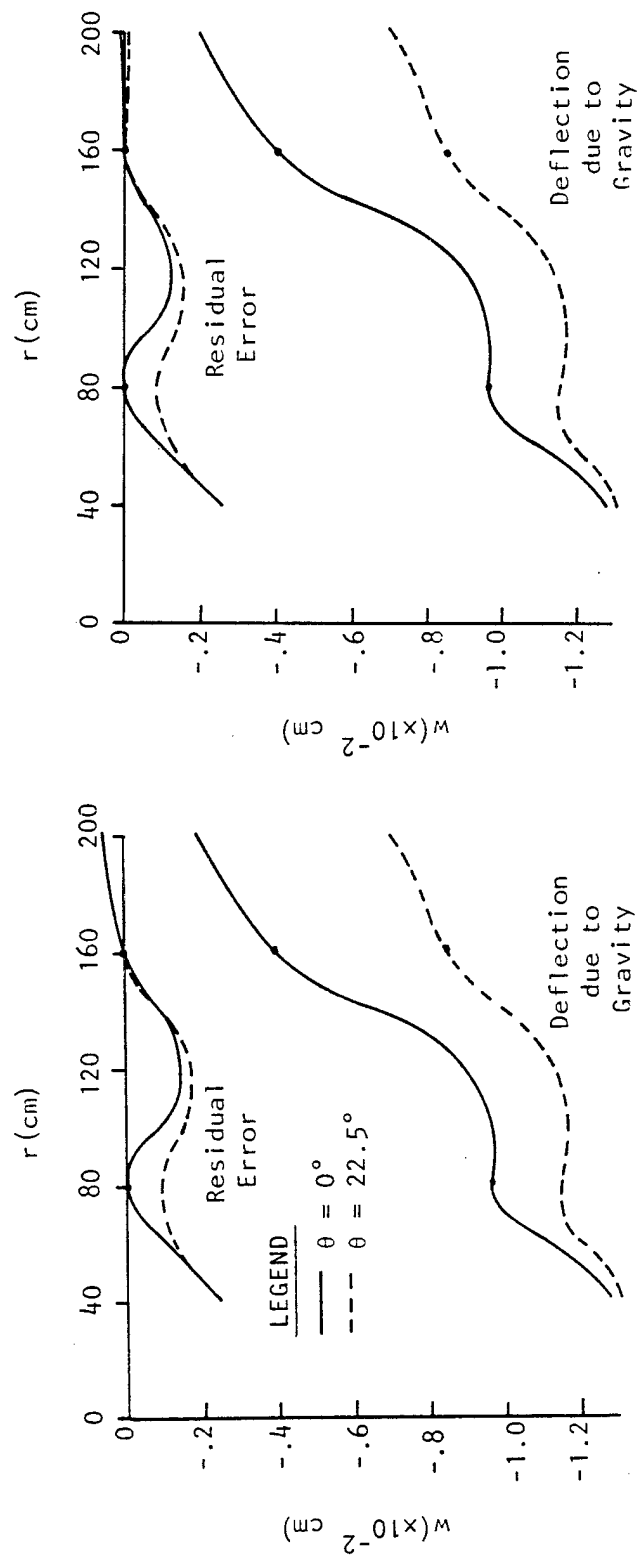
(b) Normal Position Control

Max-Def. = 1.18×10^{-4}
Min-Def. = -2.80×10^{-3}



(c) Normal Position and Slope Controls

Fig. 5.25 System Model with Solid Mirror and Small Reference Plate,
z Gravity Load of 1g



(a) Normal Position Control

(b) Normal Position and Slope Controls

Fig. 5.26. System Model with Solid Mirror and Small Reference Plate, Cross Sections for z Gravity Load.

Table 5.3. Residual Wavefront Variations after Subtraction of Tilt and Defocus for System Model with Solid Mirror and Small Reference Plate.

Load	Residual for No Correction		Residual after Normal Correction			Residual after Normal and Slope Correction		
	rms (λ)	Span (λ)	rms (λ)	Span (λ)	Error Ratio (%)	rms (λ)	Span (λ)	Error Ratio (%)
x gravity of 1 g	11.1	65.7	1.15	11.5	10.	.716	8.66	6.5
	10.8	63.8	.694	5.63	6.4	.34	2.06	3.1
y gravity of 1 g	14.0	64.5	1.05	9.52	7.5	.766	7.68	5.5
	14.0	64.6	.791	4.80	5.7	.553	2.933	4.0
z gravity of 1 g	48.0	259.	6.39	38.4	13.	5.69	37.2	12.
	49.3	259.	6.76	37.6	14.	6.09	35.0	12.
Axial thermal gradient of 1° C	.020	.112	.017	.092	85.	.017	.092	85.
	.006	.039	.005	.034	83.	.004	.025	67.
Uniform thermal soak of 1° C	.021	.116	.007	.037	33.	<.0005	.003	<2.4
	.014	.088	.088	.032	44.	.001	.003	7.1

Note: (1) Upper numbers use wavefront from entire mirror and lower numbers use wavefront from masking section of mirror within inner ring of actuators.

(2) Error Ratio = $\frac{\text{rms error after correction}}{\text{rms error before correction}}$

control to normal position control. Even if the mirror were stood on edge for ground testing, the rms residual after control is about 1λ , compared to $\lambda/20$ for a diffraction limited system.

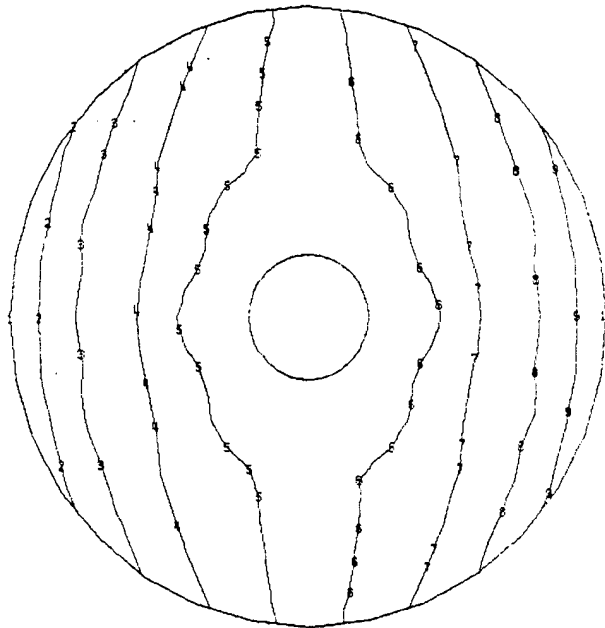
All previous results for gravity loads were for the solid mirror with a lightweight reference plate and a kinematic mount. By using the nominal reference plate with either the kinematic mount or a flexural mount, the reference plate is stiffened and print through from the mounts is drastically reduced.

Contour plots for the flexural mount are in Fig. 5.27. Due to symmetry, only two plots are necessary. FRINGE results for these systems with loads applied but with no controls are in Table 5.4. By increasing the size of the reference plate when using a kinematic mount, uncorrected deflection are reduced by factors of about 10, 3, and 3 for the three gravity loads. More importantly, when using the flexural mount, factors of reduction are 13, 17, and 18. Assuming a 10% error ratio, the rms error after correction for in-plane gravity loads would be .084, approaching the diffraction limited condition.

Thermal loads

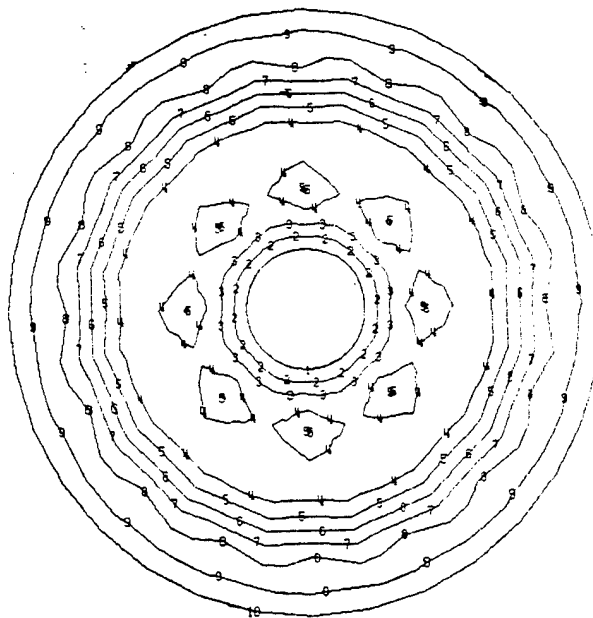
Two thermal loads were applied to the solid mirror with a small reference plate: a 1°C thermal gradient through the mirror, with the reflective surface at the highest temperature, and a 1°C uniform thermal soak of the entire 40-actuator system. Fig. 5.28 and 5.29 are corresponding sets of contour plots, with each set including plots both without and with controls. Figs. 5.30 and 5.31 are radial cross-section deflections.

Max-Def = 1.33×10^{-3}
 Min-Def = -1.33×10^{-3}



(a) x Gravity Load of 1 g

Max-Def = -2.17×10^{-3}
 Min-Def = -7.11×10^{-3}



(b) z Gravity Load of 1 g

Fig. 5.27. System Model with Solid Mirror, Nominal Reference Plate, and Flexure Mount; Gravity Loads.

Table 5.4. Residual Wavefront Variations after Subtraction of Tilt and Defocus for Two Different 40-Actuator Systems.

Load	40 Actuator System with Nominal Reference Plate and Kinematic Mount and with No Correction		40 Actuator System with Nominal Reference Plate and Flexural Mount and with No Correction	
	rms (λ)	Span (λ)	rms (λ)	Span (λ)
1 g x gravity	1.07	7.00	.843	5.57
1 g y gravity	4.59	21.2	.843	5.57
1 g z gravity	16.3	87.1	2.69	14.6
Axial thermal gradient of 1°C	----	----	.010	.056
Uniform thermal soak of 1°C	----	----	.011	.080

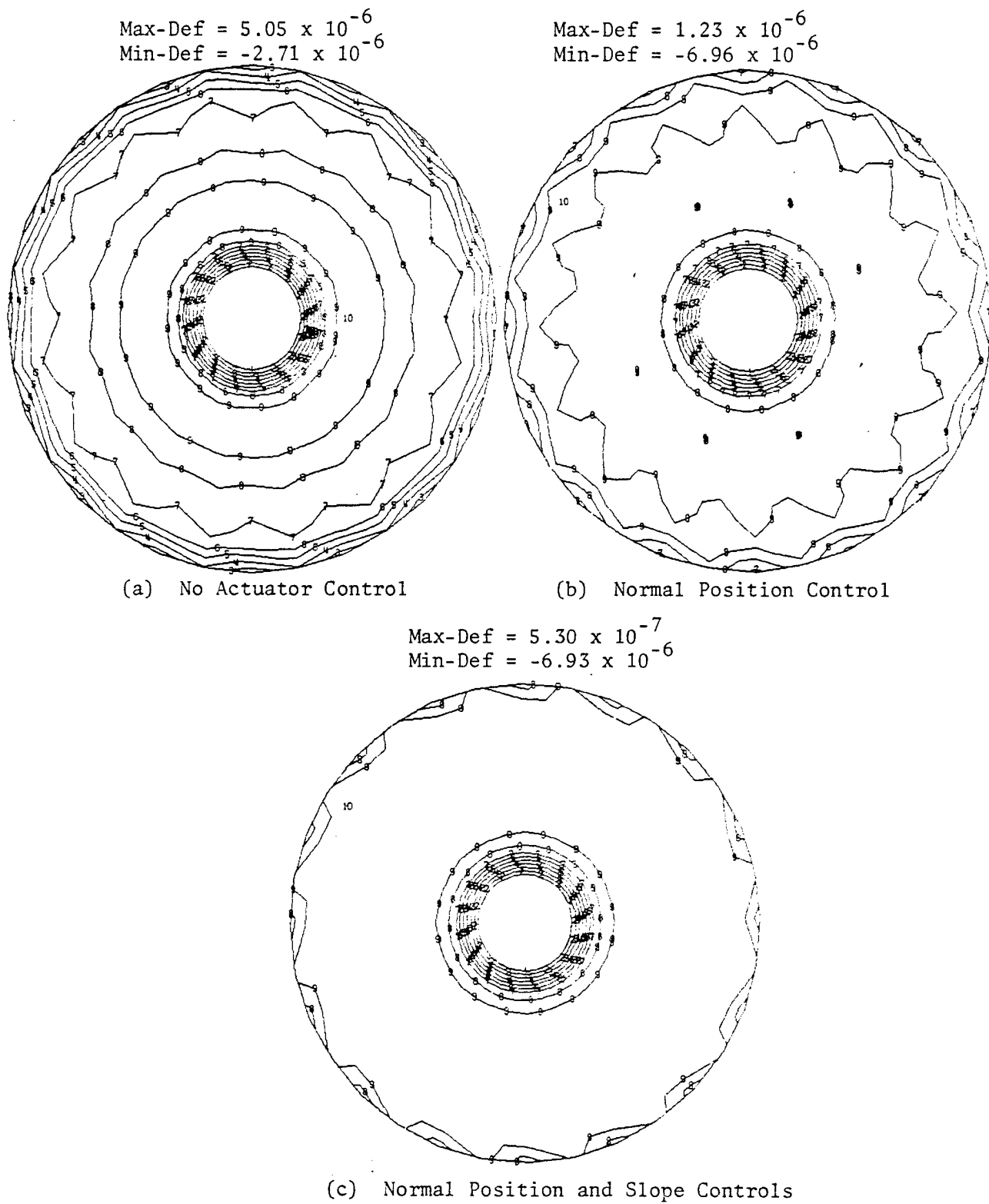
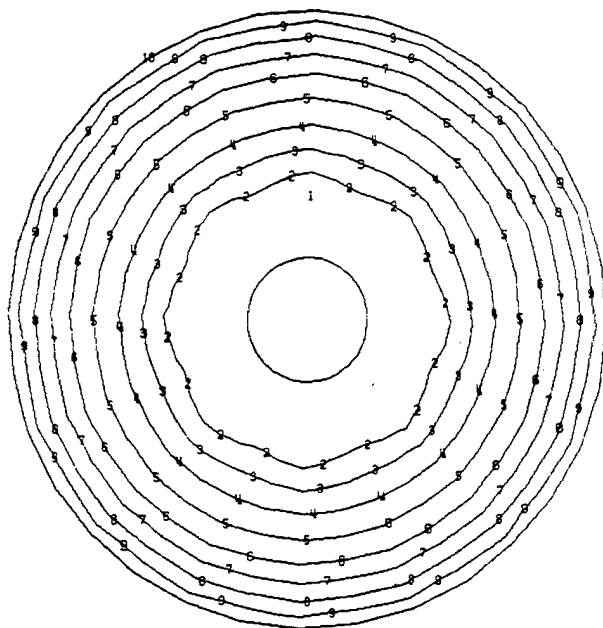


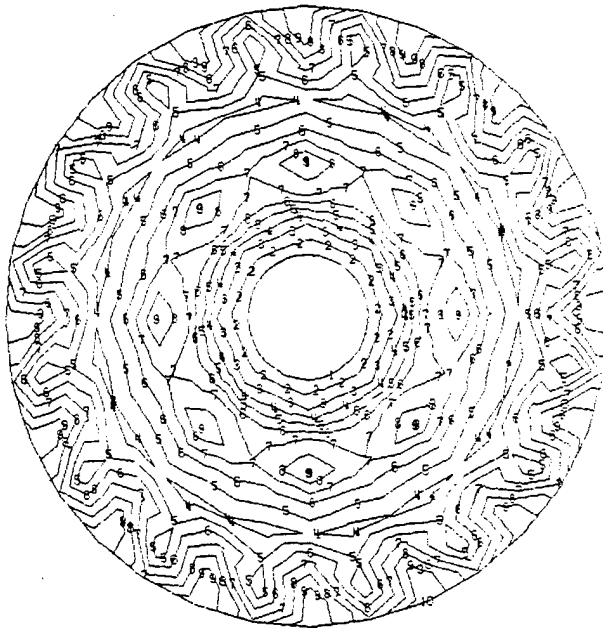
Fig. 5.28. System Model with Solid Mirror and Small Reference Plate, Axial Thermal Gradient of 1°C .

Max-Def = 9.67×10^{-6}
 Min-Def = -3.83×10^{-5}



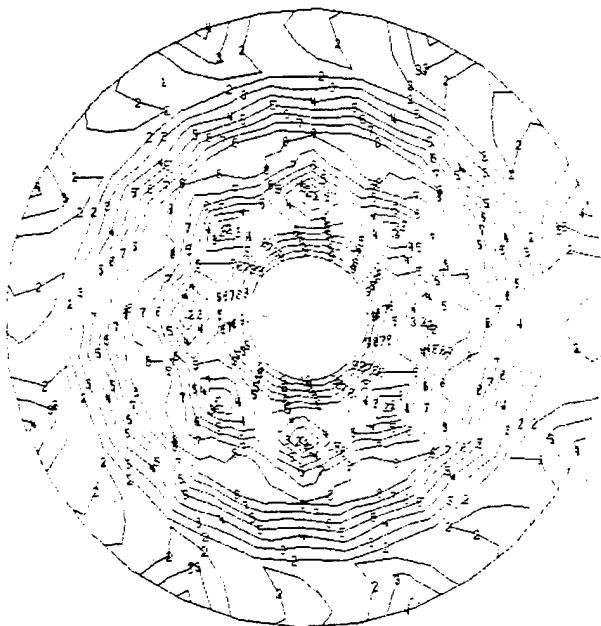
(a) No Actuator Control

Max-Def = 9.24×10^{-7}
 Min-Def = -2.14×10^{-6}



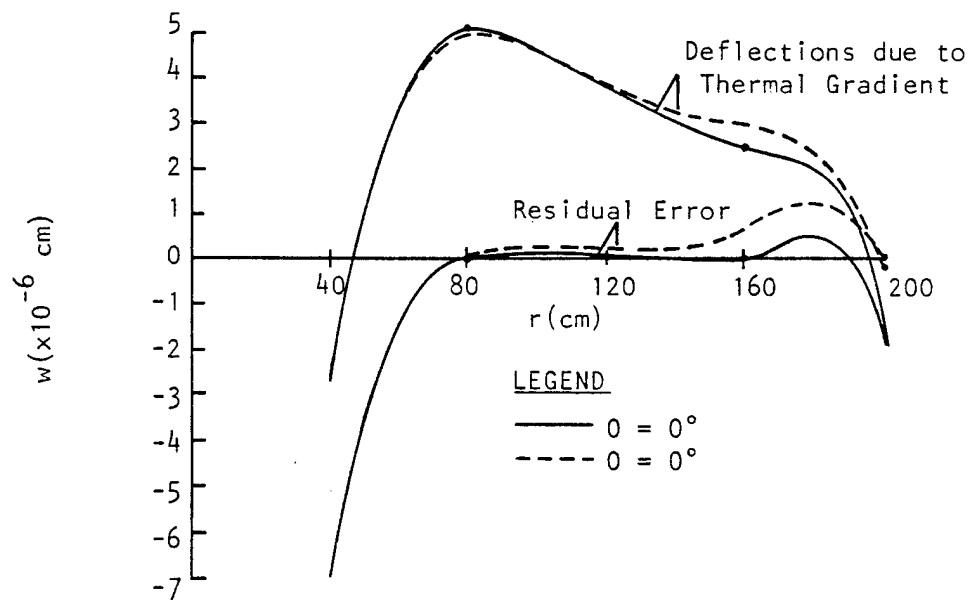
(b) Normal Position Control

Max-Def = 1.73×10^{-7}
 Min-Def = -1.10×10^{-8}

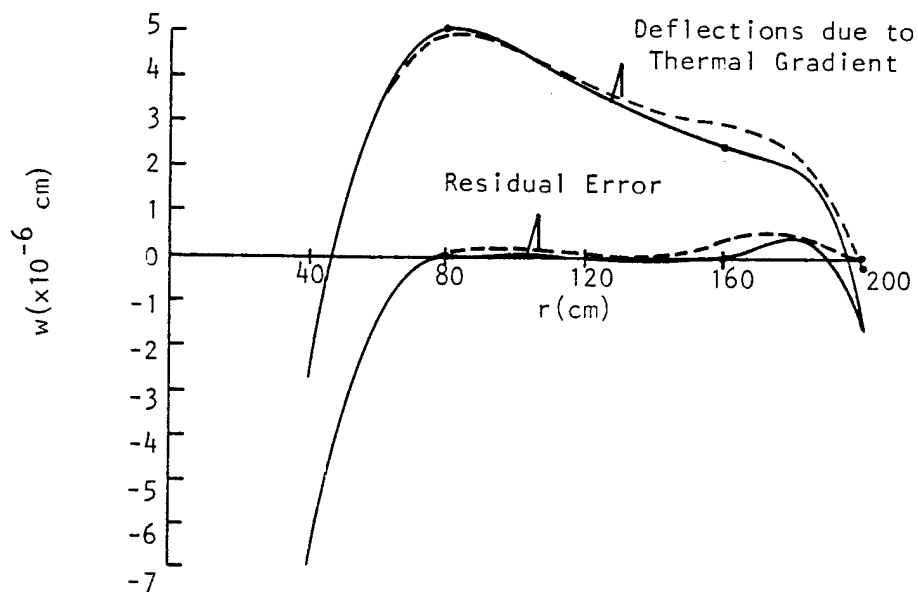


(c) Normal Position and Slope Controls

Fig. 5.29. System Model with Solid Mirror and Small Reference Plate, Uniform Thermal Soak of 1°C .

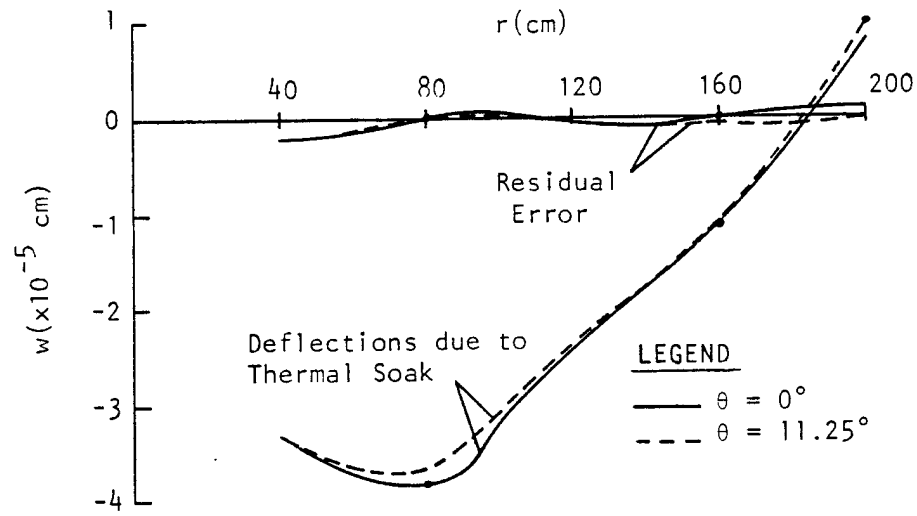


(a) Normal Position Control

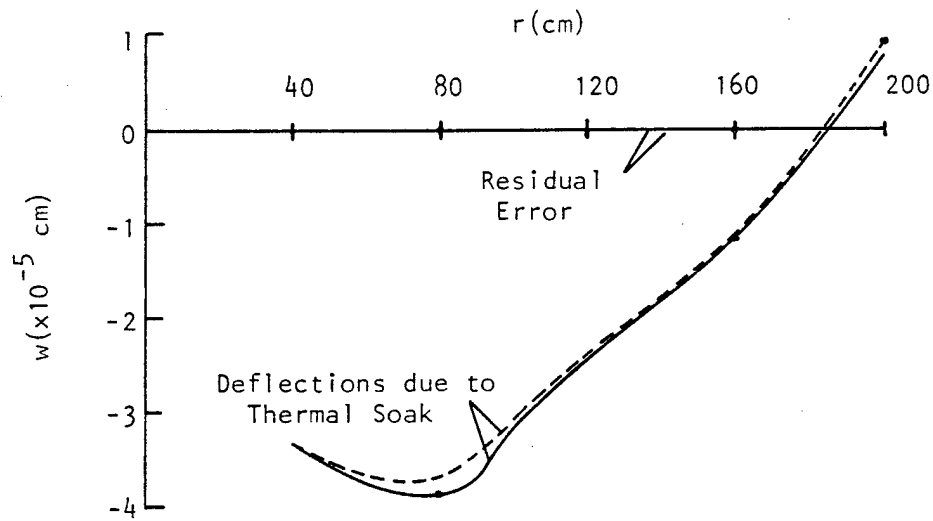


(b) Normal Position and Slope Controls

Fig. 5.30. System Model with Solid Mirror and Small Reference Plate, Cross Sections for Thermal Gradient.



(a) Normal Position Control



(b) Normal Position and Slope Controls

Fig. 5.31. System Model with Solid Mirror and Small Reference Plate, Cross Sections for Thermal Soak.

FRINGE results are in Table 5.3.

The figures for the thermal gradient loading show that, due to the greater thermal expansion of the top face of the mirror as compared to the bottom face, both the inner and outer edges of the mirror curl toward the rear. Actuators along the outer edge of the mirror reduce the curling, but between actuators scalloping takes place. The combination of slope and position controls does not combat scalloping significantly better than position control alone. In fact the rms values of the residual wavefront are equal for the two cases. Since there are no actuators along the inner edge of the mirror, inner edge warp could not be restrained. It will probably be necessary to add actuators along the inner edge, but even then some of the scalloping will exist between these new actuators, just as it does between actuators on the outer edge. Alternatively, masking around the inner edge reduces rms values by factors of 3 and 4 for the two types of controls. Controls have so little effect, that the rms of the residual of the masked, uncontrolled mirror is about one-third of the rms of the unmasked, controlled mirror. This load demonstrates that drawing conclusions based upon contour plot shapes is unreliable. Even though the plots are cleared up when controls are made, rms values are reduced only 15%.

For uniform thermal soak performance is again difficult to gauge from contour plots. The plots get much more involved as actuators make their corrections, but magnitudes are markedly reduced. The shape of the uncorrected mirror is analogous to a defocus. For the case of normal position and slope controls, corrections are so precise that not enough decimal places were printed to determine the rms value and

error ratio, and the curve for the radial cross-section is indistinguishable from the abscissa. Masking is ineffective.

Loads discussed had a magnitude of 1°C . Table 5.5 summarizes maximum allowable temperatures for a residual wavefront variation of $.1\lambda$ rms. Without masking of the uncorrected system, an axial thermal gradient of 5°C produces $.1\lambda$. The gradient due to sunlight was shown in the heat transfer analysis of the solid mirror in Chapter 4 to be only $.76^{\circ}\text{C}$. Therefore a heat load 6.6 times as intense as sunlight can be applied. By using actuators which lock in position when turned off, the active figure control system may not have to be turned on when the mirror is exposed to sunlight. This would greatly simplify the role of the active control system, by relying on the "passive" inherent stiffness of the structure of the integrated active mirror. For uniform thermal soak results are equally as impressive. It is amazing that a thermal soak of over 200°C can be withstood by using position and slope controls!

Contour plots for the same solid mirror but with a flexural mount and with a nominal reference plate are in Fig. 5.32 for the case of no actuator control. FRINGE results for the flexured system are in Table 5.4. The rms values are about one-half of those discussed previously for the kinematic mount with the small reference plate. Surely the corrected rms values would be less than before.

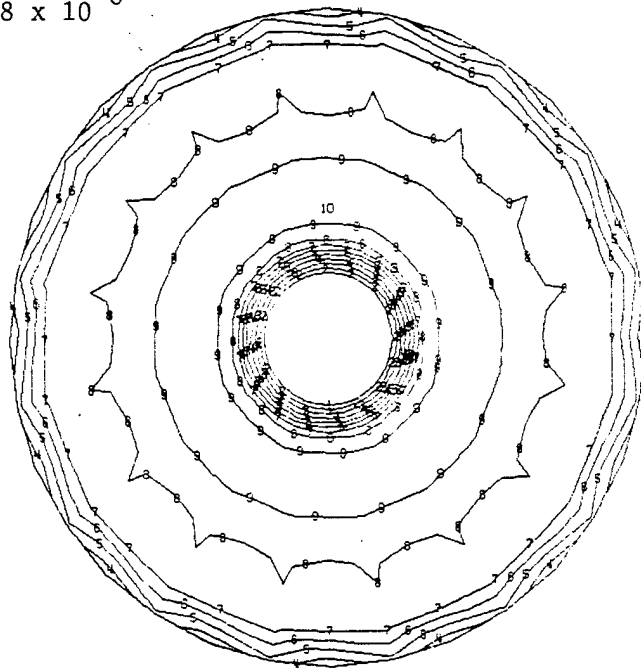
An estimate of the mirror deflection from an axial thermal gradient applied to a system with a lightweight mirror is derived from deflections for the system with a solid mirror. An assumption is made that the deflections are entirely due to the thermally induced bending moments in

Table 5.5. Thermal Loads in °C Producing Residual Wavefront Variation of .1λ rms for System Model with Solid Mirror and Small Reference Plate.

Load	No Correction	Normal Correction	Normal & Slope Correction
Axial thermal gradient	5.0 17.	5.9 20.0	5.9 25.0
Uniform thermal soak	4.8 7.1	14.0 13.0	>200.0 100.0

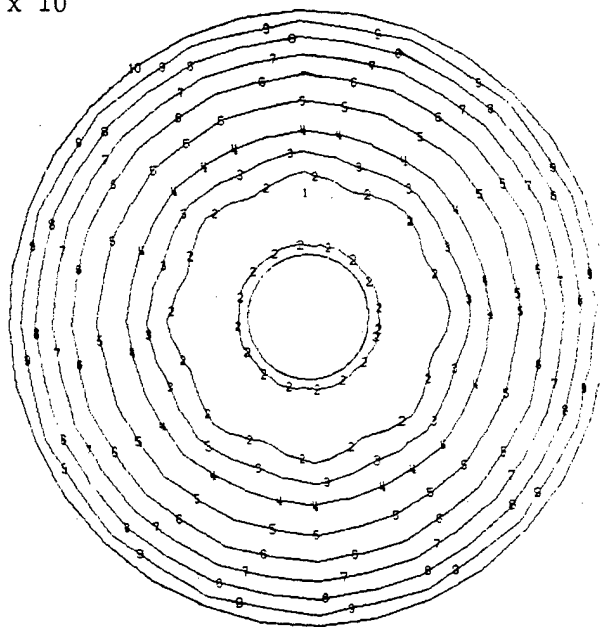
Note: Upper numbers use wavefront from entire mirror and lower numbers use wavefront from masking section of mirror within inner ring of actuators.

Max-Def = 4.24×10^{-6}
 Min-Def = -3.58×10^{-6}



(a) Axial Thermal Gradient of 1° C

Max-Def = 2.49×10^{-5}
 Min-Def = -1.76×10^{-5}



(b) Uniform Thermal Soak of 1° C

Fig. 5.32. System Model with Solid Mirror, Nominal Reference Plate, and Flexure Mount. Thermal Loads.

the mirror, and not to the membrane forces. For a solid mirror:

$$D = \frac{Eh^3}{12(1-\nu^2)}$$

$$M = \frac{q}{12kA_s} h^3 \propto E$$

$$\delta_S \propto \frac{M}{D} = \frac{(1-\nu^2)q\alpha}{kA_s}$$

δ = mirror displacement

M = bending moment per unit width from an axial temperature gradient through the mirror

D = flexural rigidity

The displacement is independent of the modulus of elasticity (E) and the thickness (h). For a lightweight mirror:

$$D = \frac{Ef(\Delta x + f)^2}{2(1-\nu^2)}$$

$$M = \frac{q}{2kA_c} \Delta x(\Delta x + f) f \alpha E$$

$$\delta_L \propto \frac{M}{D} \approx \frac{(1-\nu^2)q\alpha}{kA_c} \quad \text{for } \frac{\Delta x}{(\Delta x + f)} \approx 1$$

This time displacement is independent of E , the faceplate thickness (f), and the core thickness (Δx), so that both the thick and thin lightweight mirrors would perform equally when exposed to sunlight. Comparing results for the solid and lightweight mirrors:

$$\frac{\delta_L}{\delta_S} = \frac{A_S}{A_C}$$

For a 10% dense core the plan area of the solid mirror (A_S), is 10 times the plan area of the core of a lightweight mirror (A_C) so that

$$\frac{\delta_L}{\delta_S} = 10 .$$

Applying this factor of 10 to the deflection of the solid mirror exposed to sunlight, $.0152\lambda$ rms, yields an approximate deflection of $.152\lambda$ rms for a lightweight mirror. In a previous study (Shannon, Richard, and Hansen, 1980, p. 57) the value for a system with the thin lightweight mirror and a reference plate with stiffness equivalent to the nominal size gave a deflection of $.231\lambda$ rms, so the method of estimation is quite accurate.

Conclusions can be formulated based on the thermal analyses. In a well designed thermal environment the passive aspects of the 40-actuator system are all that is needed to keep a solid mirror's figure below $\lambda/10$, if the most intense lighting is sunlight. Bending loads, e.g. the axial thermal gradient, cause deformations more difficult to correct than deformations from membrane loads, e.g. uniform thermal soak. This also explains why gravitational deformations are so difficult to handle.

Miscellaneous Output

Stresses, actuator strength and stroke, and actuation sensitivities are provided for gravity and thermal loads.

Stress

Maximum stresses in each main type of structural member in the 40-actuator system are given in Table 5.6. For all structural members except the mirror, stresses given are the maximum or minimum extensional (axial plus bending) stresses at the ends of the beam. For gravity loads, where stresses are highest, the largest stress occurs in the truss diagonal, and its axial stress is greater than 7 times its bending stress, so it is not worthwhile to find the maximum stress throughout the length of the beam. For the mirror plate elements stresses presented may occur at either the top or bottom surface.

The first three loads are applied to a system with the solid mirror and a small reference plate and under normal position control. Thermal stresses are negligible as compared to gravitational stresses. The maximum stress from the 1g load is 1,250 psi in a truss diagonal. The maximum shear stress in the mirror is 30 psi.

The fourth load case is a 10g launch load applied to the solid mirror with the nominal reference plate and with no actuator control. Launch loads for an orbital telescope include both a steady state acceleration and the static equivalent of dynamic acceleration. The maximum equivalent static launch load is taken to be 10g (ITEK, 1970, p. 5-16). The maximum stress again occurs in a truss diagonal and is 9,600 psi. The maximum shear stress in the mirror is 420 psi. Using the ultimate stresses in Fig. 5.2, the margins of safety of 5.4 and 17 are sufficient to prevent rupture even without an auxiliary support during launch.

The mirror's dimensional stability under the 10g load is also a consideration. Nonrecoverable deformation of the mirror is estimated by scaling the rms figure error so that it equals the allowable error of $\lambda/20$. Maximum shear strain in the mirror scales to 8.46×10^{-9} . From ULE data presented by Woods (1970), an applied shear stress of 2,400 psi would create such a nonrecoverable shear strain. Since the maximum shear stress in the mirror for the 10g load is 420 psi, upon release of the 10g load the nonrecoverable figure error is admissible even before controls are administered.

Table 5.6. Stresses in System Model in Dyne/cm²

Load	Reference Plate	Actuator Posts	Sliders	Truss Members	Mirror (Max. Shear Stress)	Mirror (Max. Principal Stress)
lg z gravity with normal position control	5.4×10^7	5.6×10^6	-8.0×10^6	8.6×10^7	2.1×10^6	-3.0×10^6
Axial thermal gradient of 1°C with normal position control	-3.8×10^3	2.1×10^4	-6.4×10^3	1.4×10^4	6.1×10^3	1.6×10^4
Uniform thermal soak of 1°C with normal position control	-3.1×10^4	9.0×10^4	8.3×10^3	-5.7×10^4	2.2×10^3	-5.3×10^3
10g z gravity with no actuator control	-2.5×10^8	-1.2×10^8	-6.5×10^7	-6.6×10^8	2.9×10^7	3.2×10^7
Euler buckling stress	-1.9×10^{10} (Pinned-Pinned)	-2.9×10^9 (Pinned-Pinned)	-1.3×10^9 (Clamped-Free)	-7.7×10^9 (Clamped-Clamped)		

For all beam elements the stress required for Euler buckling is more than 10 times the maximum stress under the 10g load.

The blade flexure in the actuator post was checked for rupture and buckling under the 10g gravity load. Since the flexure is a pin joint in the model, its stresses were computed indirectly. Assuming the axial stress in the flexure to be the same as in the lower actuator post, the maximum axial stress is 1,600 psi. The angle of rotation of the lower post was also computed indirectly (Schaefer, 1979, p. 182) and was used to find the stress due to pure bending of 360 psi. Shear stress is smaller than the pure bending stress. Since the flexure would be made of high strength steel with ultimate stress over 100,000 psi, flexure stresses are negligible. The stress for Euler buckling of the flexure is very high--990,000 psi.

Actuator Strength and Stroke

Maximum actuator forces and actuator deflections (not mirror deflections) for various loads help to determine the strength and stroke required of the servomotor. A 40-actuator system with the solid mirror and the small reference plate was subjected to gravity and thermal loads. Maximum forces and deflections required for actuators for all three types of controls are in Table 5.7. The maximum force, 45 lb, and deflection, .0060 in., both occur for the 1g gravity load normal to the mirror. Actuator forces for normal, in-plane slope, and out-of-plane slope controls are, respectively, the axial forces in the slider, in the reference plate bars (the difference of the axial forces in bars on each side of an actuator post), and in the dummy rod. Actuator deflections are from the thermal strains applied to each of these members.

Table 5.7. Maximum Actuator Forces and Deflections in System Model with Solid Mirror and Small Reference Plate.

Load	Normal Actuator Force (Dyne)	In-Plane Slope Actuator Force (Dyne)	Out-of-Plane Slope Actuator Force (Dyne)	Normal Actuator Deflection (cm)	In-Plane Slope Actuator Deflection (cm)	Out-of-Plane Slope Actuator Deflection (cm)
x gravity of lg with normal position control	1.4×10^7			4.3×10^{-3}		
x gravity of lg with normal position and slope controls	1.3×10^7	2.8×10^6	6.0×10^5	4.5×10^{-3}	3.9×10^{-3}	3.8×10^{-3}
z gravity of lg with normal position control	2.0×10^7			1.5×10^{-2}		
z gravity of lg with normal position and slope controls	1.9×10^7	2.5×10^6	1.2×10^6	1.5×10^{-2}	4.8×10^{-3}	3.6×10^{-3}
Axial thermal gradient of 1°C with normal position control	1.6×10^4			5.6×10^{-6}		
Axial thermal gradient of 1°C with normal position and slope controls	9.0×10^3	1.6×10^3	1.1×10^4	5.4×10^{-6}	2.9×10^{-6}	1.5×10^{-5}
Uniform thermal soak of 1°C with normal position control	2.1×10^4			5.1×10^{-5}		
Uniform thermal soak of 1°C with normal position and slope controls	4.1×10^3	3.5×10^3	8.9×10^3	5.1×10^{-5}	3.3×10^{-5}	3.1×10^{-5}

Actuation Sensitivity

Sensitivities of mirror motion to actuation force aid in designing the servomotors. Sensitivities in Table 5.8 are from both system and mirror models. The reasonable correlation in these values insinuates that the mirror model is adequate to estimate sensitivities of other systems. In-plane slope control sensitivity is greater than out-of-plane slope control sensitivity due to the introduction of the blade flexure in the actuator post. Loads in actuated members were inadvertently not printed in the system model analysis, so they were calculated from the strain and the initial stress in the actuated members using $\sigma = E\epsilon + \sigma_0$.

Table 5.8. Sensitivities of 80-cm Actuators

Model	Normal Position Control	In-plane Slope Control	Out-of-plane Slope Control
System model with solid mirror and small reference plate	1.4 λ /lb	7.2×10^{-6} rad/lb	4.8×10^{-6} rad/lb
Solid mirror model	.571	9.4×10^{-6}	9.0×10^{-6}

CHAPTER 6

ADDITIONAL WORK

This section describes additional work beyond the scope of this study to refine the integrated active optics system design incorporating a 4 m primary. Additional work is intended to either improve system performance by design modification, better characterize system performance or refine the accuracy of the analyses. Topics are listed in an estimated order of priority in Table 6.1. Without knowing the results of the work it is impossible to establish an exact priority.

Table 6.1. Additional Work to be Completed

Slope Control. To localize deformations for both in-plane and out-of-plane slope controls, the method of slope control should be changed to that of Case 11 in Fig. 3.6 in which a pair of offset forces are applied to an actuator post. The forces would be applied in the model by thermal loading. The blade flexures in the middle of the actuator posts would be changed to thin rod flexures.

Additional Actuators at Inner Edge. A ring of eight actuators with tangential trusses at the inner edge of the annular mirror would reduce scallop and edge wrap.

Beam Actuator. A beam actuator consists of a flexible beam and a force actuator. The beam is attached to the back of a mirror by blade flexures at its ends, so that thermal expansion of the mirror is not restricted by the beam. Located at the middle of the beam, the actuator applies equal but opposite forces to the mirror and the beam. A single beam actuator would span the mirror section between two actuator attachment points of the 40-actuator system. This type of actuator, but without flexures, was proposed by Berggren and Lenertz (1975). It would effectively reduce displacements from defocus, gravity loads and an axial thermal gradient.

Moment Actuator. A moment actuator applies equal but opposite moments to two points on a mirror without reacting against a backup structure (Scott, 1975). A moment actuator constructed of a force actuator reacting at points offset from the center of the mirror would introduce membrane forces as well as moments. Scalloping exhibited during defocus could be relieved by radially aligned moment actuators, creating a radial membrane stress in addition to bending stresses. Moment actuators would also be effective for correcting deflections due to gravity loads and due to an axial thermal gradient through the mirror.

Elastic Variable Optimization. The cross-sectional properties of the reference plate and the other structural members should be varied and analyses repeated. Optimization curves for the 3-dimensional model would be similar to the curves presented in Fig. 3.5 for the 2-dimensional model. The structure is then optimized at the elastic variable level of solution hierarchy. This does not guarantee optimization at the topology level, the highest level of hierarchy, or the geometry level, the intermediate level. The topology level is characterized by basic connectedness, by numbers of actuators and by numbers, types and shapes of structural members. The geometry level is concerned with lengths and locations (Soosaar, 1971).

Table 6.1.--(continued) Additional Work to be Completed

Inhomogeneity of Thermal Expansion Coefficient. For a ULE mirror there is a radial variation in α attributed to oven temperature gradients (Friedman and Gasser, 1972). Analyses (Soosaar, Grin, Furey and Hamilton, 1975) of a design for a lightweight ULE primary mirror with 3.05 m aperture and for the NASA Large Space Telescope accounted for the inhomogeneity of α . One analysis used a nominal expansion coefficient ($\alpha = .03 \times 10^{-6}/^{\circ}\text{C}$) while another used a radial variation of α in the top and bottom faces. The rms deviations from the best fit sphere due to a 1°F thermal soak and a 1°F axial thermal gradient are 2.7 and 4.2 times greater for the variable α than for the nominal α . Corresponding factors for the 40-actuator system are of interest.

Interactuator Mirror Surface Ripple. Ripple and servo-channel cross coupling both depend on the shape of the individual actuator influence functions, which are the normalized mirror surface deflections. Mechanical mirror actuator coupling is the influence function amplitude at the center of the adjacent actuator. As mechanical coupling is increased, rippling decreases and servo coupling increases. For a hexagonal array of high frequency actuators, Pearson and Hansen (1977) state that a nearly Gaussian influence function with a mechanical coupling coefficient between 5% and 12% yields acceptably small values of both ripple and servo coupling. A detailed mirror model (see "Discretization Error of Mirror Model") should be used to study ripple of the 40-actuator system, since at least three elements are needed between actuators to distinguish a full sine wave of ripple. Two methods of generating ripple are to drive a group of actuators with equal amplitude and to induce a linear tilt across a section of the mirror surface.

Localized Temperature Gradients. Robertson (1972) experimentally applied a localized temperature gradient to a 30-in diameter thin, deformable mirror. Electric heater pads on the back surface of the mirror created local temperature fields that dropped to one-half of the maximum within a region with diameter one-eighth of the mirror diameter. Deflections were not nearly as localized, and this time one-half the maximum was within a region 2.7 times larger than for the temperature field. This broad deflection is relatively easy to correct. Since Robertson's active optics system had low spring rate force actuators, restraints to the mirror were negligible. For the 40-actuator integrated active optics system, restraints to the mirror are not as flexible. A hot spot should be tested with the integrated system to determine if it results in a broad, easily connectable deformation.

Table 6.1.--(continued) Additional Work to be Completed.

Motion of Support Points. Enforce displacements to simulate the deformation of the telescope tube. Theoretically, the kinematic mount would introduce no load, however friction would cause a small, finite displacement.

Optimal Control Law. In the reported analyses the influence matrix relating mirror deflections at the actuator attachment points was used to compute actuator forces to null actuator displacements from mechanical loads. Then a best fit sphere and associated rms deviation were determined. The optimal control law selects actuator forces to minimize the least-squares fit of errors to a best fit sphere. The influence matrix for optimal control involves mirror deflections at actuator attachment points and at other points on the mirror's surface where deflections are measured. Hill and Youngblood (March 1974) discuss the optimal control law as applied to an active primary mirror.

Discretization Error of Mirror Model. Make a detailed mirror model by subdividing existing quadrilaterals into four smaller quadrilaterals. Execute individual normal position and slope controls and compare plots of the detailed versus the coarse (current) model. Use these two approximate solutions to extrapolate a more exact solution (Zienkiewicz, 1977, pp. 34-35).

Design of Lightweight Mirror. For a lightweight mirror the following parameters can be varied to arrive at an optimal design : material, cell type, cell spacing, cell dimensions, faceplate thicknesses and total thickness. Design curves by Barnes (1969) consider both bending and shear deformation. They establish a proper tradeoff between weight and stiffness during initial design phases of a symmetrical sandwich mirror. If the faceplates have different thicknesses, Barnes' technique will not apply.

Fracture of a Lightweight Mirror. The polished, lightweight mirror will contain debonded regions between the ULE faceplates and the core. A sufficiently large shear stress at the interface between a faceplate and the core will propagate the debonded regions and destroy the mirror. Fracture mechanics predicts the critical shear stress as a function of initial crack length (Soosaar, Grin, Furey and Hamilton, 1975, pp. 5-2 - 5-6). The shear stress is not output directly from NASTRAN. By calling upon the MSC/NASTRAN Alter Library, the program will compute strains and curvatures for two-dimensional plate elements. An auxiliary program to compute shear stress between the facesheets and the core is based on the theory presented by Jones (1975).

Table 6.1.--(continued) Additional Work to be Completed.

3-Dimensional Model of Lightweight Mirror. This model would include membrane elements for the upper and lower faces and cell walls and would model the local core stiffening at the actuators. It would predict local dimpling at the actuator attachment points due both to the individual normal position and slope controls and to thermal loading. It would be sufficient to model a partial section of the mirror. The entire mirror could be modeled effectively with cyclic symmetry (Joseph, 1979, sec. 2.2).

Heat Transfer. With NASTRAN's heat transfer capability a 3-dimensional model of a lightweight mirror and the system model could be analyzed to determine temperatures to apply in structural analyses.

Optical Aberrations. Introduce fourth order coma and spherical aberration in the same manner used for defocus and astigmatism.

Flat Plate Fictitious Rotational Stiffness. Since the curvature of the mirror is so slight, normal vectors to adjacent quadrilaterals in the mirror model are nearly parallel. The angle between them is always less than 1° . When representing a shell as an assembly of flat plate elements, the rotational degree of freedom normal to each flat plate element has zero stiffness. Zienkiewicz (1977, p. 336) presents a method of introducing this rotational stiffness that is equivalent to interconnecting nodes within each individual flat plate with torsional springs. This technique eliminates a minor problem from analysis of the mirror model.

Microyield Strength. The microyield strength (MYS) of a material is the stress producing a permanent strain of 1 micro in/in. The MYS of ULE is 8,000 psi for material under ideal conditions. For pieces of ULE the size of the 40-actuator mirror the MYS is conservatively reduced to 500 psi. To minimize creep and stress relaxation, stresses in the mirror should be no greater than half the MYS (ITEK, 1970, p. D-10). Under the 10 g launch load the maximum principal stress in the mirror is 460 psi and exceeds this guideline. There would only be a problem if the mirror distortion were in a shape uncorrectable by the control system.

CHAPTER 7

CONCLUSIONS

An integrated active mirror system is an efficient structure, because the mirror is integrated with the support structure of the actuator system and because loads are carried in tensile-membrane action. By constructing the mirror and support structure out of dissimilar materials, the mirror, requiring a low thermal expansion coefficient, is made of ULE, and the support structure's high stiffness requirements are met by ultra high modulus graphite epoxy. Correspondence of the expansion coefficient of the two materials is not imperative.

The 40-actuator system with a 2 cm thick, solid mirror and a small reference plate is a diffraction limited primary for a spaceborne telescope subjected to heating from the sun. For ground testing the mirror can be actively corrected to the diffraction limited specification if the reference plate is flexure mounted to the telescope tube with the mirror oriented in a vertical plane. The structure is so proficient that if a 1λ rms error could be tolerated on the ground, and if the ambient telescope temperature was well controlled, the actuator control system would not have to exist. Passive aspects of the structure alone would keep the mirror's figure within tolerance. The solid mirror's mass of 534 kg is far greater than the 310 kg mass of the remainder of the system (support structure and servomechanisms). The reference plate can be lightened, since the greatest mechanical

coupling for actuator normal position control is 4.5%, and it can be increased to 12% (Pearson and Hansen, 1977). The solid mirror was chosen over a lightweight mirror, since the lightweight mirror deforms significantly more and is not quite correctable to diffraction limited performance in a 40-actuator system when exposed to sunlight. Economy and ease of manufacture were also considerations. Ionizing radiation, which changes mechanical and thermal material properties, alters the coefficients of the control matrix of an active mirror. This would have a detrimental effect upon an active primary mirror with high mechanical coupling produced by flexible, force actuators (Robertson, 1970), but it would not seriously degrade an integrated active mirror.

For the 40-actuator system deformations from bending loads (gravity normal to the mirror and an axial thermal gradient from sunlight) and deformations into the shape of a nondevelopable surface (defocus) are difficult to control even with combined normal position and slope controls. Deformations from membrane loads (uniform thermal soak) and deformations into the shape of a developable surface (astigmatism) are easy to control, especially with inclusion of slope controls. In fact, for the solid mirror the error ratios are less than 2.4% for thermal soak and .13% for astigmatism, and both cases experience an improvement more than a factor of 10 by adding slope controls to normal position control. Masking of the unsupported mirror surface within the inner ring of actuators was effective in reducing wavefront variation for the thermal gradient and for defocus but was ineffective with the gravity load. Instead of masking, adding a ring

of eight actuators to the inner edge of the mirror would reduce variations for all three troublesome cases by a greater amount. This treatment would be similar to the treatment of the outer mirror edge for which additional actuators reduced scalloping caused by defocus. To further improve treatment of the gravity load and the thermal gradient, beam actuators or moment actuators (see Chapter 6) could be added between existing actuators. Then the system would have diffraction limited performance for a ground-based telescope and in the presence of thermal loads more intense than sunlight.

Another improvement would be to change slope controls so that couples deflect the actuator posts with no reaction at the reference plate. Consequential reduction in mechanical coupling would bring coupling for slope control close to parity with coupling for normal position control.

Experimental results from a 24 in diameter physical model of a 41-actuator system verify the concept of an integrated active mirror system and more specifically the design of the 40-actuator system. Resemblance between interferograms and computer model contour plots is prominent. Differences are accounted for by play in the connections in the physical model, which has led to extensive use of interconnecting flexures in the 4 m system.

Proper connections and actuator load introduction, allowing for significant weight reduction, were determined from analysis of a 2-dimensional system model. For the 2-dimensional model a 65% reduction in reference plate weight resulted in an increase of worst case mechanical coupling of normal position control of from 4.0% to 4.6%, and for the

3-dimensional model a conservative reference plate weight reduction of only 50% boosted the mechanical coupling from 3.1% to 4.5%. The 2-dimensional model should be used to test model alterations prior to implementation into the 3-dimensional model.

Another invaluable design tool was the mirror model. Mirror deflections from individual controls for the system model were evaluated based upon the same controls applied to the mirror model. Close correlation between the two sets of deflections substantiated the effectiveness of the integrated mirror system. Introduction of optical aberrations from the system model compared so well with results of the mirror model that the mirror model can be used with confidence to study aberrations for other mirrors.

The suggested additional work should proceed a detailed design of an integrated active mirror system.

REFERENCES

- Armstrong, H. H. and Ellison, A. M., "Satellite Applications of Metal Matrix Composites," AFML-TR-79-4007, May 1979.
- Barnes, W. P., Jr., "Optimal Design of Cored Mirror Structures," Appl. Opt. 8(6):1191-1196, June 1969.
- Bathe, K. J., Wilson, E. L. and Peterson, F. E., "A Structural Analysis Program for Static and Dynamic Response of Linear Systems," EERC-75-11, College of Engineering, Berkeley, California, 1973.
- Berggren, R. R. and Lenertz, G. E., "Feasibility of 30-m Space Based Laser Transmitter," NASA-CR-134903, October 1975.
- Cook, Robert D., Concepts and Applications of Finite Element Analysis, John Wiley and Sons, Inc., 1974.
- Friedman, G. and Gasser, G. "Test Results on Homogeneity of Expansion for a 1.8 m ULE Lightweight Mirror," Appl. Opt. 2(12):2768-2777, December 1972.
- Hill and Youngblood, "Active Control of Primary Mirror of an Orbiting Telescope with Thermal Excitation," NASA-CR-120214, March 1974.
- Holmes, R. D. and Haskins, J., "Advanced Composites Design Data for Spacecraft Structural Applications," CASD-AFS-78-006, January 1979.
- International Mathematical and Statistical Library, Inc., "IMSL Library Reference Manual," Houston, Texas, 1979.
- ITEK Corporation, "Technology Study for a Large Orbiting Telescope," ITEK 70-9443-1, May 15, 1970.
- Jones, Robert M., Mechanics of Composite Materials, Scripta Book Co., Washington, 1975.
- Joseph, Jerrard A., "MSC/NASTRAN Application Manual," CDC Version, The MacNeal-Schwendler Corporation, Los Angeles, California, January 1979.
- Kamel, H. A., McCabe, M. W. and Hunten, K. A., "Graphics-Oriented Interactive Finite Element Time-Sharing System (GIFTS) Version, 5.0 User's Manual," College of Engineering, University of Arizona, May 1979.
- Koterwas, D. J., "A Pre-Tensioned Truss System for Active Control of Mirrors," MS Thesis, University of Arizona, 1974.
- Leissa, A. W. and Nietenfuhr, E. W., "Uniformly Loaded Plates of Regular Polygonal Shape," AIAA Journal 3(3):566-567, March 1965.

- Loomis, J. S., "FRINGE User's Manual Version 2," Optical Sciences Center, University of Arizona, November 1976.
- MacNeal, R. H., "A Simple Quadrilateral Shell Element," Computers and Structures, vol. 8, pp. 175-183, 1978.
- Pearson, J. E. and Hansen, S., "Experimental Studies of a Deformable-Mirror Adaptive Optical System," J. Opt. Soc. Am. 67(3):325-333, March 1977.
- Plantema, F. J., Sandwich Construction, Wiley, New York, 1966.
- Radau, R. E. Jr., "Analysis and Design of an Active Thin Shell Mirror," MS Thesis, University of Arizona, 1977.
- Richard, R. M. and Malvick, A. S., "Elastic Deformation of Lightweight Mirrors," Appl. Opt. 12(6):1220-1226, June 1973.
- Robertson, Hugh J., "Development of an Active Optics Concept Using a Thin Deformable Mirror," NASA-CR-1593, August 1970.
- Robertson, Hugh J., "Evaluation of the Thin Deformable Active Optics Mirror Concept," NASA-CR-2073, June 1972.
- Schaeffer, H. G., MSC/NASTRAN Primer-Static and Normal Modes Analysis, Schaeffer Analysis, Inc., Mont Vernon, New Hampshire, 1979.
- Scott, R. M., "New Technique for Controlling Optical Mirror Shapes," Opt. Eng. 14(2):112-115, March 1975.
- Shannon, R. R., Richard, R. M. and Hansen, J. G. R., Final Report on Optimum Optical Structures for Active Control, University of Arizona, 61 pp., January 1980.
- Shannon, R. R. and Smith, W. S., Final Report on Active Mirror Holographic Interferometry, University of Arizona, p. 78, September 1978.
- Soosaar, K., "Design of Optical Mirror Structures," NASA-CR-122397, January 1971.
- Soosaar, K., Grin, R. and Ayer, F., "Analysis and Tradeoff Studies of Large Lightweight Mirror Structures," NASA-CR-143881, April 1975.
- Soosaar, K., Grin, R., Furey, M. and Hamilton, J., "Structural Evaluation of Candidate Designs for the Large Space Telescope Primary Mirror," NASA-CR-143880, April 1975.
- Timoshenko, S., Woinowsky-Krieger, S., Theory of Plates and Shells, McGraw-Hill, Inc., Second Edition, 1959.

Woods, W. N., "Microyield Properties of Telescope Materials," NASA-CR-66886, January 1970.

Zienkiewicz, O. C., The Finite Element Method, McGraw-Hill, Inc. (UK), Third Edition, 1977.